

MODELING AND STOCHASTIC ANALYSIS OF COUPLED OVERLAND AND
VADOSE ZONE FLOW

By

SIQING LIU

A DISSERTATION PRESENTED TO THE GRADUATE SCHOOL
OF THE UNIVERSITY OF FLORIDA IN PARTIAL FULFILLMENT
OF THE REQUIREMENTS FOR THE DEGREE OF
DOCTOR OF PHILOSOPHY

UNIVERSITY OF FLORIDA

2003

This dissertation is respectfully dedicated to my parents for their abundant patience, unselfish love, endless support, and compassionate encouragement

ACKNOWLEDGMENTS

I would like to thank Dr. W. D. Graham, my advisor and mentor, for her tremendous help and time, guidance and encouragement, endless enthusiasm and patience, insight and inspiration, as well as confidence in our work.

I am indebted to Dr. W. D. Graham, Dr. K. L. Campbell and Dr. A. James for their efforts in ensuring financial support throughout my studies in the Department of Agricultural and Biological Engineering of University of Florida.

I would like to express my sincere thanks and appreciation to Dr. W. D. Graham, Dr. K. L. Campbell, Dr. J. D. Jordan, Dr. J. M. Jacobs and Dr. K. Hatfield for providing excellent teaching, for guiding me through this dissertation research, for spending time to serve on my dissertation committee, and for administering my qualifying exam in 2002.

I am grateful to Dr. J. M. Jacobs for supplying me with data for the verification of the numerical model; and for her many insightful suggestions and valuable comments in the writing of my dissertation, especially Chapter 4. I am also thankful to Dr. A. James for his kind help in mathematics; and for his insightful remarks in our regular meetings.

I would like to express my thanks for each family member for their deep love and endless support. Especially I would like to express my deep appreciation to my parents for their raising me and supporting my education. My wife Dong deserves many thanks for everything she has done for me. She sacrificed a lot to provide me a good study environment during this Ph.D. study. I would like to extend my special thanks to my daughter Erica for bringing me endless happiness.

PREFACE

Natural watersheds exhibit spatial heterogeneity in topography, surface roughness, vegetation, and soil infiltration capacity. The variability of these parameters has significant influence on surface runoff, pollutant transport and soil erosion. In most previous work, the spatial analysis of surface runoff was conducted using a one-dimensional kinematic wave model with a simple infiltration model such as the Green-Ampt infiltration equation, Philip infiltration equation or Smith-Parlange equation. Most work analyzed the effects of variability of soil characteristics on the surface runoff peak and volume, but not surface water depth because the influence of water depth on infiltration and subsurface flow was neglected. Thus it is necessary to develop a physically based multidimensional model for the stochastic analysis of coupled surface and subsurface water flow.

In this study, a model is proposed to couple overland flow with flow in the unsaturated and saturated zones. The model includes three components and two linkage utilities, namely, an atmospheric component, an overland flow component and a vadose zone component, a utility to incorporate the atmospheric component into the vadose zone component, and a utility to couple the overland flow component and the vadose zone component.

In the first chapter, a numerical technique based on a finite element method for solving 1-D Richards' equation is introduced. Measures are taken to reduce the oscillatory behavior of the highly non-linear Richards' equation and to improve the mass

balance of solutions. Evaporation and transpiration are modeled as a specified flux boundary and internal sink, respectively, within the vadose zone model. Several examples are presented to demonstrate the accuracy of the vadose zone model.

The second chapter introduces the Penman-Monteith equation for the calculation of potential evapotranspiration. For soils in the presence of plants, potential evapotranspiration is partitioned between evaporation and transpiration according to the plant's leaf area index and its type. The actual evaporation and transpiration are calculated by introducing a soil moisture reduction coefficient, which can be calculated by several methods.

In the third chapter, the 2-D diffusion model of overland flow is derived from the Saint-Venant equations. Again, the finite element method is chosen to solve the diffusion wave problem. The infiltration rate is determined by coupling the overland flow component and vadose zone component. Several examples are presented to demonstrate the accuracy of the overland flow model.

In chapter four, two case studies are presented to verify the coupled model and another two examples are used to study how actual evapotranspiration and water movement in the unsaturated zone are affected when using either average daily or a diurnal cycle of evapotranspiration in the numerical model.

In chapter five, Monte Carlo simulations are conducted using the coupled model to study the effect of uncertain spatial variability in Manning's coefficient, surface elevation and soil saturated hydraulic conductivity on the mean predicted surface water depth, the mean predicted surface runoff, and the prediction uncertainty around these predictions.

In chapter six, an approximate analytical stochastic model, based on stochastic perturbation techniques, is developed to examine the effects of spatial variability of hydraulic conductivity, Manning's coefficient and surface elevation on surface runoff. Expressions are derived for estimating the effective parameter values of hydraulic conductivity, Manning's coefficient and surface elevation as well as the model prediction uncertainty. The analytical model is tested against the Monte Carlo simulations presented in Chapter 5.

Chapter 7 summarizes main findings from the study and gives some recommendations for future research.

TABLE OF CONTENTS

| | <u>page</u> |
|-----------------------------------------------------------------------------------------------|-------------|
| ACKNOWLEDGMENTS | iii |
| PREFACE..... | iv |
| ABSTRACT..... | ix |
| CHAPTER | |
| 1 MODELING WATER FLOW IN THE VADOSE ZONE..... | 1 |
| 1.1 Literature Review..... | 1 |
| 1.2 Development of Governing Equation | 8 |
| 1.3 Initial and Boundary Conditions..... | 14 |
| 1.4 Development of 1-D Vadose Zone Flow Model..... | 15 |
| 1.5 Convergence Criteria and Mass Balance Calculation..... | 23 |
| 1.6 Verification of the Model..... | 25 |
| 1.7 Conclusions and Discussions..... | 34 |
| 2 WATER-PLANT-ATMOSPHERE MODEL..... | 36 |
| 2.1 Introduction..... | 37 |
| 2.2 Potential Evaporation and Transpiration | 41 |
| 2.3 Actual Evaporation and Transpiration | 44 |
| 3 OVERLAND FLOW MODEL..... | 47 |
| 3.1 Introduction..... | 47 |
| 3.2 Governing Equations | 51 |
| 3.3 Numerical Model Development..... | 55 |
| 3.4 Initial and Boundary Conditions..... | 58 |
| 3.5 Verification of the Overland Flow Model | 59 |
| 3.6 Conclusions..... | 64 |
| 4 INTEGRATING ATMOSPHERIC AND OVERLAND FLOW COMPONENT WITH VADOSE ZONE FLOW COMPONENT..... | 65 |
| 4.1 Introduction..... | 65 |
| 4.2 Integrating Model Components | 68 |

| | |
|------------------------------------------------------------------------------------------------------------------------------------------|------------|
| 4.3 Integrated Model Examples | 69 |
| 4.4 Concluding Remarks..... | 86 |
| 5 MONTE CARLO SIMULATION OF COUPLED OVERLAND AND VADOSE ZONE FLOW | 89 |
| 5.1 Introduction..... | 89 |
| 5.2 Statement of the Problem..... | 94 |
| 5.3 Analysis of Results | 96 |
| 5.4 Conclusions..... | 117 |
| 6 APPROXIMATE ANALYTICAL STOCHASTIC ANALYSIS OF COUPLED OVERLAND AND VADOSE ZONE FLOW..... | 121 |
| 6.1 Introduction..... | 121 |
| 6.2 A Stochastic Analytical Model for Predicting Surface Runoff Uncertainty..... | 125 |
| 6.3 Solution of Covariance Equations for the Steady-State 1-D Stationary Case | 132 |
| 6.4 Deriving the Effective Parameters for the Steady State 1-D Stationary case | 138 |
| 6.5 Verification of Analytical Models for Predicting Surface Runoff Uncertainties..... | 143 |
| 6.6 Verification of Analytical Model for Effective Parameter Value for Manning's Coefficient and | 159 |
| 6.7 Conclusions..... | 168 |
| 7 SUMMARIES AND DISCUSSIONS | 171 |
| APPENDIX | |
| A DERIVATION OF MATRICES A, B AND F | 175 |
| A.1 For Moisture-Content Based Governing Equation | 175 |
| A.2 For Pressure Based Governing Equation | 177 |
| B ROOT DENSITY DISTRIBUTION FUNCTIONS AND SOIL MOISTURE RESTRICTION FACTOR | 179 |
| B.1 Root Density Distribution Functions..... | 179 |
| B.2 Soil Moisture Restriction Factor | 180 |
| C CALCULATIONS OF MATRICES FOR GALERKIN FEM APPROACH | 181 |
| D DERIVING THE AUTOCOVARIANCE OF WATER DEPTH AND THE CROSSCOVARIANCE FUNCTION BETWEEN SURFACE SLOPE AND WATER DEPTH | 185 |
| LIST OF REFERENCES..... | 188 |
| BIOGRAPHICAL SKETCH | 203 |

Abstract of Dissertation Presented to the Graduate School
of the University of Florida in Partial Fulfillment of the
Requirements for the Degree of Doctor of Philosophy

MODELING AND STOCHASTIC ANALYSIS OF COUPLED OVERLAND AND
VADOSE ZONE FLOW

By

SIQING LIU

AUGUST 2003

Chair: Dr. Wendy D. Graham

Cochair: Dr. Kenneth L. Campbell

Department: Agricultural and Biological Engineering Department

In this study, a model was developed to couple overland flow with vadose zone flow. The 1-D Richards' equation was used to model unsaturated flow and solved using a finite element method. Evaporation and transpiration were modeled as a specified flux boundary and internal sink respectively within the vadose zone flow model. The Penman-Monteith equation was selected to estimate potential evapotranspiration, which was partitioned between evaporation and transpiration according to the plant's Leaf Area Index (LAI) and its type. The actual evaporation and transpiration were calculated by introducing soil moisture reduction coefficients, which can be obtained by several methods. A diffusion wave model of overland flow was derived from the Saint-Venant equations, and solved using the finite element method. Several examples were presented to verify the overland flow component, the vadose zone flow component, and the coupled numerical model. These examples showed that each component and the coupled model

are reliable and give results similar to analytical solutions, results from other numerical models or experimental data.

Using the coupled model developed in this study, Monte Carlo simulations were conducted to study the effect of uncertain spatial variability in Manning's coefficient, surface elevation and soil saturated hydraulic conductivity on the mean predicted surface water depth, the mean predicted surface runoff, and the prediction uncertainty around these values. The Monte Carlo simulation results showed that the spatial variability of saturated hydraulic conductivity, Manning's coefficient, and microtopography influences the mean surface runoff hydrograph in runoff starting time, ending time, discharge peak and volume. Among the three spatially varied parameters, hydraulic conductivity demonstrates the greatest effect on runoff discharge rate and total volume, while Manning's coefficient has the greatest effect on surface water depth.

A 1-D analytical model, based on stochastic perturbation techniques, was also developed to examine the effects of spatial variability of land surface elevation, surface roughness, and hydraulic conductivity on surface runoff. Expressions were derived for estimating the model prediction uncertainty, and the effective parameter values for hydraulic conductivity, Manning's coefficient, and surface elevation. The analytical model was tested against the Monte Carlo simulations results. The comparison shows that the analytical model agrees reasonably well with the Monte Carlo simulation.

CHAPTER 1 MODELING WATER FLOW IN THE VADOSE ZONE

1.1 Literature Review

1.1.1 Introduction

The vadose zone is the connection between the saturated zone and the surface. Precipitation percolates into the saturated zone through this zone. Evaporation and transpiration draw water from the vadose zone and result in water flowing from the saturated zone into the vadose zone by capillary forces. Movement of water in this zone must be studied to understand the influence of precipitation, evaporation and transpiration on the depth of the ground water table.

Many authors have studied vadose zone flow. The first research on vadose zone flow may be ascribed to Edgar Buckingham (1867-1940). His theoretical and experimental studies on the dynamic movement of soil gases and soil physics (Buckingham, 1907) led to a major contribution to the foundation of soil physics. Based on the works of Fourier and Ohm, Buckingham rigorously defined the concept of capillary potential and proposed that the steady flux of moisture through an unsaturated soil is directly proportional to the gradient of soil-water potential. The mathematical form of this statement was much the same as that of Darcy's Law, except that the parameter of proportionality was recognized by Buckingham to be a function of the degree of soil saturation with which Darcy was concerned half a century earlier. In a word, Buckingham provided a paradigm for soil physics and unified the flow process in the saturated and the unsaturated zone. Thus some soil physicists persuasively argued that we

should use the phrase “Darcy-Buckingham’s Law” instead of Darcy’s Law, especially when applying the law to vadose zone flow modeling.

Green and Ampt (1911), who were aware of the work of Buckingham (1907) and other soil physicists, proposed a simple approximation to quantify the vertical infiltration of water into the unsaturated zone. The Green-Ampt model assumes a steep wetting front of infiltration in an approximate homogeneous system. This infiltration model has been the subject of considerable attention since its publication, mainly because of its simplicity and good approximation of one-dimensional infiltration into a homogeneous coarse-textured soil with a small uniform initial moisture content (Philip, 1969).

Richards (1931) combined capillary potential with gravitational potential and showed that Darcy’s Law, which was originally proposed for saturated porous media, was equally valid in the partially saturated zone. Richards combined the Darcy-Buckingham equation with the mass balance equation to produce an equation describing flow and storage of water in the vadose zone subject to gravitational and capillary forces.

Because of the nonlinearity of Richards’ equation, it was evident that unsaturated hydraulic conductivity could not be acquired from field data unless some simple relationship between hydraulic conductivity and soil water pressure could be assumed on the basis of available data. Gardner (1958) found that over a limited range of soil water pressure, one could reasonably assume an exponential relationship between hydraulic conductivity and soil water pressure head. Gardner further pointed out that an exponential relation helps to obtain a closed-form solution for the one-dimensional problem.

From the beginning of the twentieth century, great efforts were made to find analytical or semi-analytical solutions to Richards’ equation. Phillip (1957, 1969)

published a series of articles on the exact solutions of absorption equations and infiltration equations. His work greatly increased our understanding of absorption and the infiltration processes.

At the same time, research was being carried out to apply the Green-Ampt model to more complicated situations. Van Duin (1955) and Bouwer (1964, 1969) extended the original Green-Ampt model to account for infiltration into layered soils. Childs and Bybordi (1969) did similar work and showed excellent agreement between the model and experimental data. Mein and Larson (1973) modified the Green and Ampt concept to account for infiltration rates that are initially less than soil infiltrability. Their model showed very good agreement with numerical results obtained by solving the Richards' equation for several soil types.

With the development of high performance computers, research was carried out to find numerical solutions to Richards' equation. Owing to the pioneering work in soil physics by Gardner (1958), Brooks and Corey (1964), Haverkamp et al. (1977) and Van Genuchten (1980), it is now easy to select a soil-water relationship and the corresponding parameters required to develop a numerical model of vadose zone flow. At the same time, emphasis has been put on finding high-performance numerical schemes to solve Richards' equation.

1.1.2 Form of Governing Equation

When developing a numerical model of the vadose zone, the first issue is selecting a form of governing equation. Soil-moisture-based algorithms can result in better mass-balance performance compared to traditional pressure-based methods when modeling infiltration into very dry heterogeneous soil. Unfortunately, soil-moisture-based algorithms cannot be used for problems containing saturated regions since the soil-water

diffusivity function goes to infinity for commonly used soil-moisture models (Hills et al., 1989a).

In contrary, pressure-based solutions to Richards' equation can be used for both saturated and unsaturated soils. However, when flux boundary conditions result in steep wetting fronts moving into very dry soil, pressure-based algorithms usually require small time steps in order to maintain stability and minimize truncation errors. Because of the highly nonlinear nature of unsaturated regions bordering those that are fully saturated, and because of the non-mass conserving nature of pressure-based finite-difference and finite element equations, convergence and stability have been continuing problems (Kirkland et al., 1992).

As a compromise, Celia et al. (1990) proposed a modified numerical approach to alleviate the mass balance problem. This approach introduced a mixed-form equation in which the storage term is expressed in moisture content while flux terms are expressed in head potential. A fully implicit time approximation was applied to the mixed-form of the vadose zone flow equation. The finite difference and the finite-element approximation using this mixed-formation are perfectly mass conservative (Celia et al., 1990).

However, like moisture-content-based algorithms, mixed-form algorithms are not applicable to the situation of layered soils, because the moisture content may not be continuous across the interface between two layers of soil. Thus finding algorithms with a good mass balance has been a continuing topic of research. Milly (1985) presented a mass-conserving solution procedure that used a modified definition of the storage capacity term to force global mass balance. Milly also pointed out the importance of mass lumping in finite-element solutions to vadose zone flow. Abriola and Rathfelder (1993)

and Rathfelder and Abriola (1994) discussed several techniques for calculating the storage capacity term for different lumping methods, namely the standard chord slope (scs) and distributed chord slope (dcs) approximation. They concluded that the most effective method in terms of mass conservation and computational efficiency is the nontraditional finite element chord slope formulation (fecs), in which the capacity matrix is lumped using a single trial function, and capacity coefficients are evaluated with the 'scs' approximation.

Kirkland and Hills (1992) proposed two finite-difference schemes ---one based on a transformed Richards' equation and one on a flux-updating scheme. Kirkland and Hills claimed that their schemes retained the advantages of the soil-moisture-based method for fully unsaturated heterogeneous problems while allowing for fully saturated conditions, and that their schemes were much faster than the algorithms based on the mixed-form of Richards' equation using the modified Picard method.

Yeh (1981) solved the velocity discontinuity and mass balance problem resulting from the standard finite element method by solving Darcy's Law for the velocity field at nodal points using the same finite element method used for the pressure field, rather than simply taking the derivatives of the approximate pressure field. He found that this method could greatly decrease the mass balance error. Berg (1999) compared two mass-conserving procedures where the highly non-linear nature of Richards' equation was overcome by substantially different iterative techniques.

1.1.3 Selection of Numerical Method

The second issue when developing a numerical model is determining which numerical method to implement. The most popular numerical methods used in solving the non-linear Richards' equation include finite difference methods (FDM) and finite

element methods (FEM). Finite difference methods are easy to code, but are not efficient for handling complicated boundaries and boundary conditions. Finite element methods, on the other hand, are more flexible in coping with complicated boundaries and also Dirichlet and Neuman boundary conditions. Perhaps the greatest advantage of FEM over FDM is that one can efficiently discretize areas that have large curvature, or localized regions that require detailed study.

Haverkamp (1977) compared six finite-difference schemes. They found that the head-based implicit method got results at least as good as those of two models that used the Kirchhoff integral transformation. Examples of finite difference algorithms that deal with either variably saturated or fully unsaturated conditions were presented by Freeze (1971), Celia et al. (1990), Kirklan et al. (1992), Clement et al. (1994), Romano et al. (1998), Yakirevich et al. (1998), Diersch and Perrochet (1999) and Berg (1999). Similar problems have been examined by Neuman (1973), Cooley (1983), Huyakorn et al. (1984, 1986, 1993), Celia et al. (1990), Allen and Murphy (1986), Cordes and Kinzelbach (1992), Forsyth et al. (1995) and Ju and Kung (1997) using standard finite element methods. Allen and Murphy (1986) used a finite-element collocation method to solve variably saturated flow in two space dimensions. Gottardi and Venutelli (1992) used a moving finite element model to solve one-dimensional infiltration in unsaturated soils.

1.1.4 Numerical Convergence Issues

A third issue that arises when developing a numerical model for vadose zone flow concerns convergence of the numerical scheme. The simplest approach for solving the nonlinear Richards' equation numerically is to use an explicit two-level time discretization. This approach yields a linear system of equations, minimizes storage requirements, and on a per-time-step basis it represents a least-cost option (Paniconi et

al., 1991, 1994). However stability constraints for explicit solutions are very stringent; and the small time step required to maintain a stable solution can render these schemes very costly on a per-simulation basis. The weighted two-level time implicit discretization, on the other hand, results in a nonlinear system of equations, and an iterative approach is adopted to solve this nonlinear system. The most widely used iterative approaches are Newton Raphson and Picard methods, with the Picard method being the more popular of the two. The Picard method was used by Cooley (1983), Hills et al. (1989b), Huyakorn et al. (1983, 1984, 1986), Neuman (1973) and Ross (1990).

Paniconi et al. (1991, 1994) compared different iterative strategies and concluded that the Newton iterative method is quadratically convergent compared to linear convergence for the Picard scheme. However, both iterative Newton and linearized Newton result in nonsymmetrical system matrices, that lead to problems in solving the system of linear equations.

Huyakorn et al. (1984) stated that the use of the chord slope approximation of capacity term can drastically improve convergence of the nonlinear iterations. He also recommended that the Newton iterative method be used in certain situations where the relative permeability and water saturation functions are very highly nonlinear.

Forsyth et al. (1995) introduced a primary variable switching technique for modeling variably saturated flow. Diersch and Perrochet (1999) used this technique in their research and found that the technique represents a fast and robust strategy for the unsaturated problem with dry initial conditions.

Huang et al. (1996) proposed a soil-moisture-based convergence criterion derived using a Taylor-series expansion of the water content. They found that the new nonlinear

convergence criterion was computationally much more efficient and robust than the alternative two criteria. Ju and Kung (1997) discussed the efficiency of mass types, element orders and matrix solution methods for the Richards' equation. They stated that, when using consistent mass or quadratic/cubic elements, one cannot arbitrarily reduce the time step to achieve convergence. They found lumped mass schemes with linear elements produced good results.

1.2 Development of Governing Equation

The equation that describes the movement of water with variable saturation can be derived by combining the equation for conservation of mass for water with auxiliary equations for fluid flux and storage.

1.2.1 Conservation of Mass

The continuity equation (which considers storage, flux, fluid sources and sinks) is used to describe mass conservation. For a unit volume of soil medium, the continuity can be expressed as

$$\frac{\partial}{\partial t}(\rho S_w \phi) = -\frac{\partial}{\partial x_i}(\rho q) + \rho Q \quad (1-1)$$

where ρ is the water density (ML^{-3}); S_w is the water saturation (L^0); ϕ is the porosity (L^0); t is time (T); q is the Darcy velocity or specific flux (LT^{-1}); Q is the volumetric flow rate per unit volume of soil medium representing water source(+) or sink(-) (T^{-1}); and x_i is spatial coordinates ($i=1,2,3$) (L).

The continuity Equation 1-1 states that the rate of change of water mass stored in a unit volume of soil matrix must be balanced by the sum of water flux across the unit volume and of water added by sources or removed at sinks from the unit volume of soil matrix.

1.2.2 Specific Flux

In Equation 1-1, specific flux can be calculated by the Darcy-Buckingham equation. The Darcy-Buckingham equation is considered valid in porous media with the Reynold's Number (Re, which is equal to $U*D/v$, where U is the velocity of the fluid, D is the characteristic length, and v is the kinematic viscosity of the fluid) less than 10.

$$q_i = -\frac{\rho g k_{ij} k_r(h)}{\mu} \frac{\partial H}{\partial x_j} \quad (1-2)$$

where k_{ij} is the intrinsic permeability of the medium (L^2); $k_r(h)$ is the relative hydraulic conductivity as a function of pressure head (L^0); h is the pressure potential (L); g is the gravitational acceleration (LT^{-2}); μ is the dynamic viscosity of the water ($ML^{-1}T^{-1}$); H is the total potential of the water, expressed as the height of a column of the water (L).

Usually, a lumped hydraulic conductivity K_{ij} (LT^{-1}) is used in the Darcy-Buckingham equation.

$$K_{ij}(h) = \frac{\rho g k_{ij} k_r(h)}{\mu} \quad (1-3)$$

Total water potential consists of two parts, pressure potential and gravitational potential resulting from position relative to a selected reference datum. The convention used in this work is that vertical distance z is assumed positive downward with datum at or above the land surface. Below the water table, the pressure potential is proportional to the weight of overlying water and increases with depth. In the unsaturated zone, water is held in the porous media by adsorptive and capillary forces. The pressure potential exists as tension, so it is negative. The equation for total water potential is written as

$$H = h + h_z = \frac{p}{\rho g} - z \quad (1-4)$$

where h_z is the gravitational potential (L); p is the water pressure ($\text{ML}^{-1}\text{T}^{-2}$); and z is the position relative to datum (L);

In soil physics, it is customary to rewrite Equation 1-4 in terms of a suction pressure ψ , defined as

$$\psi = \frac{P - P_a}{\rho g} \quad (1-5)$$

where p_a is the atmospheric pressure. Then, water flux can be expressed as

$$q_i = -K_{ij} k_r(\psi) \left(\frac{\partial \psi}{\partial x_j} - \frac{\partial z}{\partial x_j} \right) \quad (1-6)$$

1.2.3 Storage Term

For transient flow, drainage in water storage must be considered. Water storage is expressed by the first term in Equation 1-1 and can be expanded using the product rule:

$$\frac{\partial(\rho S \phi)}{\partial t} = \rho \phi \left(\frac{\partial S}{\partial t} \right) + \rho S \left(\frac{\partial \phi}{\partial t} \right) + S \phi \left(\frac{\partial \rho}{\partial t} \right) \quad (1-7)$$

The three terms on the right-hand side of Equation 1-7 account for changes in water stored in a unit volume owing to changes in water saturation, compression or expansion of pore space of the porous medium (soil matrix) because of pressure change and compression or expansion of the water.

Using the pressure head ψ as the principal variable, Equation 1-7 can be written in terms of ψ by using the chain rule of calculus to yield

$$\frac{\partial(\rho S \phi)}{\partial t} = \left[\rho \phi \left(\frac{\partial S}{\partial \psi} \right) + \rho S \left(\frac{\partial \phi}{\partial \psi} \right) + S \phi \left(\frac{\partial \rho}{\partial \psi} \right) \right] \frac{\partial \psi}{\partial t} \quad (1-8)$$

The following expressions can be defined:

$$C = \phi \frac{\partial S}{\partial \psi} = \text{specific moisture capacity, L}^{-1}$$

$$\sigma = \frac{\partial \phi}{\partial \psi} = \text{matrix compressibility, } M^{-1}LT^2,$$

$$\beta = \frac{1}{\rho} \frac{\partial \rho}{\partial \psi} = \text{fluid compressibility, } M^{-1}LT^2;$$

$$\text{and } S_s = \rho g(\phi\beta + \sigma) = \text{specific storage, } L^{-1}.$$

So Equation 1-8 can be expressed as

$$\frac{\partial(\rho S\phi)}{\partial t} = [\rho C(\psi) + \rho S S_s] \frac{\partial \psi}{\partial t} \quad (1-9)$$

1.2.4 Soil Moisture Characteristics and Specific Moisture Capacity

For partially saturated media, the pressure potential becomes more negative as the moisture content decreases, and hydraulic conductivity decreases as moisture content decreases. The curve that relates moisture content to soil potential is termed the soil moisture-characteristic curve. This relation, along with several other relations such as k - ψ , ψ - θ , θ - ψ relations, are used in modeling vadose zone flow.

When solving vadose zone flow using either the head-based or mixed-form equation of Richards' equation, specific moisture capacity needs to be handled carefully because of the nonlinear relationship between moisture content and pressure potential. Specific moisture capacity is defined as the slope of the moisture-characteristic curve, which describes the change in saturation with respect to a change in pressure potential under unsaturated conditions.

$$C(\psi) = \frac{\partial \theta}{\partial \psi} \quad (1-10)$$

In the model developed in this study, four types of relationships for the soil moisture function $k=k(\psi)$, and $\theta=\theta(\psi)$ can be used to characterize different types of soil (see Table 1-2). These are two from Gardner (1958), which were used by Haverkamp et

al. (1977), one from van Genuchten (1980), and one from Brooks and Corey (1964). In multi-layer soils, all four equations can be used together.

Table 1-1. Soil moisture characteristic and specific moisture capacity for different models

| | Gardner (1958), | Gardner (1958), | Van Genuchten (1980) | Brooks-Corey (1964) |
|----------------|-----------------------------------------------------------------------------------------------------------------------------------------------------------------------------------------------------|---------------------------------------------------------------------------------------------------------------|-----------------------------------------------------------------------------------------------------------------------|--------------------------------------------------------------------------------------------------------------------|
| $s_e(\psi)$ | $s_e = \frac{\alpha}{\alpha + \psi ^\gamma}$ | $s_e = \frac{\alpha}{\alpha + (\ln \psi)^\gamma}$ | $s_e = \left(\frac{1}{1 + (\alpha \psi)^n} \right)^m$ | $s_e = \left(\frac{\psi_b}{\psi} \right)^\lambda$ |
| $K(\theta)$ | $k = k_s \frac{A}{A + \left(\frac{\alpha(\theta_s - \theta)}{\theta - \theta_r} \right)^{\beta/\gamma}}$ | $k = k_s \frac{A}{A + e^{\left(\frac{\alpha(\theta_s - \theta)}{\theta - \theta_r} \right)^{\beta/\gamma}}}$ | $k = k_s s_e^{1/2} (1 - (1 - s_e^{1/n})^m)^2$ | $k = k_s \left(\frac{\theta - \theta_r}{\theta_s - \theta_r} \right)^{\frac{-2-3\lambda}{\lambda}}$ |
| $K(\psi)$ | $k = k_s \frac{A}{A + \psi ^\beta}$ | $k = k_s \frac{A}{A + \psi ^\beta}$ | $k = k_s s_e^{1/2} \times (1 - (1 - s_e^{1/n})^m)^2$ | $k = k_s \left(\frac{\psi}{\psi_b} \right)^{-2-3\lambda}$ |
| $\Theta(\psi)$ | $\theta = \theta_r + s_e(\theta_s - \theta)$ | $\theta = \theta_r + s_e(\theta_s - \theta)$ | $\theta = \theta_r + s_e(\theta_s - \theta)$ | $\theta = \theta_r + s_e(\theta_s - \theta)$ |
| $\psi(\theta)$ | $\psi = - \left(\frac{\alpha(\theta_s - \theta)}{\theta - \theta_r} \right)^{1/\gamma}$ | $\psi = -e^{\left(\frac{\alpha(\theta_s - \theta)}{\theta - \theta_r} \right)^{1/\gamma}}$ | $\psi = \frac{1}{\alpha} \left(\left(\frac{\theta_s - \theta_r}{\theta - \theta_r} \right)^{1/m} - 1 \right)^{1/n}$ | $\psi = \frac{\psi_b}{\left(\frac{\theta_s - \theta_r}{\theta - \theta_r} \right)^{1/\lambda}}$ |
| $C(\psi)$ | $C(\psi) = \frac{\alpha(\theta_s - \theta_r)^\gamma \psi ^{r-1}}{(\alpha + \psi ^r)^2}$ | $C(\psi) = \frac{\alpha(\theta_s - \theta_r)^\gamma (\ln \psi)^{r-1} / \psi }{(\alpha + \psi ^r)^2}$ | $C(\psi) = \frac{\alpha m n (\theta_s - \theta_r) (\alpha \psi)^{n-1}}{(1 + (\alpha \psi)^n)^{m+1}}$ | $C(\psi) = -(\theta_s - \theta_r) \times \frac{\lambda}{\psi_b} \left(\frac{\psi}{\psi_b} \right)^{-(\lambda+1)}$ |
| Parameters | α, β, γ, A ---constant (L^0) k_s ---saturated hydraulic conductivity ($L T^{-1}$) θ_s ---saturated moisture content θ_r ---residual moisture content | | α ---constant (L^{-1}); m, n ---constant (L^0), with $m = 1 - 1/n$ | λ ---constant (L^0) ψ_b ---bubbling pressure (L). |

The first and second types of relationship were used by Haverkamp et al. (1977) for a sand and a Yolo light clay. The Haverkamp soil-moisture relationship fits moisture characteristics with large curvature reasonably better than the Brooks and Corey soil-moisture relationship (Lappala et al. 1987). However, the Haverkamp soil-moisture functions need four parameters (A, α, β, γ) to describe the k - h and θ - h relations, while the Brooks and Corey functions only need two parameters (λ, ψ_b). The van Genuchten

relationship has been reported to match experimental data more satisfactorily than the Brooks and Corey relationship. Two parameters (α , n) are also needed to describe the k-h and θ -h relation in the van Genuchten model.

In describing soil-moisture characteristics, effective saturation is introduced for convenience. Effective saturation is defined as

$$s_e(\theta) = \frac{\theta - \theta_r}{\theta_s - \theta_r} \quad (1-11)$$

where s_e is the effective saturation (L^0); θ is the volumetric moisture content(L^0); θ_s is the moisture content at saturated condition(L^0); θ_r is the residual moisture content(L^0).

1.2.5 Governing Equations

Plugging Equations 1-6 and 1-9 into Equation 1-1, we obtain

$$\rho(C(\psi) + S S_s) \frac{\partial \psi}{\partial t} = \frac{\partial}{\partial x_i} \left[\rho K_{ij} k_r(\psi) \left(\frac{\partial \psi}{\partial x_j} - \frac{\partial z}{\partial x_j} \right) \right] + \rho Q \quad (1-12)$$

Assuming that the water is incompressible and the overall storage coefficient $\eta = C(\psi) + S S_s$, then Equation 1-12 can be rewritten as

$$\eta(\psi) \frac{\partial \psi}{\partial t} = \frac{\partial}{\partial x_i} \left[K_{ij} k_r(\psi) \left(\frac{\partial \psi}{\partial x_j} - \frac{\partial z}{\partial x_j} \right) \right] + Q \quad (1-13)$$

This is the ψ -based governing equation, which can be used in solving both unsaturated and saturated flow.

For the unsaturated zone, specific storage S_s plays a relatively insignificant role in Equation 1-13. Thus the equation may be approximated as

$$C(\psi) \frac{\partial \psi}{\partial t} = \frac{\partial \theta}{\partial t} = \frac{\partial}{\partial x_i} \left[K_{ij} k_r(\psi) \left(\frac{\partial \psi}{\partial x_j} - \frac{\partial z}{\partial x_j} \right) \right] + Q \quad (1-14)$$

where $\theta = S\phi$ is the volumetric moisture content (the ratio of the water volume to the bulk volume of the porous medium). Equation 1-12 represents the mixed-form of the Richards' equation.

If a function called hydraulic diffusivity (L^2T^{-1}) is introduced as

$$D_y(\theta) = K_y k_r \frac{d\psi}{d\theta} \quad (1-15)$$

then Equation 1-12 can be rewritten as

$$\frac{\partial \theta}{\partial t} = \frac{\partial}{\partial x_i} \left[D_y \frac{\partial \theta}{\partial x_j} - K_y k_r(\theta) \frac{\partial z}{\partial x_j} \right] + Q \quad (1-16)$$

Equation 1-16 is the θ -based governing equation, which is valid only for vadose zone flow.

1.3 Initial and Boundary Conditions

The solution to the above governing equations requires that initial values of θ or ψ be specified everywhere in the solution domain R . According to Lappala et al. (1987), these initial conditions usually represent some type of steady state or equilibrium. If initial conditions are used that do not represent steady state, any simulation results will include transient effects from the difference between specified initial conditions and equilibrium conditions. For vadose zone flow, the equations are not linear. Therefore it is not possible to use the principle of superposition to subtract out the effects of transient initial conditions.

Boundary conditions must specify either the flux of water across the boundary or the head along the boundary. Given a domain $\Omega \in \mathcal{R}^2$ with a boundary Γ , the boundary conditions can be expressed as

$\psi = \psi_{B1}(t)$ along boundary Γ_D for the specified head (Dirichlet) boundary.

$q = q_{B2}(t)$ along boundary Γ_N for the specified flux or (Neumann) boundary.

$$\Gamma = \Gamma_D \cup \Gamma_N \text{ with } \Gamma_D \cap \Gamma_N = 0$$

1.4 Development of 1-D Vadose Zone Flow Model

In this study, we use a finite element Galerkin discretization in space and a finite difference discretization of the time derivative term to solve the one dimensional Richards' equation. The equation can be solved using the θ -based, ϕ -based or mixed-form of the equation.

1.4.1 Model for θ -based Form Equation

In Equation 1-16, θ , D_{ij} , k_r can be replaced by trial function of the form

$$\begin{aligned}\hat{\theta}(x_i, t) &= N_j(x_i)\theta_j(t), \\ \hat{D}_{ij}(x_i, t) &= N_j(x_i)D_{ijj}(t), \\ \hat{k}_r(x_i, t) &= N_j(x_i)k_{r,j}(t)\end{aligned}\tag{1-17}$$

where N is the trial function; i, j is dimension index ($=1, 2, 3$ for one-, two-, or three-dimensional problem respectively); J is node index, range from 1 to the number of nodes in an element (i.e. for a two-node element, $J=1, 2$, for a three-node element, $J=1, 2, 3$), here summation is implied.

Selecting the trial function for the test function, Equation 1-16 can be written in a weak weighted residual form as

$$\int_{\Omega} \left(\frac{\partial \theta}{\partial t} - \frac{\partial}{\partial x_i} \left[D_{ij} \frac{\partial \theta}{\partial x_j} - K_y k_r(\psi) \frac{\partial z}{\partial x_j} \right] + Q \right) N_i d\Omega = 0\tag{1-18}$$

Application of Green's Theorem leads to the discretized form of Equation 1-16

$$\begin{aligned}
& \int_{\Omega} N_I N_J \frac{d\theta_J}{dt} d\Omega + \int_{\Omega} \left[\hat{D}_y \left(\frac{\partial N_I}{\partial x_i} \frac{\partial N_J}{\partial x_j} \theta_J - K_y \hat{k}_r \frac{\partial N_I}{\partial x_i} \frac{\partial z}{\partial x_j} \right) \right] d\Omega - \\
& \int_{\Gamma} N_I \left(\hat{D}_y \frac{\partial \hat{\theta}}{\partial x_j} - K_y \hat{k}_r \frac{\partial z}{\partial x_j} \right) n_j d\Gamma - \int_{\Omega} N_I Q d\Omega = 0
\end{aligned} \tag{1-19}$$

where Ω is the solution domain with boundary $\Gamma = \Gamma_D \cup \Gamma_N$. It is understood that for the nodes on the boundary portion Γ_D , Equation 1-19 is replaced by the appropriate Dirichlet (prescribed pressure) boundary conditions introduced by modifying the global matrix. Without affecting the end result of the matrix formulation process, Equation 1-19 can now be replaced by the following equation, which incorporates the prescribed flux condition on boundary portion Γ_N .

$$[A] \left\{ \frac{d\theta}{dt} \right\} + [B] \{\theta\} = \{F\} \tag{1-20}$$

where matrices A, B and F can be calculated as

$$A_{IJ} = \sum_e \int_{\Omega^e} N_I N_J d\Omega \tag{1-21}$$

$$B_{IJ} = \sum_e \int_{\Omega^e} \hat{D}_y \frac{\partial N_I}{\partial x_i} \frac{\partial N_J}{\partial x_j} d\Omega \tag{1-22}$$

$$F_I = \sum_e \left(\int_{\Omega^e} K_y \hat{k}_r \frac{\partial N_I}{\partial x_i} \frac{\partial z}{\partial x_j} d\Omega + \int_{\Gamma_N} N_I \left(\hat{D}_y \frac{\partial \hat{\theta}}{\partial x_j} - K_y \hat{k}_r \frac{\partial z}{\partial x_j} \right) n_j d\Gamma + \int_{\Omega} N_I Q d\Omega \right) \tag{1-23}$$

The integration is conducted over an element 'e'.

Ju and Kung (1997) have shown that using higher order finite elements results in oscillatory behavior, so here we use a two-node linear element. This element is frequently referred to as a C_0 -linear element since it has zeroth-order continuity between elements.

The shape functions are given by:

$$\begin{aligned}
N_1^{(e)}(x) &= \frac{x_2 - x}{x_2 - x_1} \\
N_2^{(e)}(x) &= \frac{x - x_1}{x_2 - x_1}
\end{aligned} \tag{1-24}$$

Substituting Equation 1-24 into A_U , B_U and F_1 we get (the detailed derivations are listed in appendix A).

$$A^{(e)} = \begin{bmatrix} \frac{L_e}{3} & \frac{L_e}{6} \\ \frac{L_e}{6} & \frac{L_e}{3} \end{bmatrix} = \frac{L_e}{6} \begin{bmatrix} 2 & 1 \\ 1 & 2 \end{bmatrix} \tag{1-25}$$

$$B^{(e)} = \begin{bmatrix} \frac{\bar{D}}{2L_e} & \frac{\bar{D}}{2L_e} \\ \frac{\bar{D}}{2L_e} & \frac{\bar{D}}{2L_e} \end{bmatrix} = \frac{\bar{D}}{2L_e} \begin{bmatrix} 1 & -1 \\ -1 & 1 \end{bmatrix} \tag{1-26}$$

$$\begin{aligned}
F^{(e)}_1 &= \int_{x_1}^{x_2} K \hat{k}_r \frac{\partial N_1}{\partial x} \frac{\partial z}{\partial x} dx + \left[N_1 (K \hat{k}_r \frac{\partial \psi}{\partial x_j} - K \hat{k}_r \frac{\partial z}{\partial x}) \right]_{x_1}^{x_2} + \int_{x_1}^{x_2} N_1 Q dx \\
&= -K \frac{k_{r1} + k_{r2}}{2} + \frac{Q L_e}{2} + q_{in}(x_1) \\
F^{(e)}_2 &= \int_{x_1}^{x_2} K \hat{k}_r \frac{\partial N_2}{\partial x} \frac{\partial z}{\partial x} dx + \left[N_2 (K \hat{k}_r \frac{\partial \psi}{\partial x_j} - K \hat{k}_r \frac{\partial z}{\partial x}) \right]_{x_1}^{x_2} + \int_{x_1}^{x_2} N_2 Q dx \\
&= K \frac{k_{r1} + k_{r2}}{2} + \frac{Q L_e}{2} + q_{in}(x_2)
\end{aligned} \tag{1-27}$$

where $L_e = x_2 - x_1$; $\bar{D} = \frac{D_1 + D_2}{2}$; $q_{in}(x_1)$, $q_{in}(x_2)$ are the fluxes at node 1 and 2

respectively; k_{r1} , k_{r2} are the relative hydraulic conductivities at node 1 and 2

respectively.

1.4.2 Model for ψ -based Form Equation

For the ψ -based governing equation, η , Ψ , k_r can be represented by trial functions of the form

$$\hat{\psi}(x_i, t) = N_j(x_i)\psi_j(t),$$

$$\hat{\eta}(x_i, t) = N_j(x_i)\eta_j(t) \quad (1-28)$$

$$\hat{k}_r(x_i, t) = N_j(x_i)k_{r,j}(t)$$

Applying the Galerkin criterion and Green's theorem to Equation 1-13 results in

$$\begin{aligned} & \int_{\Omega} \hat{\eta} N_i N_j \frac{d\psi_j}{dt} d\Omega + \int_{\Omega} \left[K_{ij} \hat{k}_r \left(\frac{\partial N_i}{\partial x_i} \frac{\partial N_j}{\partial x_j} \psi_j - \frac{\partial N_i}{\partial x_i} \frac{\partial z}{\partial x_j} \right) \right] d\Omega - \\ & \int_{\Gamma} N_i K_{ij} \hat{k}_r \left(\frac{\partial \psi}{\partial x_j} - \frac{\partial z}{\partial x_j} \right) n_j d\Gamma - \int_{\Omega} N_i Q d\Omega = 0 \end{aligned} \quad (1-29)$$

Writing Equation 1-21 in matrix form,

$$[A] \left\{ \frac{d\psi}{dt} \right\} + [B] \{\psi\} = \{F\} \quad (1-30)$$

where matrices A, B and F can be calculated as

$$A_{ij} = \sum_e \int_{\Omega^e} \hat{\eta} N_i N_j d\Omega \quad (1-31)$$

$$B_{ij} = \sum_e \int_{\Omega^e} K_{ij} \hat{k}_r \frac{\partial N_i}{\partial x_i} \frac{\partial N_j}{\partial x_j} d\Omega \quad (1-32)$$

$$F_i = \sum_e \left(\int_{\Omega^e} K_{ij} \hat{k}_r \frac{\partial N_i}{\partial x_i} \frac{\partial z}{\partial x_j} d\Omega + \int_{\Gamma_N} N_i (K_{ij} \hat{k}_r \frac{\partial \psi}{\partial x_j} - K_{ij} \hat{k}_r \frac{\partial z}{\partial x_j}) n_j d\Gamma + \int_{\Omega} N_i Q d\Omega \right) \quad (1-33)$$

Plugging Equation 1-19 into A_{ij}, B_{ij}, we get

$$A^{(e)} = \frac{L_e}{12} \begin{bmatrix} 3\eta_1 + \eta_2 & \eta_1 + \eta_2 \\ \eta_1 + \eta_2 & \eta_1 + 3\eta_2 \end{bmatrix} \quad (1-34)$$

$$B^{(e)} = \begin{bmatrix} \frac{\bar{K}}{2L_e} & \frac{\bar{K}}{2L_e} \\ \frac{\bar{K}}{2L_e} & \frac{\bar{K}}{2L_e} \end{bmatrix} = \frac{\bar{K}}{2L_e} \begin{bmatrix} 1 & -1 \\ -1 & 1 \end{bmatrix} \quad (1-35)$$

$F^{(e)}$ can be expressed in the same two parts as in Equations 1-27.

1.4.3 Model for Mixed-form Equation

In the mixed-form of Richards' equation, the term $\partial\theta^{k+1,m+1}/\partial t$ is expressed as:
(Celia et al., 1990; Rathfelder et al., 1994)

$$\frac{\partial\theta^{k+1,m+1}}{\partial t} = \frac{\theta^{k+1,m+1} - \theta^k}{\Delta t} \quad (1-36)$$

where $k, k+1$ are the previous and current time step respectively; $m, m+1$ are the previous and current iteration times respectively in current time step $k+1$; $\theta^{k+1,m+1}$ is the moisture content at current iteration of current time step.

The $\theta^{k+1,m+1}$ can be expanded by Taylor series about ψ_i^m :

$$\theta^{k+1,m+1} \approx \theta^{k+1,m} + C^{k,m}(\psi^{k+1,m+1} - \psi^{k+1,m}) \quad (1-37)$$

Plugging Equations 1-36 and 1-37 into Equation 1-14, the following equation is obtained:

$$\frac{\theta^{k+1,m} + C^{k,m}(\psi^{k+1,m+1} - \psi^{k+1,m}) - \theta^k}{\Delta t} = \frac{\partial}{\partial x_i} \left[K_{ij} k_r(\psi) \left(\frac{\partial \psi}{\partial x_j} - \frac{\partial z}{\partial x_j} \right) \right] + Q \quad (1-38)$$

After some arrangement, we get:

$$\frac{C^{k,m}(\psi^{k+1,m+1} - \psi^{k+1,m})}{\Delta t} = \frac{\partial}{\partial x_i} \left[K_{ij} k_r(\psi) \left(\frac{\partial \psi}{\partial x_j} - \frac{\partial z}{\partial x_j} \right) \right] + Q + \frac{d\theta^m}{dt} \quad (1-39)$$

In the mixed-form, θ, ψ, k_r are represented by trial functions of the form

$$\hat{\psi}(x_i, t) = N_j(x_i) \psi_j(t),$$

$$\hat{\theta}(x_i, t) = N_j(x_i) \theta_j(t) \quad (1.40)$$

$$\hat{k}_r(x_i, t) = N_j(x_i) k_{r,j}(t)$$

Applying the Galerkin criterion and Green's theorem to Equation 1-39 results in

$$\begin{aligned}
& \frac{1}{\Delta t} \int_{\Omega} C^{k,m} N_I N_J (\psi_J^{k+1,m+1} - \psi_J^{k+1,m}) d\Omega \\
& + \int_{\Omega} \left[K_y \hat{k}_r \left(\frac{\partial N_I}{\partial x_i} \frac{\partial N_J}{\partial x_j} \psi_J - \frac{\partial N_I}{\partial x_i} \frac{\partial z}{\partial x_j} \right) \right] d\Omega = \\
& \int_{\Gamma} N_I K_y \hat{k}_r \left(\frac{\partial \psi}{\partial x_j} - \frac{\partial z}{\partial x_j} \right) n_i d\Gamma + \int_{\Omega} N_I Q d\Omega - \int_{\Omega} N_I N_J \frac{d\theta_J^m}{dt} d\Omega
\end{aligned} \tag{1-41}$$

This can be written in matrix form as:

$$\frac{1}{\Delta t} [A](\psi^{k+1,m+1} - \psi^{k+1,m}) + [B]\{\psi^{m+1}\} = \{F\} - [E] \frac{d\{\theta\}^m}{dt} \tag{1-42}$$

where matrices A, B and F can be calculated as

$$A_{IJ} = \sum_e \int_{\Omega^e} \hat{C} N_I N_J d\Omega \tag{1-43}$$

$$B_{IJ} = \sum_e \int_{\Omega^e} K_y \hat{k}_r \frac{\partial N_I}{\partial x_i} \frac{\partial N_J}{\partial x_j} d\Omega \tag{1-44}$$

$$E_{IJ} = \sum_e \int_{\Omega^e} N_I N_J d\Omega \tag{1-45}$$

$$F_I = \sum_e \left(\int_{\Omega^e} K_y \hat{k}_r \frac{\partial N_I}{\partial x_i} \frac{\partial z}{\partial x_j} d\Omega + \int_{\Gamma_n} N_I (K_y \hat{k}_r \frac{\partial \psi}{\partial x_j} - K_y \hat{k}_r \frac{\partial z}{\partial x_j}) n_i d\Gamma + \int_{\Omega} N_I Q d\Omega \right) \tag{1-46}$$

For the mixed-form governing equation, the matrices [A], [B] and vector {F} are the same as those obtained from the ψ -based governing equation. Additionally, in this case the matrix [E] is the same as the matrix [A] obtained from θ -based governing equation:

$$E^{(e)} = \begin{bmatrix} \frac{L_e}{3} & \frac{L_e}{6} \\ \frac{L_e}{6} & \frac{L_e}{3} \end{bmatrix} = \frac{L_e}{6} \begin{bmatrix} 2 & 1 \\ 1 & 2 \end{bmatrix} \tag{1-47}$$

1.4.4 Issues Concerning the Numerical Model

When simulating water flow in the vadose zone using the head-based or mixed-form of the governing equation, the consistent mass scheme may cause unstable oscillations, while the lumped mass scheme with linear elements can successfully simulate water movement in unsaturated soils with low initial water content without causing any numerical oscillation (Milly, 1985; Celia, 1990; Abriola and Rathfelder, 1993; Ju and Kung, 1997). Two kinds of lumped schemes, namely “L1” and “L2” schemes (after Milly, 1985), are used in this study.

The “L1” scheme is obtained by replacing the integral of $A^{(e)}$ in Equation 1-34 by the expression:

$$A^{(e)}_{ij} = \delta_{ij} \int_{x_1}^{x_2} \hat{\eta} N_i dx \quad (i,j = 1,2) \quad (1-48)$$

After plugging $\hat{\eta}$ and N_i into this equation, one gets the lumped capacity matrix:

$$A^{(e)} = \frac{L_e}{6} \begin{bmatrix} 2\eta_1 + \eta_2 & 0 \\ 0 & \eta_1 + 2\eta_2 \end{bmatrix} \quad (1-49)$$

The “L2” scheme is obtained by replacing the integral in Equation 1-34 by the expression:

$$A^{(e)}_{ij} = \delta_{ij} \eta_i \int_{x_1}^{x_2} N_i dx \quad (i,j = 1,2) \quad (1-50)$$

After plugging η_i and N_i into this equation, one gets the lumped capacity matrix:

$$A^{(e)} = \frac{L_e}{2} \begin{bmatrix} \eta_1 & 0 \\ 0 & \eta_2 \end{bmatrix} \quad (1-51)$$

For mixed-form, the E matrix can also be lumped as:

$$E^{(e)} = \begin{bmatrix} \frac{L_e}{2} & 0 \\ 0 & \frac{L_e}{2} \end{bmatrix} = \frac{L_e}{2} \begin{bmatrix} 1 & 0 \\ 0 & 1 \end{bmatrix} \quad (1-52)$$

For comparison, the expressions for the matrices A and E for various lumping schemes are summarized in Table 1-2.

Table 1-2. Capacity matrices A and E for different lumping schemes

| Lumping scheme code in this study | Capacity matrix A (for head- based and mixed-form) | Matrix E (for mixed-form only) |
|--------------------------------------|-----------------------------------------------------------------------------------------------------------------------------------|------------------------------------------------------------------------|
| 0 (consistent) | $A^{(e)} = \frac{L_e}{12} \begin{bmatrix} 3\eta_1 + \eta_2 & \eta_1 + \eta_2 \\ \eta_1 + \eta_2 & \eta_1 + 3\eta_2 \end{bmatrix}$ | $E^{(e)} = \frac{L_e}{6} \begin{bmatrix} 2 & 1 \\ 1 & 2 \end{bmatrix}$ |
| 1 (L1) | $A^{(e)} = \frac{L_e}{6} \begin{bmatrix} 2\eta_1 + \eta_2 & 0 \\ 0 & \eta_1 + 2\eta_2 \end{bmatrix}$ | $E^{(e)} = \frac{L_e}{2} \begin{bmatrix} 1 & 0 \\ 0 & 1 \end{bmatrix}$ |
| 2 (L2) | $A^{(e)} = \frac{L_e}{2} \begin{bmatrix} \eta_1 & 0 \\ 0 & \eta_2 \end{bmatrix}$ | $E^{(e)} = \frac{L_e}{2} \begin{bmatrix} 1 & 0 \\ 0 & 1 \end{bmatrix}$ |

In solving Equations 1-20, 1-30 and 1-42, several factors should be considered:

(1) The θ -based governing equation is only suitable for the unsaturated zone, because in the saturated-zone θ does not vary with pressure head and therefore the hydraulic diffusivity D_{ij} which depends on $\partial\psi/\partial\theta$ will go to infinity.

(2) When using the ψ -based governing equation, caution should be practiced because mass balance may be a problem especially for dry initial conditions. To solve this problem, very small space and time steps can be used. Obviously this will greatly increase computational requirements. Another solution is to use the mass-balance approach (Yeh, 1981; Milly, 1985; Celia et al., 1990; Abriola and Rathfelder, 1993; Rathfelder and Abriola, 1994). In this approach, the storage coefficient is evaluated as an effective, or average, value over the element and over the duration of the time step (Milly, 1985).

(3) When using FEM to solve for θ or ψ , higher order test functions unavoidably produce oscillatory results (Ju and Kung, 1997), so in this research only lower order test functions are used. Using a consistent capacity matrix A is also prone to oscillatory results, and therefore for this work a lumped capacity matrix A is recommended, although a consistent capacity matrix A can also be used.

(4) Equations 1-20, 1-30 and 1-42 are nonlinear because matrices A , B and F are functions of θ or ψ . To solve nonlinear equations, usually the Picard method, Newton-Raphson Method or Modified Newton Method are used. Using these methods, a system of linearized equations can be obtained. The Picard method has a first-order convergence rate, and the left hand side matrix is symmetric and positive definite, so the equation can be solved using the highly efficient Preconditioned Conjugated Gradient (PCG) method. The Newton-Raphson Method requires calculating the Jacobian matrix, however, the Newton-Raphson Method converges much more rapidly than the Picard method.

1.5 Convergence Criteria and Mass Balance Calculation

Huang et al. (1996) proposed a soil-moisture-based convergence criterion derived using a Taylor series expansion of the water content and found the new nonlinear convergence criterion to be much more computationally efficient and robust than the other two criteria of their comparison. However, when ponding occurs when precipitation rate is greater than infiltration rate and part of the vadose zone becomes saturated, the soil-moisture-based convergence criterion is no longer valid. Thus the convergence criteria used here follows that by Rathfelder and Abriola (1994).

$$\max \frac{|\psi^{m+1} - \psi^m|}{|\psi^{m+1}|} \leq eps \quad (1-53)$$

where *eps* is convergence criteria.

Following the work done by Rathfelder and Abriola (1994), the global mass balance error is calculated by

$$error(\%) = 100 \left| 1.0 - \frac{M_t - M_0}{\sum F_{\Delta t}} \right| \quad (1-54)$$

where M_t is the mass storage at time t , M_0 is the initial mass storage at time zero, and $F_{\Delta t}$ is the mass entering the computation domain during the time step Δt . M_t and $F_{\Delta t}$ are calculated by the method of Liedl et al. (1996).

$$M_{t+\Delta t} = \theta_0 \frac{\Delta z_{1/2}}{2} + \sum_{i=1}^{n-1} \theta_i \Delta z_i + \theta_n \frac{\Delta z_{n-1/2}}{2} \quad (1-55)$$

$$F_{\Delta t} = (q_0 - q_n) \Delta t \quad (1-56)$$

where θ_0 is the moisture content at first node; θ_n is the moisture content at last node; q_0 is the flux at boundary at first node; q_n is the flux at last node; Δz_i is the segment length including node i (half the length from node $i-1$ to i , and half the length from node i to $i+1$). The boundary fluxes may be calculated as

$$q_0 = q_{1/2} + (\theta_{0,m} - \theta_{0,m+1}) \frac{\Delta z_{1/2}}{2\Delta t} \quad (1-57)$$

$$q_n = q_{n-1/2} + (\theta_{n,m} - \theta_{n,m+1}) \frac{\Delta z_{1/2}}{2\Delta t} \quad (1-58)$$

where $\theta_{0,m}$ is the moisture content at first node at previous time level m ; $\theta_{0,m+1}$ is the moisture content at first node at this time level $m+1$; $\theta_{n,m}$ is the moisture content at last node at previous time level m , $\theta_{n,m+1}$ is the moisture content at last node at this time level $m+1$; $q_{1/2}$ and $q_{n-1/2}$ are the water fluxes through the first and last element.

The water flux through an element can be calculated as

$$q_{i+1/2} = -K_{i+1/2} \left(\frac{\psi_{i+1} - \psi_i}{\Delta z_{i+1/2}} - 1 \right) \quad i=0, 1, 2, \dots, n-1 \quad (1-59)$$

Table 1-3. Parameter values for five types of soil used in examples

| Soil | Type | Function | $K_s(\text{cm/s})$ | A | α / ψ_b | β/n | γ | θ_s | θ_r |
|-----------|------|-----------|------------------------|---------------------|-----------------------|-----------|----------|------------|------------|
| Sand | 1 | Haverkamp | 9.440×10^{-3} | 1.175×10^6 | 1.611×10^6 | 4.747 | 3.960 | 0.2870 | 0.0750 |
| Yolo | 2 | Haverkamp | 1.230×10^{-5} | 1.246×10^2 | 7.390×10^2 | 1.770 | 4.000 | 0.4950 | 0.1240 |
| Berino | 3 | V-G | 6.261×10^{-3} | --- | 2.8×10^{-3} | 2.2390 | --- | 0.3658 | 0.0286 |
| Glendale | 4 | V-G | 1.516×10^{-4} | --- | 1.04×10^{-2} | 1.3954 | --- | 0.4686 | 0.1060 |
| Clay loam | 5 | B-C | 8.750×10^{-4} | --- | -5.4 | 0.2 | --- | 0.52 | 0.0 |

1.6 Verification of the Model

In this study, several types of soil were used in the verification examples. Table 1-3 summarizes the soil moisture characteristic parameters for each soil. The hydraulic properties of each soil are described by one of the three relations, the Haverkamp relations; the Van Genuchten (V-G) relations and the Brooks-Corey (B-C) relations.

1.6.1 Example Problem 1

The first example is taken from the VS2DT documentation (Lappala et al., 1987). This is a problem of one-dimensional vertical infiltration into a soil with uniform initial pressure head of -130 cm. The soil is Glendale clay loam (Soil Type 5 in Table 1-3). Its hydraulic properties were modeled with the Brooks and Corey equations. H_b , λ , θ_s , θ_r and K_s were -5.4 cm; 0.2; 0.52; 0.0 and 8.75×10^{-4} cm/sec, respectively. At 0 hours a constant

pressure head, equal to -5.4 cm, was applied to the uppermost node. The pressure head at the bottom node did not change through the simulation period. The length of the simulated column was 60 cm.

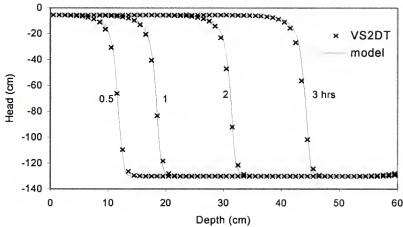


Figure 1-1. Comparison of head profiles calculated by VS2DT and model developed in this study for an infiltration problem with specified head of -5.4 cm at the top boundary.

For this example, the fully implicit head-based form of Richards' equation with lump parameter equal to 2 was used. Figure 1-1 shows that the results from VS2DT and the model developed in this study are very similar, with the VS2DT model showing slightly more dispersion of the wetting front.

1.6.2 Example Problem 2

For the second example problem, simulation results are compared to experimental results by Haverkamp et al. (1977) for vertical infiltration of water into sand.

The hydraulic properties for the soil were selected from soil Type 1 in Table 1-3. A 70 cm soil column was used. A constant soil moisture content of $0.10 \text{ cm}^3/\text{cm}^3$ was used as the initial condition for this experiment. Water was applied to the upper boundary at a constant rate of 13.69 cm/h through the experiment. The bottom boundary was fixed at a moisture content of 0.1 through the experiment.

The model was run with a fully implicit scheme and the “L₂” lump scheme. The results from this model are shown in Figure 1-2 along with the experimental data. The simulated results, which are very similar to those by Haverkamp et al. (1977), agree reasonably well with experimental data except that the wetting front from the experiment moves a little more rapidly than the simulated wetting front.

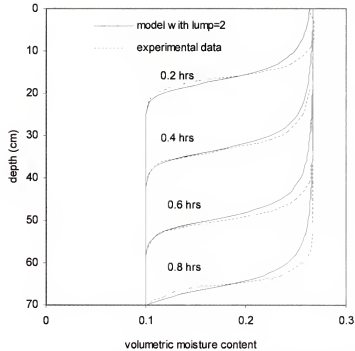


Figure 1-2. Comparison of the infiltration profiles from experimental data and running the model with lump=2 for an infiltration problem with specified flux of 13.69 cm/h at the top boundary.

1.6.3 Example Problem 3

This example compares the numerical model developed in this study to the analytical solution developed by Srivastava and Yeh (1991). The dependence of hydraulic conductivity and the moisture content on the pressure head is assumed to be described by a power function:

$$K = K_s e^{a\psi} \quad \text{and} \quad \theta = \theta_r + (\theta_s - \theta_r) e^{a\psi}$$

where K_s is the saturated hydraulic conductivity (L/T); θ_s is the saturated moisture content (L^3); θ_r is the residual moisture content (L^3); and α is the soil pore-size distribution parameter (L^{-1}).

Table 1-4. Parameter values for two types of soil used in examples

| Problem no | Thickness of zone (cm) | K_s (cm/hr) | α (cm^{-1}) | θ_s | θ_r | q_a (cm/hr) | q_b (cm/hr) | ψ_0 (cm) |
|------------|------------------------|---------------|------------------------|------------|------------|---------------|---------------|---------------|
| 1 | 100 | 1.0 | 0.1 | 0.40 | 0.06 | 0.1 | 0.9 | 0 |
| 2 | 100 | 1.0 | 0.01 | 0.45 | 0.2 | 0.1 | 0.9 | 0 |

In this example, two problems are solved that have the same soil parameters except α . In both problems, the thickness of the homogeneous soil is 100 cm. The saturated hydraulic conductivity was 1.0 cm/hr. and the α values were 0.1 cm^{-1} and 0.01 cm^{-1} , respectively. The saturated and residual water contents of the soil, with $\alpha=0.1$, were taken as 0.40 and 0.06, respectively; for $\alpha=0.01$ they were 0.45 and 0.2. The initial pressure head profile was the steady state infiltration profile at an infiltration rate q_a equal to 0.1 cm/h. Then, after time zero of the simulation, the infiltration rate q_b was increased to 0.9 cm/h (see Table 1-4) for the duration of simulation. The bottom boundary was a fixed head boundary with pressure equal to zero (i.e. a water table boundary).

For each example (one with higher infiltration capacity $\alpha=0.01$, and one with lower infiltration capacity $\alpha=0.1$) the model was run twice with fully implicit schemes and two lumping techniques. Figures 1-3 and 1-4 show that both schemes give results close to the analytical solution by Srivastava and Yeh (1991) with the consistent mass scheme (L0) giving better results. For the “L2” lumping scheme, at the onset of infiltration, the solution deviates somewhat from the analytical solution. This deviation becomes smaller as infiltration proceeds.

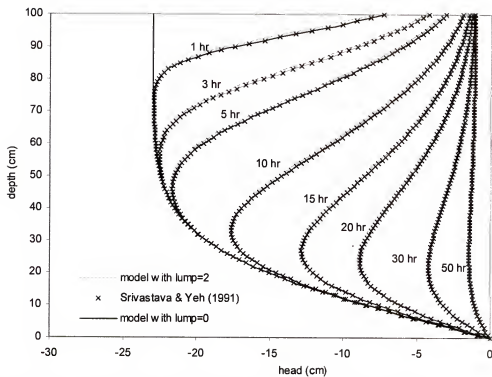


Figure 1-3. Comparison of head profiles from the analytical solution by Srivastava and Yeh (1991) and this model, for a homogeneous soil with $\alpha=0.1$.

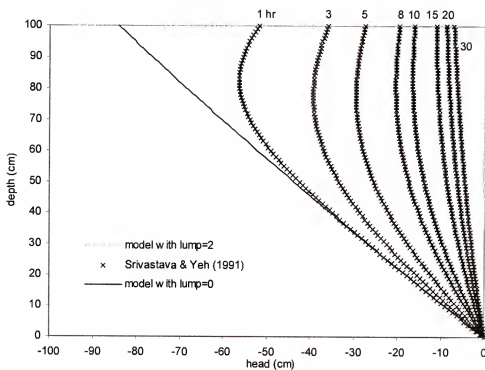


Figure 1-4. Comparison of head profiles from the analytical solution by Srivastava and Yeh (1991) and this model, for a homogeneous soil with $\alpha=0.01$.

1.6.4 Example Problem 4

This example compares results from the numerical model developed by Gottardi and Venutelli (1993) to the numerical solution developed in this study. The hydraulic properties and Haverkamp function values for the soil were selected from soil type “1” in Table 1-3. The initial head was uniformly set at -100 cm except the uppermost node, which had a head of -50 cm. The head of the bottom boundary was -100 cm and kept unchanged during the whole simulation period. After time zero, a constant flux equal to 0.0045 cm/sec was applied to the uppermost node. The length of the simulated column was 120 cm.

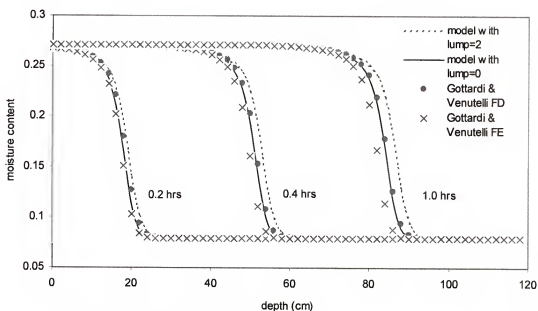


Figure 1-5. Moisture profiles at times 0.2, 0.4 and 1.0 hours for a homogeneous soil with constant flux at the top of the column and constant head at the bottom of the column.

The head-based form of our model with a time weighting factor of 0.5 and both the consistent and “L2” lumping schemes were compared to the Gottardi and Venutelli (1993) model with both the FD (finite difference) and FE (finite element) scheme. Figure

1-5 shows that the consistent mass scheme (lump = 0) gives results very similar to that of the FD scheme of Gottardi and Venutelli model, while the L2 lumping scheme of our model gives results showing faster moving infiltration fronts. Comparison of the mass balance error of our model with those of Gottardi and Venutelli model indicates that the mass balance errors of our model are much smaller than those of Gottardi and Venutelli model. This difference may result from two factors: (1) Gottardi and Venutelli (1993) calculated specific moisture capacity by derivative rather than the chord-slope method; (2) Gottardi and Venutelli (1993) calculated the mass balance using an expression which may not be very suitable for specified flux boundary conditions.

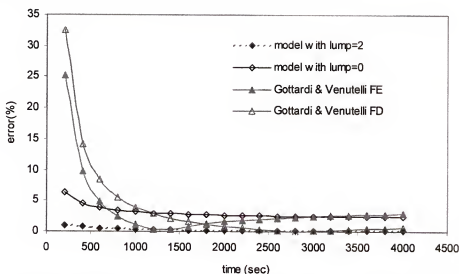


Figure 1-6. Mass balance error vs time for different method for a homogeneous soil with constant flux at the top of the column and constant head at the bottom of the column.

1.6.5 Example Problem 5

This example is also from Gottardi and Venutelli (1993). It includes two problems of infiltration into an unsaturated layered soil column, 75 cm in depth. The first example used a specified pressure head boundary condition, and the second used a specified flux boundary condition. For each of the problems, five 15 cm layers were utilized. Starting

from the top of the soil column the different types of soil used for each layer were: sand, Glendale clayloam, Berino loamy fine sand, Yolo light clay and Sand, as given in Table 1-3. For both problems, the initial head was set at -600 cm uniformly except for the uppermost node, which had a head of -20 cm. The head at the bottom boundary was -600 cm and kept unchanged during the whole simulation period. For the first problem, the specified head for the upper boundary was -20 cm during the whole simulation period. The specified flux of the upper boundary for the second problem was 0.0001 cm/sec.

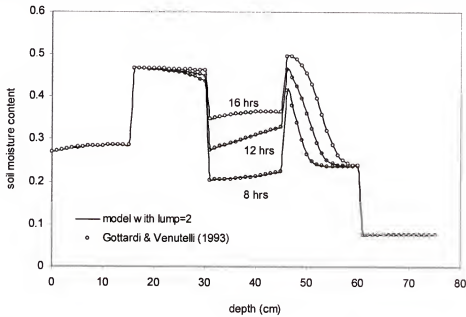


Figure 1-7. Moisture profiles at 8, 12 and 16 hours from numerical solution by Gottardi and Venutelli (1993) and this model with $\text{lump}=2$ for layered soils with specified head of -20 cm at the top boundary.

This example demonstrates the ability of the model developed in this research to simulate water flow in unsaturated layered soils. Figures 1-7 and 1-8 show that the results of our model are very similar to that of Gottardi and Venutelli model. Again, the model generates much less mass balance error than Gottardi and Venutelli model (Figures 1-9 and 1-10).

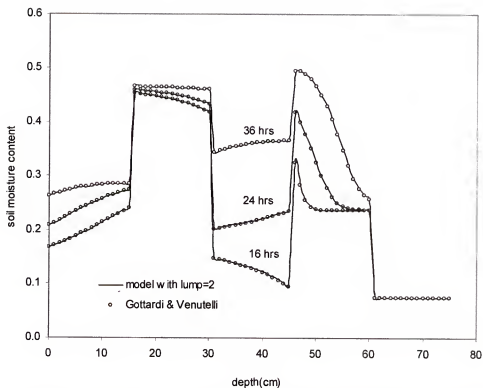


Figure 1-8. Moisture profiles at 16, 24 and 36 hours from numerical solution by Gottardi and Venutelli (1993) and this model with lump=2 for layered soils with specified flux of 0.0001 cm/sec at the top boundary.

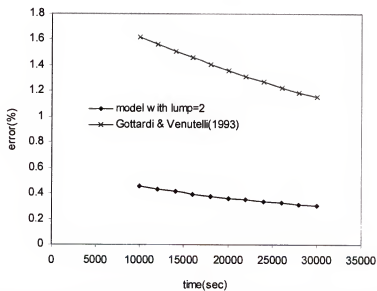


Figure 1-9. Mass balance error with time from numerical solution by Gottardi and Venutelli (1993) and this model with lump=2 for layered soils with specified head of -20 cm at the top boundary.

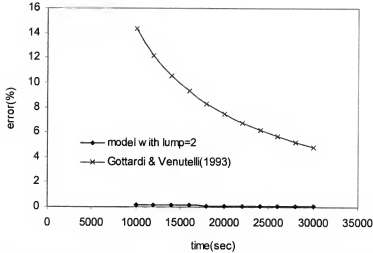


Figure 1-10. Mass balance error with time from numerical solution by Gottardi and Venutelli (1993) and this model with lump=2 for layered soils with specified flux of 0.0001 cm/sec at the top boundary.

1.7 Discussions and Conclusions

In this chapter, the accuracy of the model developed in this study was verified by comparing its simulation results with simulation results from other numerical models (Examples 1, 4 and 5), experimental data (Example 2) and analytical solutions (Example 3) from the literature. The model can simulate water flow in both single- and multi-soil layers with good mass balance (Examples 4 and 5).

The model developed in this study provides many choices to select from according to the practical problems which must be solved. As far as the forms of governing equation, three types can be selected, namely, moisture (θ) based, head (ψ) based, or the mixed-form. For the head-based or the mixed-form of the governing equation, one can choose either the lumped or the consistent method. One can also select the weighting factor to choose fully-implicit, semi-implicit or explicit techniques.

The head-based form of the governing equation is preferred because it is continuous in multi-layered soil, and can be used in modeling both saturated and vadose

zone flow. However, mass balance has been reported as a problem for the head-based form (Celia et al., 1990; Milly, 1985; Yeh, 1981; Berg, 1999; Abriola and Rathfelder, 1994) in very dry soil conditions. In this study, numerical experiments showed that the fully implicit scheme with “L2” lumping (second lumped method), which is similar to the fecs method of Abriola and Rathfelder(1994), generates good mass balance when the capacity matrix is calculated using the chord-slope approximation. The numerical experiments also showed that lumped method can increase the speed of convergence and stability.

CHAPTER 2 WATER-PLANT-ATMOSPHERE MODEL

2.1 Introduction

On a global basis, approximately 70% of the precipitation striking the earth's surface eventually returns to the atmosphere by evaporation from soils, water bodies and wetted canopies, and transpiration from plants (Burman and Pochop, 1994; Molz, 1981). In arid regions, the percentage is higher and may reach up to 90%. Therefore, there is a need for hydrologists to further develop their quantitative understanding of water movement in plant and soil-plant systems (Molz, 1981).

2.1.1 Evaporation

Evaporation from the soil surface is controlled by meteorological and soil conditions (Lappala et al., 1987; Yakirevich et al., 1997) and is known to occur in many stages (Jensen et al., 1990; Bond and Willis, 1970). Jensen et al. (1990) identified two stages. The first stage is characterized by a wet soil surface and known as the *constant rate stage* during which evaporation occurs at the rate of the climatic potential. The second stage is known as the *falling rate stage* during which evaporation is largely controlled by the ability of the soil profile to transport water towards the evaporation zone. Bond and Willis (1970) identified a third stage, which is characterized by slow rates from a dry soil profile. During the third stage, the soil suction reaches a nearly constant level.

The *constant rate* stage occurs when the soil surface is wet following an irrigation or significant rain. During the first stage, surface resistance can be neglected and the

evaporation rate remains constant because the soil profile can supply the water fast enough to continuously replenish the water which is evaporated to the atmosphere. The *falling rate* stage is characterized by a dry layer at the ground surface. The evaporation rate decreases because upward water movement is mainly by vapor diffusion. When the moisture at the soil surface approaches equilibrium with the overlying atmosphere, the water potential gradient towards the soil surface is not great enough to compensate for the decrease in soil conductivity upon drying. The third stage may also be considered to be the continuous progression of the second stage.

2.1.2 Transpiration

Transpiration is the process of vaporization of liquid water contained in plant tissues and the vapor transport to the atmosphere. The vaporization occurs within the leaves, namely in the intercellular spaces, and the vapor exchange with the atmosphere is controlled by the stomata aperture. Nearly all water taken up from the soil profile is lost by transpiration and only a small fraction is used within the plants (Allen et al., 1998).

Transpiration, like direct evaporation, depends on meteorological conditions such as energy supply, vapor pressure deficit and wind speed. Hence, radiation, air temperature, air humidity and wind terms should be considered when assessing transpiration. The soil water content, the ability of the soil to conduct water to the roots and the ability of water transport within plants also determine the transpiration rate (Allen et al., 1998).

Evaporation and transpiration occur simultaneously and there is no easy way to distinguish the two processes. Apart from the water availability in the root zone, the evaporation from a vegetated soil is mainly controlled by the fraction of the solar radiation reaching the soil surface. This fraction decreases over the growing season as the

vegetation develops and the vegetative canopy shades more and more of the ground area. When the vegetation is small, water is predominately lost by soil evaporation, but once the vegetation is well developed and completely covers the soil, transpiration becomes the main process (Allen et al., 1998). For a wet soil surface, soil evaporation is less than 5% of total evapotranspiration when LAI is greater than 4 and may be higher than 50% when LAI is less than 2 (Radersma and de Ridder, 1996).

2.1.3 Factors that influence Evapotranspiration

Many factors influence the evapotranspiration rate. Factors from meteorological conditions include solar radiation, vapor pressure deficit and wind speed. Factors from soil include water availability and soil physical characteristics. Landuse plays a great role in changing local and global environments in general and water balance in particular (McNaughton and Jarvis, 1983). Evapotranspiration may be higher from land occupied with perennial crops than with annual crops. This may be due to four factors: (1) the lower aerodynamic resistance of perennial crops compared with annual species; (2) the much higher interception of precipitation from land occupied with perennial crops. Intercepted water evaporates at a potential rate since no resistance exists (McNaughton and Jarvis, 1983); (3) the transpiration characteristics among plant species, e.g. differences in stomatal behavior in relation to light intensity, CO₂ concentration, temperature, vapor pressure deficit of the air, and leaf water potential (Radersma and Ridder, 1996); (4) differences in the reflectance of solar radiation and thus net radiation may vary among different canopies. More radiation is absorbed by forests than by crops/herbaceous vegetation.

Certainly the influence of reflection varies among plants. Radersma and Ridder (1996) found that the influence of reflection coefficients is small compared with

difference in surface resistances of crops when the aerodynamic resistance is below 20 s/m. For annual crops with higher values of aerodynamic resistance, differences in reflection coefficient are more important.

Soil moisture content influences not only hydraulic conductivity and thus the water vapor flow rate from soil surface to atmosphere and water transport from soil to plant, but also the reflectance of the soil surface. Researchers (Idso et al., 1975; Graser and Van Bavel, 1982) have found a strong relationship between reflectance and soil water content. After studying and comparing the albedo-water moisture relationship and albedo-water potential relationship, Graser and van Bavel (1982) stated that albedo may be more generally related to water potential than to water content.

2.1.4 Models of Water Uptake by Plants

Water uptake by plant roots greatly influences transport of water and chemicals in soil-plant system, and has a substantial effect on crop yields, as well as the quality and quantity of water recharged to groundwater systems under croplands (Schmidhalter et al. 1994). Most models simulating soil water movement with plant water uptake have adopted a macroscopic approach in which water extraction by plant roots is treated as a sink term distributed in the root zone (Childs, 1977; Feddes et al., 1978; Wu et al. 1999). Childs et al. (1977) developed a mathematical model to simulate the environmental and physical processes involved in the growth of corn. Potential evaporation was estimated from potential evapotranspiration using a Beer's law analogy to calculate the amount of energy available for evaporation at the soil surface. Actual evaporation was calculated using the potential surface flux rate and Darcy's Law (Nimah and Hanks, 1973). Actual transpiration (T_a) was calculated from potential transpiration (T_p), which is the difference between potential evapotranspiration and potential evaporation, using an electrical

resistance analogue. This approach to calculate T_a is the basis of the approach used in many widely used models such as the VS2DT model (Lappala et al., 1987).

The Feddes model (Feddes et al., 1978) takes into account the effect of soil water stress on root water extraction by introducing a reduction coefficient dependent on soil water potential. However, no consideration was given to the variation of the maximum root water extraction rate with the depth in the root zone by such factors as the growth of roots and shoots of annual plants and water stress on the growth of plants (Wu et al., 1999).

Prasad (1988) modified Feddes' model to allow variation of the maximum root water extraction rate with depth using a linear function to represent the root density distribution. However, discrepancies still existed between observed and simulated water depletions using the linear model of maximal root water extraction distribution (Prasad, 1988). A linear distribution function may not be adequate in the description of root activity distribution of various plant species. A nonlinear distribution function based on root density distributions seems likely to bring better agreement between observed and simulated results (Wu et al., 1999).

Clemente et al. (1994) compared three models (SWATRE, LEACHW, and SWASIM) which handle the root extraction terms in different ways. SWATRE (soil water and actual transpiration rate, extended, Belmans et al., 1983) is a water balance model, which simulates transient vertical flow in a heterogeneous soil profile. In this model, the actual water uptake by plants is determined by the maximum possible water extraction by plant roots and a restriction factor, which is a function of pressure head (Feddes et al., 1978). LEACHW (Wagenet and Huston, 1989) water flow model is one of

four separate submodels of the LEACHM (Leaching Estimation and Chemistry Model) package. In this model, the plant root extraction term $S(h,z)$ is described by the expression proposed by Wagenet and Huston (1989). The SWASIM (Soil Water Simulation Model, Hayhoe and De Jong, 1982) is based on the one-dimensional transient water-content based form of Richards' equation. The sink term for water uptake takes into account the rooting density distribution. The results of Clemente et al. (1994) showed that all models produced acceptable predictions and none of the models was consistently more accurate than the others.

2.2 Potential Evaporation and Transpiration

Potential evapotranspiration is the rate at which water is removed from the soil surface or soil profile without restriction of available soil water. In numerical simulations, evaporation and transpiration are handled differently. Evaporation from soil is basically controlled by atmospheric and soil conditions and is simulated as a boundary condition. Transpiration by plants is controlled by atmospheric conditions and the water potential difference between the soil profile and plant roots and is simulated as an interior water sink.

For soils covered with canopies, the potential evapotranspiration can be calculated by Penman-Monteith equation (Monteith, 1981). Then, total evapotranspiration is distributed between evaporation from soil and transpiration from plants. For bare soil, The potential evaporation can be calculated by the Penman equation, which is equivalent to Penman-Monteith with surface resistance set equal to zero.

2.2.1 Potential Evapotranspiration

In this study, potential evapotranspiration is calculated using the well known Penman-Monteith equation (Monteith, 1981)

$$ET_p = \frac{\Delta(R_n - G) + \rho_a c_p (e_s - e_a) / r_a}{\lambda \rho_w \left[\Delta + \gamma \left(1 + \frac{r_s}{r_a} \right) \right]} \quad (2-1)$$

where ET_p is the evapotranspiration rate (m day^{-1}); R_n is the net radiation ($\text{MJ m}^{-2} \text{ day}^{-1}$); G is the soil heat flux ($\text{MJ m}^{-2} \text{ day}^{-1}$); λ is latent heat of vaporization (MJ Kg^{-1}); ρ_a is the air density (Kg m^{-3}); c_p is the heat capacity of moist air ($\text{MJ Kg}^{-1} \text{ C}^{\circ-1}$); e_s is the saturated vapor pressure (kPa); e_a is the actual vapor pressure (kPa); r_a is the aerodynamic resistance (s m^{-1}); r_s is the surface resistance (s m^{-1}); Δ is the slope of the saturation vapor pressure curve (mb K^{-1}); and γ is the psychrometric constant ($\text{kPa C}^{\circ-1}$).

The calculations of R_n , G , r_a , r_s , e_s , and Δ in Equation 2-1 were discussed by Allen et al. (1998) in detail.

2.2.2 Potential Evaporation from Crop-Covered Soil and Transpiration from Crop

In this study, potential evaporation rate from a crop-covered soil is considered to be a function of LAI

$$E_p = ET_p e^{-\alpha LAI} \quad (2-2)$$

In the Equation 2-2, α is a plant dependent parameter, generally takes a value of 0.4.

Drooger (1999) used a lumped value of 0.45 for mixed crops of grape, cotton and olive trees; Childs et al. (1977) used a value of 0.438 for corn; Feddes et al. (1976) used a value of 0.39 for red cabbage.

The difference between the potential ET and maximum evaporation is the maximum possible transpiration rate from crop.

$$T_p = ET_p - E_p \quad (2-3)$$

2.2.3 Potential Evaporation from Bare Saturated Soil

The evaporation from wet bare soil can be calculated by mixed combination of evaporation from the rate of net radiation and the evaporation rate computed from aerodynamic methods (Chow et al., 1988).

$$E = \frac{\Delta}{\Delta + \gamma} E_r + \frac{\gamma}{\Delta + \gamma} E_a \quad (2-4)$$

where Δ , γ have the same meaning as above; E_r is the evaporation rate computed from the rate of net radiation (mm/day) and E_a is the evaporation rate computed from aerodynamic methods (mm/day).

E_r is calculated by the following formula,

$$E_r = \frac{\Delta(R_n - G)}{\lambda \rho_w} \quad (2-5)$$

E_a is calculated by the following formula,

$$E_a = \frac{0.622k^2 \rho_a u_2}{p \rho_w [\ln(z_2 / z_0)]^2} (e_s - e_a) \quad (2-6)$$

where z_2 is the height at which wind speed and air temperature are measured (m); z_0 is the roughness height of surface (m); p is the air pressure (KPa); k is the von Karman constant, usually taken as 0.4 and u_2 is the wind speed (m/day).

2.3 Actual Evaporation and Transpiration

2.3.1 Actual Evaporation

The approach selected to calculate actual evaporation from soils for this study was proposed by Lappala et al. (1987) in the VS2DT model.

$$E_a = \begin{cases} K_s K_r(h) \times SRES \times (h_{top} - HA) & E_a < E_p \\ E_p & E_a \geq E_p \end{cases} \quad (2-7)$$

where E_a is the actual soil evaporation ($L T^{-1}$); E_p is the potential soil evaporation ($L T^{-1}$); K_s is the saturated hydraulic conductivity ($L T^{-1}$); K_r is the relative hydraulic conductivity (-); SRES is the surface resistance (T); HA is the pressure potential at soil-atmosphere interface (L); h_{top} is the pressure potential at the first node on the land surface (L).

Pressure potential HA is calculated by the Kelvin equation (Lappala et al., 1987)

$$HA = \frac{RT}{M_w g} \ln(R_h) \quad (2-8)$$

where R is the ideal gas constant ($ML^2T^{-2}K^{-1}Mol^{-1}$); T is the absolute temperature ($^{\circ}K$); M_w is the mass of water ($M Mol^{-1}$); R_h is the relative humidity (-).

Surface resistance SRES is calculated

$$SRES = [2.0 / DZ_{top}] \times K_c / K_{s,top} \quad (2-9)$$

where $K_{s,top}$ is the saturated hydraulic conductivity of first cell from the ground surface ($L T^{-1}$); DZ_{top} is the thickness of first top cell (L); K_c is the saturated hydraulic conductivity of crust material ($L T^{-1}$).

2.3.2 Actual Transpiration

In the model developed for this study, transpiration from plants is calculated by either of two approaches, the first one is taken from the VS2DT model (Lappala et al. 1987). The second approach is widely used by other existing models such as Feddes et al. (1978), Perrochet (1987), Wu et al. (1999) and Lai and Katul (2000). The possible actual transpiration obtained by either approach is compared with the potential transpiration, and the smaller of the two is taken to be the actual transpiration.

The first approach computes transpiration based on the following plant-root extraction equation

$$q_m = K_s K_r(h) r(z, t) (h_{root} - h) \quad (2-10)$$

where $r(z, t)$ is the root activity function of depth and time ($L L^{-3}$); and h_{root} is the pressure head in the root for the entire system (L), which is usually set equal to the permanent wilting point for the plants. For most agricultural crops, the permanent wilting point is equal to about -150 m of water. Root activity is defined as the length of roots in a given volume of soil divided by that volume. Root activities range from 0 up to about 3.0 cm^{-2} , depending on the plant species and its development stage (Lappala et al., 1987). The user gives the maximum root activity at land surface and the bottom of the root zone, then a linear interpolation gives the root activity for each depth within the root zone.

In the second approach, transpiration is taken as a sink which consists of three parts (Feddes et al., 1978; Perrochet, 1987; Wu et al., 1999; Lai and Katul, 2000): (1) the potential transpiration rate T_p ; (2) a root distribution function $g(z)$ specific to different species of plants; and (3) the soil moisture dependent reduction factor $\alpha(\psi)$.

$$S(\psi, z) = \alpha(\psi) g(z) T_p \quad (2-11)$$

where $\alpha(\psi)$ is the soil moisture reduction factor (-); z is the current root depth (L); $g(z)$ is the root density distribution function (L^{-1}); and T_p is the potential transpiration rate ($L T^{-1}$).

In the Equation 2-11, $\alpha(\psi)$ and $g(z)$ must satisfy the following constraints (Lai and Katul, 2000):

(i) the integration of the product of $\alpha(\psi)$ and $g(z)$ along the root zone is no greater than 1

$$\int_0^{L_r} \alpha(\psi) g(z) dz \leq 1 \quad (2-12)$$

(ii) the integration of root distribution along the root zone is no greater than 1.

$$\int_0^{L_r} g(z) dz \leq 1 \quad (2-13)$$

(iii) soil moisture reduction factor at any point is no greater than 1.

$$\alpha(\psi) \leq 1 \quad (2-14)$$

The actual transpiration rate is evaluated from the water extraction rate by:

$$T_a(t) = \int_0^{L_r} S(z, t) dz \quad (2-15)$$

where L_r is the total root depth (L)

Determining root distribution is important in modeling the uptake of water by plant roots. The greatest concentration of roots generally occurs in the surface soil (Kalisz et al., 1987), where organic carbon content and cation exchange capacity are higher and soil bulk density is lower (Sainju and Good, 1993). Also, the shape of the root system is a function of plant species, meteorological and geographic conditions. To obtain the cumulative distribution of roots usually a nonlinear relationship between the root fraction and the soil depth is used.

When soil moisture is greater than or equal to that at field capacity, the plants are considered to transpire at potential rate. When soil moisture falls below a critical value, which usually is taken as the moisture content at field capacity, the water extraction by roots will be reduced. When the soil moisture content falls below wilting point, water can't be extracted from soils by plant roots any longer and transpiration goes to zero. The soil moisture reduction factor is used to mimic this process.

Alternative formulations for root density function and the soil moisture reduction function are given in appendix B.

CHAPTER 3 OVERLAND FLOW MODEL

3.1 Introduction

Overland flow is a dynamic part of watershed response to rainfall when the soil's infiltration capacity has been exceeded (Tisdale et al., 1998) or the water table is at or near the land surface. It is important to many engineering applications including the study of soil erosion and conservation, infiltration processes, flood prediction, surface irrigation and contaminant transport (Singh and Bhallamudi, 1998; Gandolfi and Savi, 2000).

3.1.1 Three Models for Simulating Overland Flow

The movement of surface water can be described by continuity and momentum equations applied to an incompressible fluid in form of the Saint Venant equations. In general, three models are used to simulate overland flow, 1) the kinematic wave model, 2) diffusion model, and 3) fully dynamic model.

Both kinematic wave and diffusion models have many applications in the real world. The kinematic wave approximation is applicable for steep and smooth surfaces (Lighthill and Whitham, 1955; Henderson and Wooding, 1964; Brakensiek, 1967; Woolhiser, 1969; Eagleson, 1970; Li et al., 1975; Borah et al. 1980; Govindaraju et al., 1992), while the diffusion wave approximation is also applicable for rough surfaces (Xanthopoulos and Koutitas, 1976; Ponce et al., 1978; Akan and Yen, 1981; Hromadka and Lai, 1985). However the kinematic wave approximation has limits. Since the kinematic wave model lacks the pressure term, it is not suited for overland flow over mild slopes, where diffusion plays a major role. Govindaraju et al. (1992) gave two main

criticisms of the kinematic wave approximation. The first is its inability to incorporate backwater effects. The second is its lack of any physical attenuation of the wave profile since all the energy dissipation terms of the momentum equation are neglected.

Like the kinematic wave approximation, in the diffusion wave approximation the inertia terms are also neglected. However, the pressure term is kept, which makes the diffusion wave approximation applicable in a wider range of situations. Ahn et al. (1993) argued that such simplification introduces errors between 5% and 10%, which are negligible in real world applications considering the uncertainty that affects geometrical and hydrological measurements. According to Lal (1998a), most dynamic models introduce numerical errors and instabilities when the cell size is small and the topographic data show relatively large variations over these short cell lengths (Tan, 1992).

Areas such as south Florida are characterized by large areal extent, small slopes, widespread ponding, and slow regional flow dynamics. Kinematic wave models are inadequate for these cases because backwater effects are neglected. Compared with dynamic models, diffusion flow models offer computational advantages for areas such as south Florida. Diffusion flow models have been successfully used to simulate hydrologic processes in the Everglades, using the natural system model (NSM) and the south Florida water management model (SFWMM) developed by the South Florida Water Management District (Lal, 1998a).

3.1.2 Numerical Methods in Solving Overland Flow Problems

The commonly used methods for solving overland flow problems include methods of characteristics (MOC), the finite difference method (FDM) and the finite element method (FEM).

The MOC has found many applications in shallow water flow problems (Liggett and Woolhiser, 1976; Borah et al. 1980; Hunt, 1987). The reasons lie both in its simplicity and that it has several advantages over other methods. First, the method of characteristics is well suited for sharp front problems arising from the kinematic wave equations. Second, the characteristic method may be the most accurate method for approximating boundary conditions (Liggett and Woolhiser, 1976). However, the MOC is too complicated to be used in a two-dimensional model, especially with spatially varying hillslope features (Zhang and Cundy, 1989). The common occurrence of irregular domains with spatially varying properties has led to the routine application of Eulerian methods for solution of kinematic wave problems (Munoz-Carpena et al., 1993).

Finite difference methods are among the most widely used methods for solving shallow water flow (Smith and Woolhiser, 1971; Freeze, 1972; Katopodes and Strelkoff, 1978; Holden et al., 1995). Chow and Ben-Zvi (1973) modeled overland flow by using a two-dimensional hydrodynamic equation solved by the Lax-Wendroff Scheme. Using the same scheme, Iwasa and Inoue (1982) modeled flood flows due to dam/dike breaks using the two-dimensional Saint Venant equation. Melone et al. (1988) used this scheme to simulate the dynamics of overland flow using the non-linear kinematic wave approximation. Zhang and Cundy (1989) used a MacCormack finite-difference scheme to solve a two-dimensional overland flow model. Using a higher order MacCormack scheme, Garcia and Kahawita (1986) solved the St. Venant equations.

The NSM and the SFWMM models developed by the SFWMD use a modified version of the alternating direction explicit (ADE) method to solve 2-D diffusion flow. Lal (1998a) examined three finite-difference algorithms based on the explicit method, the

alternating direct implicit (ADI) method and the successive over relaxation (SOR) method. He concluded that the ADE method has a relatively short run time and may be appropriate when high accuracy is not a priority. Explicit methods require a longer run time, but they are more accurate. SOR methods can be efficient under certain conditions due to the use of the adaptive relaxation parameter.

While finite difference methods are easy to implement, they lack the flexibility to handle problems with irregular domains. On the other hand, irregular domain problems can be easily handled by finite element methods. It is also simple to incorporate natural boundary conditions using the finite element method. This is the reason that finite element methods are adopted in many overland or shallow water flow models (Taylor et al., 1974; Ross et al., 1979; Kawahara and Yokoyama, 1980; Borah et al., 1988; Vieux et al 1990; Goodrich et al., 1991; Motha and Wigham, 1995; Gottard and Venutelli, 1997).

The Galerkin finite element method is only globally conservative, so the controlled volume finite element (CVFE) method or finite volume method, which are locally conservative, are sometimes used in overland flow or shallow water flow modeling (Zhao et al., 1994; Giammarco et al., 1996; Gottardi and Venutelli, 1997). Lal (1998b) developed a weighted implicit finite-volume model to simulate two-dimensional diffusion flow in arbitrarily shaped areas. A mixture of unstructured triangles and quadrilaterals was adopted to discretize the domain. Giammarco et al. (1996) proposed a control volume finite element (CVFE) method to model a two-dimensional overland flow problem. Gottardi and Venutelli (1997) presented a finite element program for the two-dimensional diffusion model. Control-volume finite element and Galerkin finite element (GFE) formulation were compared on the basis of the global mass-balance.

To overcome numerical oscillations in these types of problems, Rice and Schnipke (1985) developed a streamline upwind finite element method for convection-dominated flows. Tisdale et al. (1998) used a streamline upwind finite element method to solve the two-dimensional kinematic wave and shallow water wave equation for overland flow problems. Advances in Petrov-Galerkin finite element methods have resulted in reduction in such errors compared to conventional Eulerian formulation for advection-dominated transport problems. Munoz-Carpena et al. (1993) developed a Petrov-Galerkin (PG) finite element method to solve the kinematic wave formulation of the overland flow equations.

3.2 Governing Equations

3.2.1 Saint Venant Equations

The equations describing overland flow are the well-known Saint Venant equations (Abbott, 1979), which include the continuity Equation 3-1 and momentum Equations 3-2 and 3-3.

$$\frac{\partial h}{\partial t} + \frac{\partial(uh)}{\partial x} + \frac{\partial(vh)}{\partial y} = Q \quad (3.1)$$

$$\frac{\partial(uh)}{\partial t} + \frac{\partial(u^2h)}{\partial x} + \frac{\partial(uvh)}{\partial y} + gh\frac{\partial h}{\partial x} - gh(S_{0x} - S_{fx}) = 0 \quad (3.2)$$

$$\frac{\partial(vh)}{\partial t} + \frac{\partial(v^2h)}{\partial y} + \frac{\partial(uvh)}{\partial x} + gh\frac{\partial h}{\partial y} - gh(S_{0y} - S_{fy}) = 0 \quad (3.3)$$

| Local | Convective acceleration | Pressure | Gravity | Friction |
|--------------|-------------------------|----------|---------|----------------|
| acceleration | term | force | force | force |
| term | | term | term | term |
| | | | <----- | kinematic wave |
| | | <----- | | diffusion wave |
| | | <----- | | dynamic wave |

where $\psi(x,y,t)$ is the water surface elevation above a horizontal datum $= h(x,y,t) + z(x,y)$, (L); $h(x,y,t)$ is the local water depth above the surface elevation (L); $z(x,y)$ is the surface elevation, (L); t is the time (T); x,y are the horizontal Cartesian coordinates (L); $u(x,y,t)$, $v(x,y,t)$ are the flow velocities in x and y directions (L/T); $Q(x,y,t)$ is the distributed input, which is the net amount considering sources (+) such as rainfall, irrigation and sinks (-) such as evapotranspiration and infiltration (L/T); S_{0x} , S_{0y} are the bed slope in the x and y directions (-); $S_{fx}(x,y,t)$, $S_{fy}(x,y,t)$ are the friction slope in x and y directions (-); g is the gravitational acceleration (L/T²).

The full momentum equations, which include inertial terms (local acceleration terms and convective acceleration terms), pressure force terms, gravity force terms and friction force terms, are seldom used in solving overland problems. Simplification of the Saint Venant equations is appropriate for many problems (Munoz-Carpena et al., 1993). Two such simplifications are the kinematic wave and diffusion wave approximations.

3.2.2 Kinematic Wave Equation

For a kinematic wave, the inertial and the pressure terms in the momentum equation are neglected and the wave motion is described principally by the equation of continuity (Chow et al., 1988).

$$\frac{\partial h}{\partial t} + \frac{\partial(uh)}{\partial x} + \frac{\partial(vh)}{\partial y} = Q \quad (3-4)$$

$$S_{0x} = S_{fx} \quad (3-5)$$

$$S_{0y} = S_{fy} \quad (3-6)$$

Applying the Manning-Stricker law to the description of the friction slopes (Giammarco et al., 1996), we have,

$$S_{fx} = \frac{n_x^2}{h^{4/3}} |\mathbf{w}| \mathbf{w} \cdot \mathbf{i} = \frac{n_x^2}{h^{4/3}} (u^2 + v^2)^{1/2} u \quad (3-7)$$

$$S_{fy} = \frac{n_y^2}{h^{4/3}} |\mathbf{w}| \mathbf{w} \cdot \mathbf{j} = \frac{n_y^2}{h^{4/3}} (u^2 + v^2)^{1/2} v \quad (3-8)$$

where $\mathbf{w} = u\mathbf{i} + v\mathbf{j}$ is the velocity vector; and n_x, n_y are the Manning roughness coefficients in the directions x and y , respectively.

Therefore,

$$|\mathbf{w}|^2 = u^2 + v^2 = h^{4/3} \left(\frac{S_{fx}^2}{n_x^4} + \frac{S_{fy}^2}{n_y^4} \right)^{1/2} \quad (3-9)$$

Using Equations 3-5, 3-6 and 3-9 to solve for the components of the velocity vector gives:

$$u = S_{0x} \frac{h^{2/3}}{n_x^2} \left[\frac{S_{0x}^2}{n_x^4} + \frac{S_{0y}^2}{n_y^4} \right]^{-1/4} \quad (3-10)$$

$$v = S_{0y} \frac{h^{2/3}}{n_y^2} \left[\frac{S_{0x}^2}{n_x^4} + \frac{S_{0y}^2}{n_y^4} \right]^{-1/4} \quad (3-11)$$

Substituting Equations 3-10 and 3-11 into 3-4, gives the partial differential equation:

$$\frac{\partial h}{\partial t} + \frac{\partial (K_x h^{5/3})}{\partial x} + \frac{\partial (K_y h^{5/3})}{\partial y} = Q \quad (3-12)$$

where

$$K_x = \frac{S_{0x}}{n_x^2} \left[\frac{S_{0x}^2}{n_x^4} + \frac{S_{0y}^2}{n_y^4} \right]^{-1/4} \quad (3-13)$$

$$K_y = \frac{S_{0y}}{n_y^2} \left[\frac{S_{0x}^2}{n_x^4} + \frac{S_{0y}^2}{n_y^4} \right]^{-1/4} \quad (3-14)$$

3.2.3 Diffusion Wave Equation

For a diffusion wave model the inertia term in the momentum equations are neglected but the pressure terms remain, so the wave motion is described principally by the following continuity and momentum equations (Chow et al., 1988).

$$\frac{\partial h}{\partial t} + \frac{\partial(uh)}{\partial x} + \frac{\partial(vh)}{\partial y} = Q \quad (3-15)$$

$$S_{fx} = S_{ax} - \frac{\partial \psi}{\partial x} \quad (3-16)$$

$$S_{fy} = S_{ay} - \frac{\partial \psi}{\partial y} \quad (3-17)$$

Following the same procedures as above, we can get the expressions for the components of the velocity vector

$$u = -\frac{\partial \Psi}{\partial x} \frac{h^{2/3}}{n_x^2} \left[\left(\frac{\partial \Psi}{\partial x} \right)^2 \frac{1}{n_x^4} + \left(\frac{\partial \Psi}{\partial y} \right)^2 \frac{1}{n_y^4} \right]^{-1/4} \quad (3-18)$$

$$v = -\frac{\partial \Psi}{\partial y} \frac{h^{2/3}}{n_y^2} \left[\left(\frac{\partial \Psi}{\partial x} \right)^2 \frac{1}{n_x^4} + \left(\frac{\partial \Psi}{\partial y} \right)^2 \frac{1}{n_y^4} \right]^{-1/4} \quad (3-19)$$

Noticing that $\partial h / \partial t = \partial \Psi / \partial t$ and substituting Equations 3-18 and 3-19 into Equation 3-4 leads to the following partial differential equations

$$\frac{\partial \psi}{\partial t} + \frac{\partial}{\partial x} \left(-K_x \frac{\partial \psi}{\partial x} \right) + \frac{\partial}{\partial y} \left(-K_y \frac{\partial \psi}{\partial y} \right) = Q \quad (3-20)$$

where K_x and K_y are overland flow transmissivity in the x and y direction (L^2/T), which are represented as

$$K_x = \frac{h^{5/3}}{n_x^2} \left[\left(\frac{\partial \psi}{\partial x} \right)^2 \frac{1}{n_x^4} + \left(\frac{\partial \psi}{\partial y} \right)^2 \frac{1}{n_y^4} \right]^{-1/4} \quad (3-21)$$

$$K_y = \frac{h^{5/3}}{n_y^2} \left[\left(\frac{\partial \psi}{\partial x} \right)^2 \frac{1}{n_x^4} + \left(\frac{\partial \psi}{\partial y} \right)^2 \frac{1}{n_y^4} \right]^{-1/4} \quad (3-22)$$

3.3 Numerical Model Development

In this work the diffusion wave approximation was chosen to represent the overland flow process and traditional Galerkin finite element methods were used to solve these equations.

For simplicity, Equation 3-20 for the diffusion wave equation can be rewritten as:

$$\frac{\partial \psi}{\partial t} + \frac{\partial}{\partial x_i} \left[-K_i(\psi) \frac{\partial \psi}{\partial x_i} \right] - Q = 0 \quad (3-23)$$

where $\psi(\mathbf{x}, t)$ is the water surface elevation above an horizontal datum (L); i is the index for x_1 and x_2 coordinates ($i=1,2$); $K_i(\psi)$ is the a generalized form of $K_x(\psi)$ and $K_y(\psi)$; S_{0i} is the bed slope in the x and y directions (—).

The Neumann and Dirichlet boundary conditions can be written as

$$\begin{aligned} \psi(\mathbf{x}, t) &= g_D(\mathbf{x}, t) & \mathbf{x} \in \Gamma_D \\ q(\mathbf{x}, t) &= g_N(\mathbf{x}, t) & \mathbf{x} \in \Gamma_N \end{aligned} \quad (3-24)$$

In Equation 3-23, the ψ and K_{ij} can be represented by trial functions of the form

$$\psi(\mathbf{x}, t) = N_J(\mathbf{x}) \psi_J(t),$$

$$K_{ij}(\mathbf{x}, t) = N_J(\mathbf{x}) K_{ij,J}(t),$$

Using trial functions for test functions and applying Green's theorem to Equation 3-23 results in,

$$\begin{aligned} \int_{\Omega} N_I N_J \frac{d\psi_J}{dt} d\Omega + \int_{\Omega} \left[K_I \frac{\partial N_I}{\partial x_i} \frac{\partial N_J}{\partial x_i} \psi_J \right] d\Omega - \int_{\partial\Omega} N_I K_I \frac{\partial \psi_J}{\partial x_i} n_i d\Gamma \\ - \int_{\Omega} N_I Q d\Omega = 0 \end{aligned} \quad (3-25)$$

where Ω is the solution domain with boundary $\Gamma = \Gamma_D \cup \Gamma_N$ and $\Gamma_D \cap \Gamma_N = \emptyset$, $i, j=1, 2$ and $I, J=1, 2, 3$.

Writing Equation 3-24 in matrix form,

$$[A]\left\{\frac{d\Psi}{dt}\right\} + [B]\{\Psi\} = \{F\} \quad (3-26)$$

where matrices A, B and F can be calculate as

$$\begin{aligned} A_{IJ} &= \sum_e \int_{\Omega^e} N_I N_J d\Omega, \\ B_{IJ} &= \sum_e \int_{\Omega^e} K_i \frac{\partial N_I}{\partial x_i} \frac{\partial N_J}{\partial x_i} d\Omega, \\ F_I &= \sum_e \left(\int_{\partial\Omega} N_I K_i \frac{\partial \Psi}{\partial x_i} n_i d\Gamma + \int_{\Omega^e} N_I Q d\Omega \right) \end{aligned} \quad (3-27)$$

In this model we used triangular elements with linear interpolation functions for the whole domain Ω . Consider the typical triangular element with nodes numbered in the counterclockwise direction, as shown in Fig. 3-1. The trial function can be expressed as:

$$N_I = \frac{1}{2\Delta}(\alpha_I + \beta_I x + \gamma_I y) \quad I=1, 2, 3$$

where Δ is the area of triangular element; x, y are the coordinates.

Δ and α, β, γ are expressed as

$$\begin{aligned} \alpha_1 &= x_2 y_3 - x_3 y_2, & \beta_1 &= y_2 - y_3, & \gamma_1 &= x_3 - x_2, \\ \alpha_2 &= x_3 y_1 - x_1 y_3, & \beta_2 &= y_3 - y_1, & \gamma_2 &= x_1 - x_3, \\ \alpha_3 &= x_1 y_2 - x_2 y_1, & \beta_3 &= y_1 - y_2, & \gamma_3 &= x_2 - x_1, \end{aligned}$$

The area of triangular element is

$$\Delta = \frac{1}{2} \begin{vmatrix} 1 & x_1 & y_1 \\ 1 & x_2 & y_2 \\ 1 & x_3 & y_3 \end{vmatrix}$$

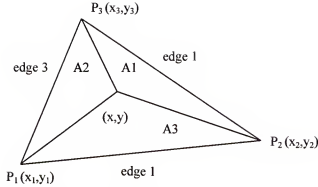


Figure 3-1. Area coordinates and node designation for triangles.

Substituting trial functions into Equation 3-27, after some manipulations (Appendix C) we get expressions for Matrices A, B and F.

$$A^e = \frac{\Delta^e}{12} \begin{vmatrix} 2 & 1 & 1 \\ 1 & 2 & 1 \\ 1 & 1 & 2 \end{vmatrix} \quad (3-28)$$

$$B_U^e = \frac{1}{4\Delta^e} (\bar{k}_x \beta_I \beta_J + \bar{k}_y \gamma_I \gamma_J) \quad I, J=1, 2, 3 \quad (3-29)$$

where $\bar{k}_x = (k_{x,1} + k_{x,2} + k_{x,3}) / 3$ and $\bar{k}_y = (k_{y,1} + k_{y,2} + k_{y,3}) / 3$

F_I^e consists of two parts. In the first part, $\partial\Omega$ is the entire boundary of the flow region. However, nodes that are on boundary portion Γ_D are to be replaced by the appropriate Dirichlet (specified head) boundary conditions introduced by modifying the global matrix. In the second part only nodes that are on boundary Γ_N are considered. We note that

$$q = -K_t(\Psi) \frac{\partial \Psi}{\partial x_i}$$

Then the first part of F_I^e is $-\int_{\partial\Omega} N_I q d\Gamma$, its integration is

$$F_1^e = - \begin{pmatrix} (2q_1 + q_2)L/6 \\ (q_1 + 2q_2)L/6 \\ 0 \end{pmatrix} \quad (3-30)$$

where q_1 and q_2 are flux at nodes 1 and 2 of an edge prescribed as flux boundary.

The third part of F_f^e is relatively easy to integrate,

$$F_{f3}^e = \frac{\Delta Q}{3} \quad (3-31)$$

3.4. Initial and Boundary Conditions

A set of differential equations cannot be solved unless appropriate boundary conditions are specified. In certain cases, boundary conditions can lead to instability, i.e. uncontrolled, non-physical evolution of the solution. The initial condition for overland flows is usually one of a dry land surface. However this initial condition leads to singularities for the full St. Venant equations and therefore researchers frequently assume a very thin flow depth at the start of simulation (Govindaraju et al., 1992; Tisdale et al., 1998).

Before prescribing boundary conditions, it is often useful to know the Froude number of the overland flow. The Froude number is defined as the ratio of inertial force to gravitational force. In mathematical form,

$$Fr = \frac{u}{\sqrt{gh}}$$

If the magnitude of the flow velocity is such that $|u| \leq \sqrt{gh}$ or $-1 \leq Fr \leq 1$, the waves can propagate in all directions, and the flow is called subcritical (tranquil flow, streaming flow, low flow regime). In the opposite case, the wave can propagate only in

some certain directions, and the flow is called supercritical (jet flow, rapid flow, shooting flow, upper flow regime).

Zhang and Cundy (1989) considered two kinds of boundary conditions in their problems, closed boundary and open boundary. At a closed boundary both the normal and tangential velocities vanish because of the no-penetration and no-slip condition. The water depth at this boundary fluctuates depending on the flow inside the boundary. For an open boundary, if flow immediately upslope from the boundary is subcritical, critical flow may be defined at the boundary $h_c = \left((q_x^2 + q_y^2) / g \right)^{1/3}$, where h_c is the critical depth of the flow. Akan and Yen (1981) suggested that the outflow boundary conditions may be prescribed as a discharge or stage hydrograph or a discharge-stage relationship. Govindaraju et al. (1992) adopted a critical flow downstream condition that simulates a free fall situation, i.e. for the full St. Venant equations, at the downstream boundary $u = \sqrt{gh}$. For the diffusion wave approximation, this critical flow downstream boundary can be further simplified using velocity expressions in water depth such as Equations 3-18 and 3-19.

3.5 Verification of the Overland Flow Model

3.5.1 Example Problem 1

In this example, flow over a plane surface was simulated. The results were compared against experimental data obtained by Izzard and Augustine (1943) and simulated results by Tisdale et al. (1998) using a streamline upwind finite element method (Figures 3-2 and 3-3). The plane was 72 ft long and 6 ft wide. It was coated with a mixture of emulsified asphalt and sand and had an approximate texture of sheet-asphalt pavement. In the first simulation, a rainfall intensity of 3.87 in/hr was applied for a period

of 650 s. The second simulation used an initial rainfall intensity of 3.69 in/hr for a period of 600 s, immediately followed by an intensity of 1.93 in/hr for 350 s.

The finite element mesh used to represent the plane consisted of 50 nodes and 80 elements. A surface slope of 0.001 and a Manning's coefficient of 0.01 were used for the two test simulations.

For both tests, the simulated results by this study are very close to the simulated results obtained by Tisdale et al. (1998) using the upstream upwind finite element method. The numerical results also generally agree well with the experimental data. For the numerical models, runoff starts from the time when rainfall begins because surface detention is not considered. Also the numerical model does not consider the raindrop impact on discharge and thus failed to reproduce the sudden increases in discharge resulting from the release or reduction of overpressure head due to raindrop impact when rainfall stopped or the rainfall intensity changed.

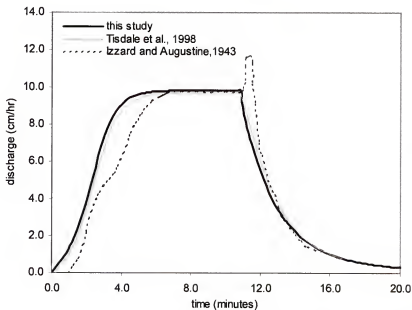


Figure 3-2. Discharge hydrographs for flow off single plane with rainfall rate of 9.83 cm/h and rainfall duration of 650 s.

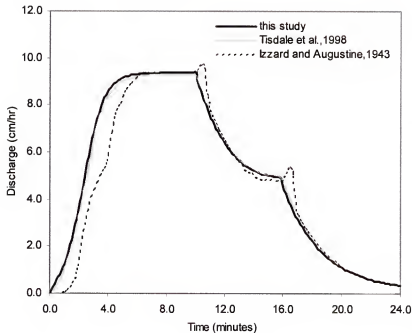


Figure 3-3. Discharge hydrographs for flow off single plane with rainfall rates of 9.37 and 4.90 cm/h and rainfall durations of 600 and 350 s.

3.5.2 Example Problem 2

In this example, the model was run against the experimental data obtained by Iwagaki (1955). The experiment was conducted in a laboratory flume, which was made of very smooth aluminum. The flume was divided into three sections of equal length. Each section of flume was 8 m long and surface slopes were 0.02, 0.015 and 0.01 from upslope to downslope. During the experiments, three different rainfall intensities of 389, 230 and 288 cm/hour were simultaneously applied to the upper, middle, and lower sections respectively. Rainfall lasted for 10, 20 and 30 seconds respectively for three different experiments.

Borah et al. (1980) simulated this problem using a kinematic wave shock-fitting model. Zhang and Cundy (1989) simulated this problem using a hydrodynamic model with a MacCormack finite difference scheme. Tisdale et al. (1998) simulated this

problem using a kinematic wave model with a streamline upwind finite element method. Their results or experimental data are referenced for comparison.

The finite element mesh used in this study to represent the runoff surface consisted of 221 nodes and 384 elements. The calibrated Manning's coefficient for the test simulation was 0.009, which is between the value of 0.0107 used by Tisdale et al. (1998) and the value of 0.006 calibrated by Zhang and Cundy (1989).

Hydrographs for each experiment from different approaches are shown in Figures 3-4 through 3-6. Like other models, the simulated results from our model show good agreement with experimental data, especially for the hydrographs resulting from 20 s and 30 s rainfall (Figures 3-5 and 3-6).

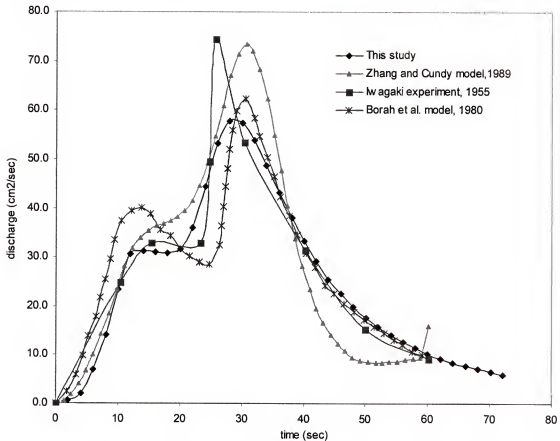


Figure 3-4. Comparison of hydrographs on a three-plane cascade by different methods ($t_r = 10$ sec).

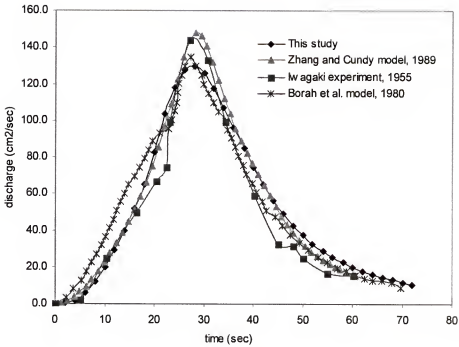


Figure 3-5. Comparison of hydrographs on a three-plane cascade by different methods (tr=20 sec).

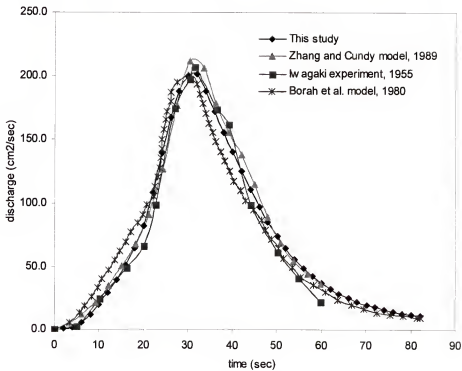


Figure 3-6. Comparison of hydrographs on a three-plane cascade by different methods (tr=30 sec).

3.6 Conclusions

In this chapter, two examples were presented to verify the overland flow model. In the first example, the model was tested against experimental data obtained by Izzard and Augustine (1943) and simulated results by Tisdale et al. (1998) using a streamline upwind finite element method. The simulated results agree reasonably well with experimental data. Simulated runoff started at the time when rainfall started, while experiment indicated that runoff did not start until 50 seconds after rainfall started. Several reasons may cause the discrepancy. The simulated model considered neither surface retention (water retained on the ground surface in micro-depressions) nor surface detention (water temporarily detained on the surface before runoff occurs). Both factors delay the time when runoff begins. The model did not consider rainfall resistance effects on surface runoff so it failed to reproduce the abrupt increase in runoff rate when rainfall ceased or rainfall intensity changed.

In the second example, the model was tested against the experimental data. Instead of single plane, in this experiment, the flume consisted of three planes with different slopes. Like other numerical models, the model developed in this study gave results similar to experimental data especially for rainfall events with longer duration. Based on the performance of the model in the previous two examples, we are confident in the reliability and accuracy of the overland flow model.

CHAPTER 4 INTEGRATING ATMOSPHERIC AND OVERLAND FLOW COMPONENTS WITH VADOSE ZONE FLOW COMPONENT

4.1. Introduction

Numerical simulation of transient water flow in soil in the presence of plants has been undertaken by various authors such as Molz and Remson (1970), Nimah and Hanks(1973), Lappala et al. (1987) and Rowse et al. (1978). In most of those models, water uptake by plant roots is represented by a volumetric sink term, which is incorporated into the continuity equation for soil water flow. The sink term in these models requires detailed information about the root system as functions of root density, root distribution and root length. Experimental evaluation of such functions is both time-consuming and costly. For this reason simpler and more practical sink terms have been proposed. A detailed description of different functions was given in Chapter 2. For both bare soil and soil in the presence of plants, the evaporation rate is incorporated as a top boundary condition for the system equations for solving soil water flow problems.

Many hydraulic and hydrological problems involve the interaction of flow on the soil surface and in the subsurface media. Numerical modeling of such problems involves connecting the surface and subsurface components. There exist three different approaches to couple these components. The simplest and least accurate approach is the externally coupled approach. In this approach, the surface flow and subsurface flow are simulated separately in succession without iteration. A simple infiltration rate expression is typically used as the common boundary condition between two components.

The second approach to join the surface and subsurface flow components together is an alternating iterative approach. In this approach, the surface flow and subsurface flow are solved separately but iteratively at the same time step joined by the common internal boundary of infiltration between the two components. Solutions for surface and subsurface flows at a time step are achieved when the iterative errors are within specified acceptable tolerances before advancing to the next time step. The third approach of conjunctive modeling is a coupled model in which the surface flow equation, subsurface flow equation, and common internal boundary condition of an infiltration equation are all solved as simultaneous equations at each time step before advancing to the next time step. Numerically, the first approach is the simplest, whereas the third approach is the most sophisticated and theoretically the most satisfactory approach. Until now, the third approach has not been found in the literature.

Smith and Woolhiser (1971) were the first to publish results on the first approach of coupled surface and subsurface flow simulation. They used the Lax-Wendroff second-order explicit scheme to solve the one-dimensional kinematic wave overland flow and the nonlinear Crank-Nicholson implicit scheme to solve the one-dimensional vertical unsaturated flow. Motha and Whigham (1995) used this approach to integrate the one-dimensional kinematic wave overland flow component and the two-dimensional transient saturated-unsaturated flow component. Their studies were based on the Galerkin's formulation of finite element method. A simplified variation of this externally coupled approach is to express infiltration as an algebraic equation. For example, Katopodes and Strelkoff (1977) and Playan et al. (1994) used the Kostiakov infiltration equation. Munoz-Carpena et al. (1993), Stone et al. (1992), Savabi (1993) and Tayfur et al. (1993)

used the Green-Ampt infiltration formula. Cundy and Tento (1985) used the Philip infiltration formula. Smith and Hebbert (1979), Woolhiser et al. (1990) and Woolhiser et al. (1996) used the Smith-Parlange infiltration equation. Singh and Bhallamudi (1996) allowed a choice of the Kostiakov equation or the quasi-analytical Parlange equation for the infiltration calculation.

At the present, the second approach may be the most common way to couple surface and subsurface flow components. Pinder and Sauer (1971) were the first to report on such an approach. They used a staggered explicit scheme to solve the one-dimensional channel flow conjunctively with an alternating direction implicit (ADI) method for the two-dimensional saturated groundwater. Freeze (1972) formulated a conjunctive model using the Lax-Wendroff explicit scheme to solve the one-dimensional channel flow dynamic wave and a successive line over-relaxation technique to solve the three-dimensional unsaturated subsurface flow. Akan and Yen (1981) developed a coupled alternating iterative conjunctive model for one-dimensional subsurface flow. A four-point implicit finite-difference scheme was employed for the solution of the surface runoff equation and an implicit finite difference scheme based on the successive line over-relaxation method (SLOR) was employed for the solution of subsurface flow equation. Sakkas et al. (1994) proposed a model that coupled the one-dimensional shallow water equations and the two-dimensional Richards' equations. The explicit, two-step, predictor-corrector MacCormack scheme was used to solve both the surface flow and subsurface flow. Wallach et al. (1997) coupled the one-dimensional kinematic overland flow with the two-dimensional subsurface flow to study the errors in surface runoff prediction by neglecting the relationship between infiltration rate and overland flow depth. Govindaraju

et al. (1988) used the diffusion wave approximation for the surface flow component. The surface flow equation was solved by the centered implicit scheme, while the two-dimensional Richards' equation was solved by the SLOR technique. Singh and Bhallamudi (1998) coupled a one-dimensional surface flow model with the two-dimensional Richards' equation. The surface flow was solved by an explicit finite difference scheme. The two-dimensional Richards' equation in the mixed form for the subsurface flow was solved using a strongly implicit finite-difference scheme.

Morita and Yen (2000) coupled the two-dimensional surface flow and three-dimensional subsurface flow components using the iterative approach. Numerical schemes of the purely explicit method, alternating direction explicit (ADE) methods, and alternating direction implicit (ADI) methods were investigated for application to the surface and subsurface flow sub-models in terms of accuracy, stability, and calculation time. Gandolfi and Savi (2000) developed a model based on the two-dimensional shallow water equations and coupled with the one-dimensional Richards' equation. The second order explicit finite difference MacCormack scheme was used to solve the surface and subsurface flow.

4.2. Integrating Model Components

In the model developed for this study, evaporation from the soil surface is taken as the top boundary condition for subsurface flow components. Actual evaporation from the ponded surface is considered to equal the potential evaporation rate. When the moisture content in the soil surface decreases to the residual point, the boundary condition changes from specified flux to specified head, which is the soil potential at the residual. Transpiration from plants is represented by a volumetric sink term in the

subsurface continuity flow equation. The potential and actual evaporation and transpiration rates are estimated using the techniques covered in Chapter 2.

Surface and subsurface flow components are interrelated by a common pressure head and the infiltration at the ground surface. The top boundary condition for the subsurface flow is determined by the surface flow depth. The infiltration term in the surface flow equation is controlled by the subsurface flow conditions. In the model developed for this study, the following procedure is adopted for simulating the interaction between the surface and the subsurface flow components for each time step.

When the soil potential becomes positive at the top nodes, a zero soil potential is specified for the calculation of the infiltration rate, which is less than the rainfall rate. The infiltration rate at the ground surfaces is determined by solving the Richards' equation using the specified head for the upper boundary, the infiltration rate calculated in solving Richards' equation is then used to solve the surface flow equation. The water depth obtained from the solution of the surface equation is used as a specified head boundary for the subsurface flow equation. The above procedures are repeated until the iterative errors for both surface and subsurface flow are within specified acceptable tolerances.

4.3 Integrated Model Examples

Four case studies are presented to illustrate the capacity of the coupled model. Case studies 1 to 3 give examples that integrate the atmospheric component with the subsurface component, while case study 4 gives an example that integrates the surface component with the subsurface component.

4.3.1 Case Study 1

The model was validated using the data from Paynes Prairie State Preserve from an experiment conducted from April 10 to July 20, 2001 (Jacobs et al., 2002). Paynes

Prairie State Preserve, a large highland marsh system in north-central Florida, USA, is 5600 ha in area and is 13 km long (east-west). The major portion of the area lies in the prairie basin. Biological communities include freshwater marshes, wet prairie and pasture. The entire basin is either seasonally or perennially flooded. The experiment was conducted in the wet prairie community within this system (29°34'14"N, 82°16'46"W). This prairie is a relatively flat, treeless plain with moderately dense ground cover. The common species in this area were *Panicum hemitomon* Schultes (maidcane), *Polygonum hydropiperoides* Michx. (mild water-pepper), and *Ptilimnium capillaceum* Michx. (mock bishop's weed). *Eupatorium capillifolium* Lam. (dog fennel) was also prevalent and *Sesbania sp.* (sesben) was scattered throughout; both species were measured to be about 1.5 m tall. Field observations showed that the majority of the root zone was contained in the upper 10-cm soil layer, with approximately 95% of the root zone contained in the upper 25-cm soil layer. Based on the plant characteristics and model calibration, in this model we assign a root depth and leaf area index (LAI) of 25 cm and 2.7 respectively. The α value for Equation 2-2 was assumed to be 0.4. The root density distribution function given in Equation C-6 was used with $c=0.5$.

The micrometeorological measurements necessary to determine atmospheric forcing were obtained using instruments mounted approximately 4.0 m above the ground surface. Measurements were made every minute and averaged over 30-minute intervals except where noted. The net radiation was measured with a net radiometer (Radiation Energy Balance Systems Q7.1). The temperature and relative humidity were measured using a shielded Vaisala model HMP 45C sensor (Vaisala, Inc.). Wind speed and direction were measured with an CS 800-L anemometer (RM Young, Inc.). Atmospheric

pressure was measured with a PTB100 barometer (Vaisala, Inc.). Precipitation was measured using a TE525 tipping bucket rain gage (Texas Electronics). Ground heat flux was measured by RFT 3.1 heat fluxes plates installed approximately 2 cm below the surface (Radiation Energy Balance Systems). Actual evapotranspiration was measured using the eddy correlation approach. Water table depth was recorded every 15 minutes using a WL-14 Water Logger. Near-surface volumetric soil water content was recorded using a CSI 615L water-content reflectometer installed vertically to average over the top 25 cm of soil (Jacobs et al., 2002).

The meteorological data were used to calculate daily potential ET. The missing meteorological data from April 18 to 30 were obtained from the Citra Weather Station (29°24'35"N, 82°10'13"W) located in the Florida Automated Weather Network (FAWN). The Penman-Monteith surface resistances were assumed to be 200 s m⁻¹ for April and 100 s m⁻¹ for May, June and July. Those values agree well with resistance coefficients reported from different wetlands, including 75-150 s m⁻¹ for a prairie wetland in Nebraska, USA; 25 s m⁻¹ during the growing season and 90 s m⁻¹ for the remainder of the year for cattails in the South Florida Everglades (Jacobs et al., 2002).

Table 4-1. Soil characteristics for the Wauberg sand soil in the Paynes Prairie Preserve Area, Florida used in case study 1

| Layer | Depth(cm) | Soil Texture | Saturated Hydraulic Conductivity (cm hr ⁻¹) | Saturated Moisture Content | Residual Moisture Content |
|---------|-----------|--------------|---------------------------------------------------------|----------------------------|---------------------------|
| Layer 1 | 1-10 | Sand | 248.5 | 0.38 | 0.03 |
| Layer 2 | 10-28 | Sand | 85 | 0.45 | 0.03 |
| Layer 3 | 28-140 | Sand loam | 0.05 | 0.30 | 0.03 |
| Layer 4 | 140-160 | Sand loam | 0.01 | 0.30 | 0.14 |

The site's soils include Emerald fine sandy loam, Wauberg sand, and Ledwith Muck. The predominant soil type was Wauberg sand (Jacobs et al., 2002). The modeled soil characteristics were based on the experimental data by Jacobs et al. (2002), the soil data for Wauberg soil from UF-IFAS (1985). Four layers were identified (Table 4-1). The soil moisture release curves for the first layer and fourth layer were fitted to the van Genuchten $\theta(\psi)$ relationship using the experimental data by Jacobs et al. (2002) and UF-IFAS (1985), respectively. The second and third layers were best characterized by the Haverkamp $K(\psi)$ and $\theta(\psi)$ relationships. The soil release curves for the second and third layers were fit to the experimental data from UF-IFAS (1985). The parameters for the $K(\psi)$ relation were calibrated since no source existed. Table 4-2 lists the soil potential relationships and fitted parameters for each of the layers.

Table 4-2. Soil potential relationships and fitted parameters for Wauberg soil layers in the Paynes Prairie Preserve Area, Florida used in case study 1

| Soil layer | Relationship | α | M | n | A | α | β | γ |
|------------|---------------|----------|------|-------|--------------------|-------------------|---------|----------|
| Layer 1 | Van Genuchten | 0.1 | 1.66 | 0.398 | N/A | N/A | N/A | N/A |
| Layer 2 | Haverkamp | N/A | N/A | N/A | 1.18×10^6 | 1.0×10^6 | 3.0 | 3.9 |
| Layer 3 | Haverkamp | N/A | N/A | N/A | 1.18×10^6 | 1.0×10^6 | 3.0 | 3.5 |
| Layer 4 | Van Genuchten | 0.015 | 1.45 | 0.31 | N/A | N/A | N/A | N/A |

The unsaturated flow model was used to simulate soil water dynamics forced with both the daily average and the diurnal cycle of potential evapotranspiration. The simulated volumetric soil moisture content in the top 25 cm, the water table depth, and the actual evapotranspiration from Days of Year (DOY) 100 to 181 of 2001 were compared to measured values. Figure 4-1 shows the measured average soil moisture and

water table values between DOY 100 and 181 and the calculated values between DOY 100 and 201. The comparison indicates that the simulated results agree with the measured data reasonably well except that the simulated water table fluctuation between DOY 161 and 181 is not as intense as the measured values. As the simulated water table agrees well with the observed values before and after this period, the observed water table's rapid rise and fall during this period may reflect soil macroproperties that resulted in locally enhanced infiltration and mounding of the groundwater table with a subsequent lateral redistribution.

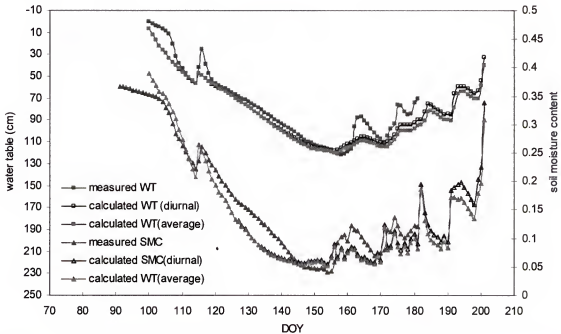


Figure 4-1. Comparison of measured and predicted water table and moisture change with time based on the study at Paynes Prairie State Preserve site.

Figure 4-2 compares the measured ET against calculated potential and actual ET. The calculated actual ET compares well with measured ET for the whole period except for period DOY 106 to 114. The model overestimated potential and actual ET for this period.

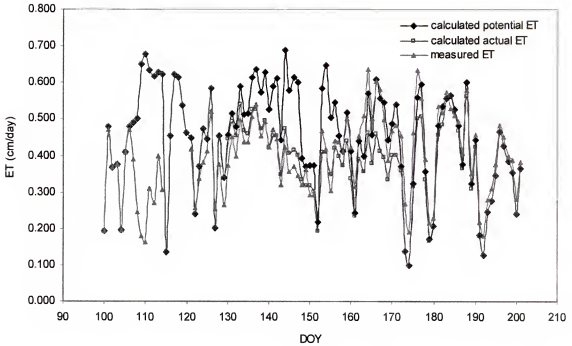


Figure 4-2. Comparison of measured and predicted evapotranspiration with time based on the study at Paynes Prairie State Preserve site.

The goodness of fit between simulated and measured data was quantified using the Nash-Sutcliffe efficiency where

$$Eff = 1 - \frac{\sum(model - measured)^2}{\sum(measured - \overline{measured})^2}.$$

The Nash-Sutcliffe efficiency results, summarized in Table 4-3, are 0.888, 0.902, and 0.605 for the simulated water table, soil moisture content and actual ET, respectively. These results demonstrate that the model satisfactorily captures the soil water dynamics and indicate that using daily average PET adequately characterizes the required atmospheric forcing.

The unsaturated flow model was next used to simulate soil water dynamics forced with the diurnal PET rate. Figure 4-2 shows that for high water table conditions, no significant evapotranspiration difference exists between the two methods. However, for

the low water table conditions that occurred for Julian days 130 through 172, the calculated actual ET results using the diurnal PET are lower than those obtained using daily average ET in the numerical simulation. This decrease in water removed from the soil impacts the water table and temporal soil water dynamics. Figure 4-2 shows that the diurnal PET results in higher water tables and wetter surface conditions that better reflect observed values than the daily average. Application of the diurnal PET results in a slight improvement to the Nash-Sutcliffe efficiencies, which were 0.916, 0.913, and 0.653 for the simulated water table, soil moisture content and actual ET, respectively (Table 4-3).

Table 4-3. Model forecast efficiency for case study 1

| Nash- Sutcliffe Forecast Efficiency | | |
|-------------------------------------|-------------------------------------|----------------------------------------|
| Parameters | Modeled Results Using Average ET | Modeled Results Using Sinusoidal ET |
| Water Table Depth | 0.888 | 0.916 |
| Average Soil Moisture Content | 0.902 | 0.913 |
| Actual ET | 0.605 | 0.653 |

Table 4-4. Soil parameters for $k(\psi)$ and $\theta(\psi)$ for case studies 2 and 3

| Soil | Sand | Yolo light Clay |
|---------------------|---------------------|---------------------|
| $K_s(\text{cm/hr})$ | 33.984 | 0.04428 |
| A | 1.175×10^6 | 1.246×10^2 |
| α | 1.611×10^6 | 7.390×10^2 |
| β | 4.747 | 1.770 |
| γ | 3.9600 | 4.0000 |
| θ_s | 0.2870 | 0.4950 |
| θ_r | 0.0750 | 0.1240 |

Note: Data are taken from Gottardy and Venutelli (1993).

4.3.2 Case Study 2

For this study, the influence of the diurnal PE function on the prediction of actual evaporation and water dynamics was further explored for a bare sandy soil and a range of water table depths. A homogeneous soil column consisting of a sandy soil was considered. Its $K(\psi)$ and $\theta(\psi)$ relationships were characterized using the Haverkamp equations using parameters observed by Gottardi and Venutelli (1993) as listed in Table 4-4.

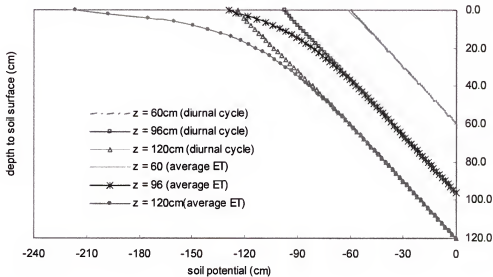


Figure 4-3. Soil potential profiles at different water tables after two days of evaporation for a bare sandy soil, both considering a diurnal cycle of evaporation and using average daily evaporation.

The soil column was uniformly divided into 60 equal elements. The daily PE rate was 4.00 mm day^{-1} , roughly equal to the average daily PET for case study 1. The initial soil potential is -10 cm for every node except the bottom boundary, where soil potential was zero. The model was run to equilibrium before the atmospheric forcings were applied. To study the influence of water table on the actual evaporation process, the bare

soil model was run three times with the water table at depths of 60, 96 and 120 cm, while holding all other parameters the same.

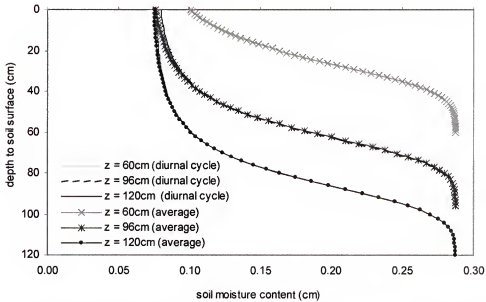


Figure 4-4. Soil moisture content profiles at different water tables after two days of evaporation for a bare sandy soil, both considering a diurnal cycle of evaporation and using average daily evaporation.

Figure 4-3 gives a comparison of the soil potential profile after two days of evaporation from a bare sandy soil, both considering a diurnal cycle of evaporation and using average daily evaporation. From Figure 4-3, it is apparent that as the depth to the water table increases, the difference between the soil potential profiles from using diurnal cycle and daily average of evaporation increases. For a water table at a depth of 96 cm, the soil moisture profiles from the two approaches begins to diverge from a location of 30 cm below the soil surface to a maximum difference of 32 cm tension at the soil surface. For the water table at 120 cm, the soil moisture profile begins to diverge at 40 cm and the tension difference between the approaches is 92.6 cm at the soil surface. For a water table at depth 60 cm, the soil potential profiles from both approaches are very similar.

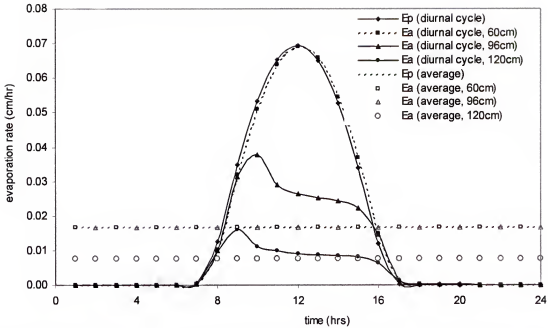


Figure 4-5. Actual evaporation during the 24-hour period of second day at different water tables from a bare sandy soil, both considering a diurnal cycle of evaporation and using average daily evaporation.

Figure 4-4 shows a comparison of soil moisture content profiles resulting from the same simulations outlined above. When water table depth is 60 cm, the soil moisture profiles from the two approaches are very similar. When the water table depth increases to 96 cm, the soil moisture profiles from the two approaches begin to diverge at a point 38 cm below the soil surface with a maximum difference of 0.003 at the soil surface. When water table depth increases to 120 cm, the soil moisture profiles from the two approaches begin to diverge at a point 30 cm below the soil surface with a maximum difference of 0.0016 at the soil surface. It is interesting that when water table depth increases from 96 to 120 cm, the difference between the soil moisture profiles decreases. The reason may be that the difference between the actual evaporation rates from both approaches is greater when water table is 96 cm than when water table is 120 cm,

possibly because the potential evaporation cannot be satisfied when water table depth is further increased, even using the average daily approach.

Figure 4-5 shows a comparison of potential evaporation and actual evaporation rate for a 24-hour period beginning after 1 day of evaporation. The potential evaporation rate can be satisfied for the whole period using the average potential evaporation rate when water table depth is 60 cm or 96 cm. However when water table depth is increased to 120 cm, the potential evaporation rate cannot be satisfied. For the diurnal cycle approach, when water table depth is 60 cm, potential evaporation rate can be satisfied for the whole period. However, when water table depth is increased to 96 cm or 120 cm it is apparent that the potential evaporation cannot be satisfied during peak potential evaporation because of the decreasing soil potential and hydraulic conductivity near the soil surface. Thus, using the average daily potential evaporation rate removes an excess of water from the soil profile.

4.3.3 Case Study 3

In this case study, a clay soil was used to examine the effects of plants on actual evapotranspiration and soil water dynamics. As for case study 2, the Haverkamp $K(\psi)$ and $\theta(\psi)$ relationships were used to characterize the clay soil. The parameters for the relationship are listed in Table 4-4. The water table was 96 cm from the soil surface. The soil column was uniformly divided into 60 elements. The daily average evapotranspiration rate was again taken to be 4.0 mm day^{-1} . The initial soil potential was -10 cm for every node except the bottom boundary, where soil potential is zero. The model was run to equilibrium before atmospheric forcing was applied. In this case study, the model was run for a bare clay soil and for the clay soil in presence of plants. The same parameters used in case study 1 were selected to characterize plants.

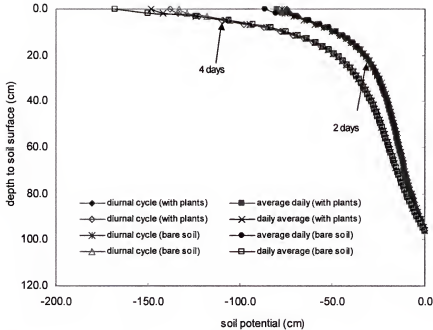


Figure 4-6. Soil potential profiles after 2 and 4 days of evaporation for a bare clay soil and a clay soil in presence of plants, both considering a diurnal cycle of evaporation and using average daily evaporation.

Figure 4-6 gives a comparison of the soil potential profile after 2 and 4 days considering both a diurnal cycle of potential evaporation and average daily potential evaporation for bare clay soil and the clay soil in presence of plant. The soil potential profiles using a diurnal cycle of potential evaporation and daily average potential evaporation are identical for depth greater than 5 cm. Due to the higher moisture holding capacity of the clay, the actual evaporation is closer to the potential evaporation than for the sand. For a bare soil with a water table depth of 96 cm the maximum soil potential differences at the soil surface after 2 and 4 days are 9.25 and 34.4 cm respectively, slightly lower than those observed for sand. This is a result of the relatively slow redistribution of soil water to the upper layers of the soil profile for the clay soil, which impacts the evaporation rate.

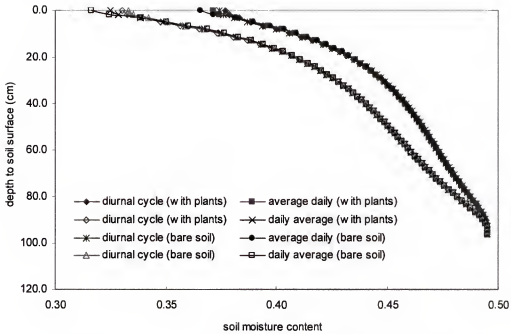


Figure 4-7. Soil moisture profiles after 2 and 4 days of evaporation for a bare clay soil and a clay soil in presence of plants, both considering a diurnal cycle of evaporation and using average daily evaporation.

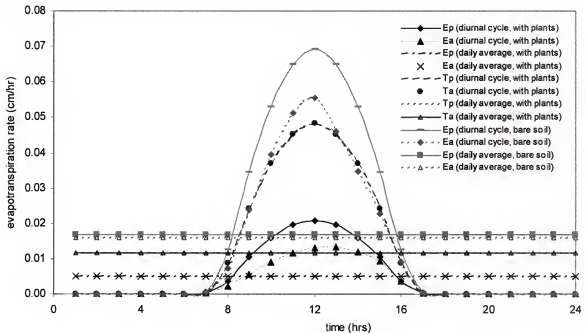


Figure 4-8. Actual evaporation during the 24-hour period of fourth day from a bare sandy soil and a soil in presence of plants, both considering a diurnal cycle of evaporation and using average daily evaporation.

All parameters for the scenario assuming plants are present were the same as for case study 1. In Figure 4-6 the soil potential profiles after 2 and 4 days of evapotranspiration are shown. For the case in presence of plants, the maximum soil potential differences at the soil surface after evapotranspiration for 2 and 4 days are 5.88 and 10.5 cm respectively. The differences are smaller than for the pure evaporation process for bare soil, apparently because more water is lost from the deeper soil when soil is covered with plants. Figure 4-7 shows the soil moisture profiles after 3 and 4 days of evapotranspiration. For the case in presence of plants, the difference between soil moisture contents at the ground surface by the end of 4th day obtained using the average and diurnal cycle evapotranspiration is 0.0054, compared to 0.017 for bare soil. This phenomenon is consistent with soil potential change for both cases.

Figure 4-8 compares the potential and actual evaporation rate for a clay soil for a 24-hour period during the fourth day. In contrast to case study 2, the potential evaporation rate cannot be satisfied even when average potential evaporation is used in the simulation. As with case study 2, less water is removed from the soil profile when accounting for the higher daytime evaporative demand using the diurnal potential evaporation cycle.

4.3.4 Case Study 4

For this case study, the data from the experiment conducted by Smith and Woolhiser (1971) for a coupled surface-subsurface flow are used to verify the model. The experimental data have been used by several authors (Akan and Yen, 1981; Singh and Bhallamudi, 1998) for the comparison with their numerical models. The experiment was conducted in a laboratory watershed consisting of a soil flume and a rainfall simulator. The soil was Poudre fine sand. The flume was 2 in. (51mm) in width, 4 ft (1.22 m) in

depth, and 40 ft (12.2 m) in length. The slope of the flume was 0.01. The bottom of the flume was impervious, but water was collected at ends for measurement. Three layers were identified with thickness of 76.5, 229.5 and 761 mm respectively. The fluid used was a light oil with a kinematic viscosity of 0.003 sq in./sec ($1.94 \times 10^{-4} \text{ m}^2/\text{s}$). A rainfall simulator generated a rainfall with intensity of 9.9 in/h (250 mm/h) over a duration of 15 min. The dry initial condition existed after the flume had drained for several weeks and the water table was approximately 1066.8 mm. In this study, the model was run to equilibrium and the soil moisture profile at equilibrium was used as the initial condition for modeling. The $K(\psi)$ and $\theta(\psi)$ relationships were determined experimentally. The relative hydraulic conductivity, K_r and saturated moisture content, θ_r are defined as

$$K_r = \frac{K}{K_s} \quad (4-1)$$

$$S_e = \frac{\theta - \theta_r}{\theta_s - \theta_r} \quad (4-2)$$

in which θ_r is the residual moisture content, K_s and θ_s are the saturated hydraulic conductivity and saturated moisture content respectively, K and θ are the hydraulic conductivity and moisture content. The curves for S_e vs. pressure head and K_r vs. pressure head used by Smith and Woolhiser (1971) were fitted by Singh and Bhallamudi (1998). The fitted expressions are employed in this example with small modification so they are a little closer to measured data. They are written here for reference.

For layer 1:

$$S_e = \begin{cases} \left(\frac{\Psi_b}{\Psi} \right)^{\lambda} & \text{if } \psi \leq -12.85 \text{ cm} \\ 0.8434 - 0.0148\psi - 0.0026\psi^2 & \text{if } -12.85 \leq \psi \leq -2.82 \text{ cm} \\ 0.8645 & \text{if } \psi > -2.82 \text{ cm} \end{cases} \quad (4-3)$$

$$K_r = \begin{cases} \left(\frac{\Psi_b}{\Psi}\right)^\eta & \text{if } \psi \leq -13.729 \text{ cm} \\ 0.5228 + 0.0204\psi - 0.0009\psi^2 & \text{if } -13.729 \leq \psi \leq -1.0 \text{ cm} \\ 0.5015 & \text{if } \psi > -1.0 \text{ cm} \end{cases} \quad (4-4)$$

For layer 2:

$$S_e = \begin{cases} \left(\frac{\Psi_b}{\Psi}\right)^\lambda & \text{if } \psi \leq -17.196 \text{ cm} \\ 0.9163 + 0.0011\psi - 0.0012\psi^2 & \text{if } -17.196 \leq \psi \leq -2.0 \text{ cm} \\ 0.9093 & \text{if } \psi > -2.0 \text{ cm} \end{cases} \quad (4-5)$$

$$K_r = \begin{cases} \left(\frac{\Psi_b}{\Psi}\right)^\eta & \text{if } \psi \leq -17 \text{ cm} \\ 0.6421 + 0.0226\psi - 0.00042\psi^2 & \text{if } -17 \leq \psi \leq -1.0 \text{ cm} \\ 0.6189 & \text{if } \psi > -1.0 \text{ cm} \end{cases} \quad (4-6)$$

For layer 3:

$$S_e = \begin{cases} \left(\frac{\Psi_b}{\Psi}\right)^\lambda & \text{if } \psi \leq -25.18 \text{ cm} \\ 0.9842 + 0.01\psi - 0.000536\psi^2 & \text{if } -25.18 \leq \psi \leq -2.0 \text{ cm} \\ 0.962 & \text{if } \psi > -2.0 \text{ cm} \end{cases} \quad (4-7)$$

$$K_r = \begin{cases} \left(\frac{\Psi_b}{\Psi}\right)^\eta & \text{if } \psi \leq -21.34 \text{ cm} \\ 0.7387 + 0.0063\psi - 0.0011\psi^2 & \text{if } -21.34 \leq \psi \leq -1.0 \text{ cm} \\ 0.7313 & \text{if } \psi > -1.0 \text{ cm} \end{cases} \quad (4-8)$$

The values of K_s , θ_s , θ_r , λ , η and ψ_b for the three soil layers are given in Table 4-5.

Table 4-5. Hydraulic properties of the soil

| Layer | K_s (cm/day) | θ_s | θ_r | λ | η | ψ_b (cm) |
|-------|----------------|------------|------------|-----------|--------|---------------|
| 1 | 566.9 | 0.460 | 0.020 | 2.03 | 8.09 | -10.0 |
| 2 | 365.7 | 0.504 | 0.025 | 2.20 | 8.60 | -13.0 |
| 3 | 268.2 | 0.543 | 0.025 | 2.31 | 8.93 | -17.0 |

The horizontal plane for overland flow is divided into 48 triangle elements and 32 nodes (Figure 4-9). The area close to downstream was more densely discretized compared to the area close to upper stream. Each element is the top boundary of a 1-D soil column with 25 nodes. The distance between the water table and the land surface of the downstream end was 1066.8 mm.

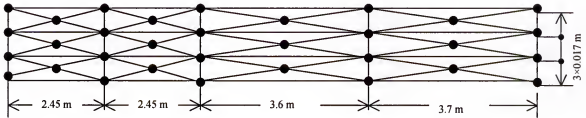


Figure 4-9. Overland flow domain discretization.

Figure 4-10 shows the runoff hydrograph at the downstream for the experiment results by Smith and Woolhiser (1971), the numerical results by Akan and Yen (1981) and Singh and Bhallamudi (1998) and this study. The first half of the rising limb of the hydrograph is close to that of Smith and Woolhiser (1971), the other half of the rising limb of the hydrograph is closer to that of Singh and Bhallamudi (1998), while the recession limb of the hydrograph is closer to that of Akan and Yen (1981). Our results show a slight improvement over the hydrograph presented by Singh and Bhallamudi (1998). The discrepancy between the present numerical results and the numerical results by Akan and Yen (1981) may be due to the different overland flow models that were used to simulate surface runoff and also the minor differences in processing the soil-moisture characteristic curves. Akan and Yen (1981) used a dynamic wave model for their overland flow while we used a diffusion overland flow model. Finally, the different

algorithms used in solving the differential equations and the way by which the study domain was discretized may introduce discrepancy in the results.

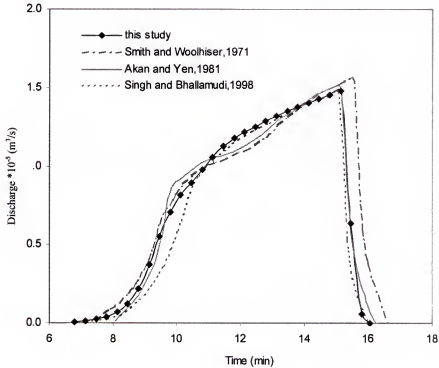


Figure 4-10. Comparison of runoff hydrograph at the downstream from the experiment results by Smith and Woolhiser (1971), the numerical models by Akan and Yen (1981) and Singh and Bhallamudi (1998), and model developed in this study.

4.4. Concluding Remarks

In case study 1, an example based on an experiment conducted at Paynes Prairie State Preserve site was simulated to study how water table and soil moisture are influenced by the atmospheric forcings. From this study it is shown that the model can simulate actual evapotranspiration, water table and moisture content reasonably well, both when daily average ET or diurnal cycle ET are used to force the model. However using the diurnal cycle of ET showed a slight improvement on the prediction accuracy.

Give the same initial moisture condition and evapotranspiration rate, the soil potential all through the soil profile for a sandy soil (case study 2) is relatively higher than that for a clay soil (case study 3), because of differences in water transport capacity. Our tests show that for a sandy soil the actual evapotranspiration is mainly restricted by the residual potential of the soil. However, for the clay soil in a drying process, the actual evaporation rate is mainly determined by upper ward flux driven by the pressure-potential gradient between the soil and the atmosphere, expressed in Equation 2-7, an algorithm used in the VS2DT model for calculating actual evaporation, rather than the residual potential of the soil. At the soil surface, the soil potential difference between cases when the daily average and diurnal cycle is used is greater for sandy soil than that for clay soil. Due to the different soil moisture holding capacities of sand and clay, the soil moisture potential profiles using daily average and diurnal cycle begin to diverge at a location of 30 cm below the soil surface for sandy soil, while for clay soil, divergence occurs only 5 cm below the soil surface.

For different water table depths, the actual evaporation rate may be quite different even for the same atmospheric forcing. In case study 2, as water table depth increases, the actual evaporation rate significantly decreases. Comparing the actual evaporation pattern of the bare soil and soil in presence of plants, we find that with the same potential evapotranspiration rate, soils in the presence of plants evaporate water at a rate very close to the potential evaporation rate because the roots draw moisture from a larger volume than for surface evaporation from bare soil.

In case study 4, the proposed coupled surface-subsurface flow model is used to simulate an experiment conducted by results by Smith and Woolhiser (1971). The

numerical results obtained from running the model developed in this study were compared with both the experimental data and the numerical results by Akan and Yen (1981) and Singh and Bhallamudi (1998). The numerical results from the model developed in this study are close to those by Singh and Bhallamudi (1998). Generally speaking, the agreement between the observed and computed hydrographs is reasonably good.

CHAPTER 5

MONTE CARLO SIMULATION OF COUPLED OVERLAND AND VADOSE ZONE FLOW

5.1. Introduction

Natural watersheds exhibit spatial heterogeneity in topography, surface roughness, vegetation, and soil infiltration capacity. The influence of the spatial variability of these parameters on surface runoff, soil erosion and pollutant transport has been widely recognized in hydrology. To examine the relationship between the surface flow processes and soil and vegetation characteristics, it is very important to develop a physically-based multidimensional model that incorporates spatial variations in topography, surface roughness and soil infiltration capacity.

Over the past several decades, the influence of spatial variations in topography, surface roughness and soil infiltration characteristics on the variability in surface runoff has been studied by a number of researchers. Using a Monte Carlo methodology and the Smith and Parlange infiltration model, Smith and Hebbert (1979) examined the effects of random distribution of infiltration characteristics on the hydrologic performance of catchment areas. They found that the mean ponding time in a composite simulation showed little bias, while the mean infiltration rate was particularly biased at greater coefficients of variation and smaller ratios of rainfall intensity to saturated hydraulic conductivity.

Freeze (1980) used a stochastic-conceptual hydrologic model to investigate the influence of spatial stochastic properties of hillslope parameters on the statistical

properties of runoff events. Both Hortonian and Dunnian overland flow generation mechanisms were simulated. The results ranked the importance of the stochastic properties of the distribution of hydraulic conductivity as follows: the mean value, the standard deviation and the autocorrelation function. Freeze warned that great error may be introduced in the statistics of predicted runoff when an equivalent uniform hillslope is used in lieu of a heterogeneous hillslope, for a sequence of stochastically generated storm events.

Utilizing a parallel plane analogy to incorporate lognormal spatial variability of saturated hydraulic conductivity, Woolhiser and Goodrich (1988) studied the influence of spatial variations of saturated hydraulic conductivity on the surface runoff for different intensities of storm events. They found that a uniform plane represented by the geometric mean of hydraulic conductivity yielded higher peak discharges for low infiltration rates or high intensity storms, while storms of short duration and high saturated hydraulic conductivity values led to a higher discharge from the heterogeneous hillslope.

Zhang and Cundy (1989) developed a two-dimensional hydrodynamic and numerical model for overland flow and applied the model to study the effects of spatially varied roughness, infiltration and microtopography on the variability of surface runoff for a single random replicate. Their study shows that microtopography is the dominant factor causing spatial variation in overland flow depth, velocity and direction. As only one realization of each spatially varied parameter was used, their results are more qualitative than quantitative.

Julien and Moglen (1990) examined the spatially uncorrelated variability in slope, roughness, width and excess rainfall on a one-dimensional runoff plane separately. The

kinematic wave approximation of the St. Venant equations was selected and solved using a one-dimensional finite element method. After analyzing results from 8400 simulated dimensionless hydrographs under spatially varied input, they concluded that variability in discharge from impervious surfaces depends primarily on the ratio of rainfall duration to the time to equilibrium. Runoff variability from uncorrelated and correlated slope, Manning's n , width, and excess rainfall intensity, decreased in a similar manner with increasing rainfall duration. Among four spatially varied parameters, excess rainfall demonstrated the greatest relative sensitivity effect on surface runoff, while slope had the least effect.

Using a Monte Carlo methodology and a two-dimensional hydrodynamic rainfall-runoff model, CASC2D, coupled with the Green-Ampt equation, Saghaian et al. (1995) examined the variability in Hortonian surface runoff discharge and volume produced by stationary rainstorms on watersheds with spatially distributed soil saturated hydraulic conductivity. Their study revealed the importance of the ratio of the mean saturated hydraulic conductivity to the uniform rainfall, and rainfall duration to the representative equilibrium time of the mean system. In general, the variability in both discharge and runoff volume for randomly distributed systems increased with the coefficient of variation of K and the ratio of saturated hydraulic conductivity to rainfall intensity, compared to the runoff generated from uniformly distributed systems. Runoff variability was found to decrease when time increased unless the mean value of hydraulic conductivity approached the rainfall intensity. The spatial variability of hydraulic conductivity exerted a greater influence on the runoff volume than on the peak discharge. Increasing initial soil moisture contents, particularly near saturated conditions, generally

caused more diversity in the hydrograph response of heterogeneous watersheds excited by short-duration storms, but had a minimal effect under long duration storms.

Employing the kinematic wave equations with interactive Smith-Parlange infiltration, Woolhiser et al. (1996) studied the effects of spatial variability of saturated hydraulic conductivity on Hortonian overland flow. They found that runoff hydrographs were strongly affected by trends in hydraulic conductivity, particularly for small runoff events. Their study showed that the flow concentration in rills and the resulting reduced effective wetted areas subject to infiltration after rainfall ceases had a major impact on runoff peaks and time to peak for cases where the saturated hydraulic conductivity increased downslope.

By studying the interaction between infiltration and the Hortonian runoff using a kinematic wave model and the Monte Carlo methodology, Corradini et al. (1998) concluded that for realistic values of the coefficient of variation of the saturated hydraulic conductivity, the run-on process could not be disregarded. It produced a significant decrease of overland flow during both the rising and the recession limb of the hydrograph. Merz and Plate (1997) investigated the effects of spatial variability of infiltration parameters and initial soil moisture on the rainfall runoff process using a quasi-three-dimensional, process-oriented model---SAKE / FGM and a single replicate approach. They found that effects of spatial variability are small for very small and for large runoff events.

Using the Monte-Carlo methodology together with the fully distributed hydrological model r.water.fea (Vieux and Gaur, 1994), which simulates storm water runoff using a kinematic wave model coupled with the Green-Ampt infiltration equation,

Seguis et al. (2002) investigated the impact of stochastic and elevation-related spatial distributions of soil parameters on Hortonian runoff. They found that regardless of the saturated hydraulic conductivity gradient and/or stochastic variation coefficient, outflow volumes and peak discharges tended towards those calculated with a uniform saturated hydraulic conductivity value when the storm was long and intense. They also found that whatever the rainstorm and variation coefficient of saturated hydraulic conductivity, the basin runoff production was higher when the saturated hydraulic conductivity increased with elevation than when it decreased.

In most previous work, the spatial analysis of surface runoff has been conducted using the one-dimensional kinematic wave model coupled with a simple infiltration model such as Green-Ampt infiltration equation, Philip infiltration equation and Smith-Parlange equation (Smith and Parlange, 1978). The interaction between the surface and subsurface water flow has not been fully considered. Furthermore most previous work analyzed the effects of variability of soil characteristics on surface runoff peak and volume, but not surface water depth. Saturated hydraulic conductivity has been the main parameter varied in previous studies and usually the soil has been assumed to be homogeneous in the vertical. The objectives of this study are i) to quantify the influence of spatial variability of microtopography, Manning's n and saturated hydraulic conductivity on surface runoff characteristics, ii) to compare the relative sensitivity of different spatially varied parameters, and iii) to compare our results with those reported by previous researchers to see if discrepancies exist because of somewhat different approaches used to model the problems.

5.2 Statement of the Problem

The hypothetical hillslope is a modification of case study 4 in Chapter 4. As a geometrical simplification, we represent a natural hillslope by a single plane with a mean slope of 2%. The plane was 40 *40 m. The vertical distance from the soil surface to the fixed water table at the downstream end of the hillslope was 1.2 m. A rainfall with an intensity of 250 mm/h was applied to the hillslope uniformly for a duration of 15 min (900 sec). No-flux boundary conditions were applied to all boundaries except the downstream boundary, where a critical flow condition was employed.

A stationary lognormal distribution of saturated hydraulic conductivity was assumed and hydraulic conductivities were allowed to vary spatially in three dimensions with different correlation scales in the vertical and horizontal planes. In the horizontal plane, the correlation scale was 4 m, while in the vertical direction the correlation scale was 0.25 m. The geometric mean of saturated hydraulic conductivity was 3.657 m/day, so the ratio of saturated hydraulic conductivity to rainfall is 0.61 (<1).

The Manning's coefficients were assumed to be stationary and lognormally distributed on the soil surface. The correlation scale for Manning's coefficients was 4 m. The geometric mean of Manning's coefficient was $0.04 \text{ s/m}^{1/3}$. The microtopography was assumed to have a stationary normal distribution. The actual surface elevation was set equal to the sum of a spatially variable microtopography term and a mean surface elevation obtained using the mean slope. As with the Manning's coefficient, the correlation scale for microtopography was 4 m.

The Monte Carlo methodology was used to analyze the impact of the heterogeneities described above on surface water depth and discharge. For hydraulic conductivity, 5 cases were considered, each case corresponding to a random field with

the same geometric mean but different standard deviation. The lognormal standard deviation for each case was 0.5, 0.65, 0.8, 1.1 and 1.5 respectively. For Manning's coefficient, 5 cases with geometric mean equal to $0.04 \text{ s m}^{-1/3}$ and lognormal standard deviation of 0.5, 0.65, 0.8, 0.95 and 1.1 were considered. For surface elevation, only four cases were considered, standard deviations of microtopography corresponding to 0.2, 0.3, 0.4 and 0.5 cm around the 2% mean slope. The model had difficulty converging if the microtopography deviation was increased to above 0.5 cm because for this study the maximum average water ponding depth is about 0.5 cm. Table 5-1 summarizes the statistical properties of all parameters for the case studies described above.

Table 5-1. Statistical parameters for the case studies

| Parameters | Mean | Correlation Scale | Distribution | Standard Deviations |
|----------------------------------------------|-------|-------------------------------------|--------------|---------------------------|
| Hydraulic conductivity (m/day) | 3.657 | x-y plane: 4m z direction: 0.25m | Lognormal | 0.5, 0.65, 0.8, 1.1, 1.5 |
| Microtopography (cm) | 0 | 4m | Normal | 0.2, 0.3, 0.4, 0.5 |
| Manning's coefficient ($\text{s m}^{1/3}$) | 0.04 | 4m | Lognormal | 0.5, 0.65, 0.8, 0.95, 1.1 |

The study domain was discretized into a 40*40 cell rectangular mesh in the horizontal plane. Each rectangular cell mesh in the horizontal plane was further split into two triangular elements. According to the case study, each element was assigned the geometric mean value of parameters being treated as deterministic and randomly varying values generated using a turning bands algorithm for the parameter being treated as spatially variable (Tompson et al., 1989). Two hundred simulations were carried out for each case study. By using the Monte Carlo method, we are assuming that if a sufficiently

large number of realizations are used in the simulations, the statistical properties of the simulated output variables over the ensemble of all realizations may be determined. The 200 replicates were selected in Monte Carlo simulations so that both the reliability of results and computational time would be acceptable.

5.3 Analysis of Results

5.3.1 The Effects of Spatially Varied Hydraulic Conductivities on Subsurface Flow

Using the model developed in this study, the effects of spatial variability of hydraulic conductivity, Manning's coefficient and microtopography on surface water depth and discharge rate were examined separately and systematically. Primary emphasis was put on analyzing the variability of surface water depth and discharge rate, not the subsurface flow, which has been intensively studied by others (Foussereau et al., 2000; Russo, 1993; Russo et al., 1998) for the case in which all rainfall infiltrates the profile. However, the outputs concerning subsurface flow will be briefly reviewed. The outputs for subsurface flow include soil potential, moisture content and water flux from the soil surface to water table. Figures 5-1 to 5-6 show results for an element which is on the horizontal domain centerline between the upstream and downstream, 1.5 m away from the downstream end.

Figure 5-1 shows the soil potential profiles from the soil surface to the water table at different times using the uniform field (geometric mean = 3.657 m/day) and the mean soil potential profile from the Monte Carlo simulation (log standard deviation = 0.8). From this figure it is evident that there is little difference between the soil potentials at the soil surface at different times for the uniform field and the mean of the random fields. At time $t=300$ sec, the soil potential from the ensemble mean field is about 1.5 cm higher than that from the uniform field. At time 600 sec and 900 sec, the soil potential difference

for both cases is not significant. After rainfall ceases at 900 sec, water begins to drain from the top soil layer. At 1200 sec and 1500 sec, the soil potential difference between the uniform field and ensemble mean field are quite different, especially for the top 50 cm of soil and the soil profile from the ensemble mean field is drier. This is most likely due to the fact that for the random hydraulic conductivity field more surface runoff is generated and less water infiltrates into the unsaturated zone.

From Figure 5-2 we find that the soil water potential standard deviation is high at the soil surface near the beginning (300 sec) and at the end of the storm (1200-1500 sec). In the middle of the storm event, when water begins to pond at the soil surface, the soil water potential standard deviation at the soil surface becomes insignificant although at other soil depths the soil potential standard deviation continues to increase as the moisture front moves down. This figure indicates the soil water potential uncertainty is highest near the leading and tailing edge of the moisture profile, where soil potential gradients are high.

Figure 5-3 shows that the infiltration rate at the soil surface is higher for the uniform field than for the ensemble mean of the Monte Carlo simulation. This indicates that the total volume of surface runoff is higher for the ensemble mean random field than for the uniform case. The reason may be that the infiltration rate in each soil column is mostly determined by the lowest hydraulic conductivity. When the variability of hydraulic conductivity increases, the probability of hydraulic conductivity with extremely low values increase. The overall effect is that effective hydraulic conductivity decreases, the surface infiltration rate decreases. Figure 5-4 shows that water flux uncertainty is highest at the leading edge of the mean moisture profile.

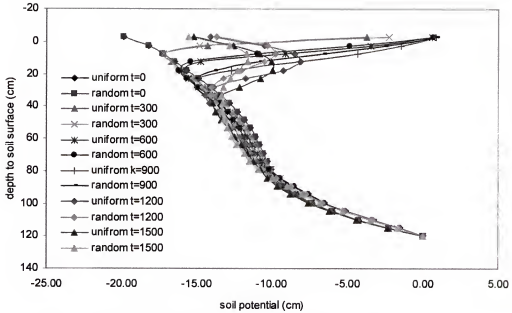


Figure 5-1. Comparison of soil potential profiles at different times for uniform geometric mean K_s and mean of Monte Carlo simulations for an element of 1.5 m from the downstream.

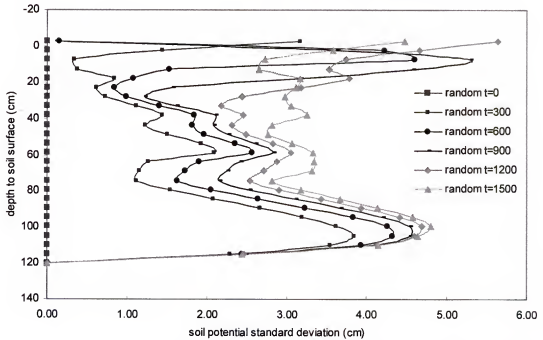


Figure 5-2. Soil potential standard deviation profiles at different times for Monte Carlo simulations for an element of 1.5 m from the downstream.

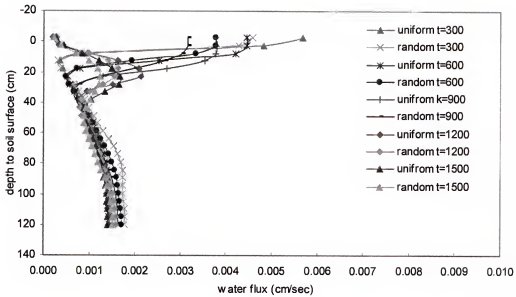


Figure 5-3. Comparison of water flux profiles at different times for uniform geometric mean K_s and mean of Monte Carlo simulations for an element of 1.5 m from the downstream.

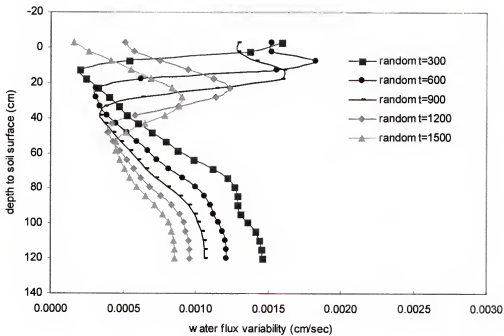


Figure 5-4. Water flux standard deviation profiles at different times for Monte Carlo simulations for an element of 1.5 m from the downstream.

5.3.2 The Effects of Spatially Varied Hydraulic Conductivities on Surface Runoff

The effects of spatially varied hydraulic conductivities on surface runoff were examined by running different Monte Carlo simulations with different standard deviations of log hydraulic conductivity. Random saturated hydraulic conductivity fields with lognormal standard deviation of 0.5, 0.65, 0.8, 1.1 and 1.5 were evaluated in this study. For each Monte Carlo simulation, 200 realizations were generated and used by the model for simulating surface and subsurface flow. From the outputs of surface water depth and total surface discharge for the 200 realizations, the mean and standard deviation of surface runoff discharge and the mean and standard deviation of water depth along the domain centerline were obtained.

The uniform and mean Monte Carlo water depth curves along the centerline between upstream and downstream at 450 sec and 900 sec are shown in Figure 5-5 and Figure 5-7 respectively. From Figure 5-5 we can see that near the middle of the storm at 450 sec, the mean water depths increase with increasing hydraulic conductivity standard deviation. The mean of the Monte Carlo simulations is not the same as the result using mean input parameters. This indicates a non-linear effect and the need to derive effective parameters to simulate the mean response. At the end of the storm (900 sec), the water depths generated from the uniform field are higher than the mean generated from the Monte Carlo simulations and the actual depths are much closer. The difference between the deterministic and mean Monte Carlo water depth prediction decreases as time increases because as time increases the infiltration rate decreases so the effect of hydraulic conductivity on the runoff process decreases.

Figure 5-6 and Figure 5-8 show that the standard deviation of water depth increases as the variability of hydraulic conductivity increases, but the increase in the

standard deviation of water depth for both downstream and upstream is much less than for the center domain. It is apparent that the upstream and downstream boundaries restrict the uncertainty of water depth prediction at both ends of the domain.

Figure 5-9 shows the hydrographs obtained using the uniform field and the mean of the Monte Carlo simulations for various hydraulic conductivity standard deviations. For the ensemble mean field, the hydrograph extends for a longer period compared with the uniform geometric mean field. This simply means that at early or later times, the mean water depths for the Monte Carlo simulation are higher than the water depths reduced from for the uniform geometric mean field. At the time corresponding to peak discharge, the mean water depths for the ensemble mean of the Monte Carlo simulation are lower than the water depths for the uniform geometric mean field. From Figure 5-9 we can see that compared to the uniform field, surface runoff begins earlier if the hydraulic conductivity is a spatial random field and, the higher the variability, the earlier runoff begins. Compared to the uniform field, surface runoff ends later for the Monte Carlo simulation mean, and again the higher the saturated hydraulic conductivity variability, the later runoff ceases. For both the rising and recession limbs, the higher the variability, the higher the discharge rate. In general, the mean surface discharge runoff for the Monte Carlo simulations is higher than that for the uniform field for the whole time period, except at around 900 sec when the rainfall stops. At 900 sec, the peak discharge rate from the uniform field is higher than any Monte Carlo simulation. However, the total surface discharge volume increases with the increase in field variability, and except for the random field with log standard deviation of 0.5, all random fields have more surface runoff than uniform field (see Table 5-2 and Figure 5-11). Figure 5-10 shows the

standard deviation of runoff discharge with time for the Monte Carlo simulations. The standard deviation of surface runoff increases with time for the first half of the storm, then begins to decrease after the inflection point of the rising limb of mean surface discharge is reached. After the rainfall ceases at 900 sec, the variability of runoff decreases rapidly as water is lost from the domain. As expected, as the variability of hydraulic conductivity increases, the variability of surface runoff increases.

Table 5-2 summarizes the surface runoff starting time, ending time, peak and total volume for the different hydraulic conductivity case studies. Figure 5-11 shows the change of mean discharge volume with the hydraulic conductivity standard deviation. From this figure, it seems an approximately linear relationship exists between the discharge volume and the log standard deviation of hydraulic conductivity.

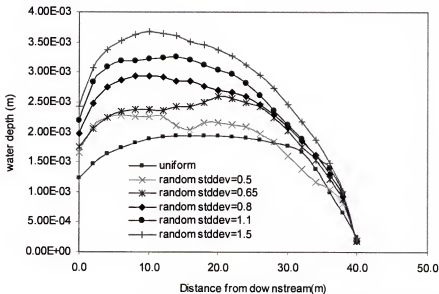


Figure 5-5. Water depth along the centerline between upstream and downstream for uniform field and Monte Carlo simulations with different saturated hydraulic conductivity standard deviation at time 450 sec.

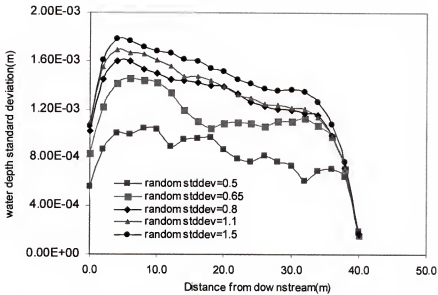


Figure 5-6. Water depth standard deviation along the centerline between upstream and downstream for Monte Carlo simulations with different saturated hydraulic conductivity standard deviation at 450 sec.

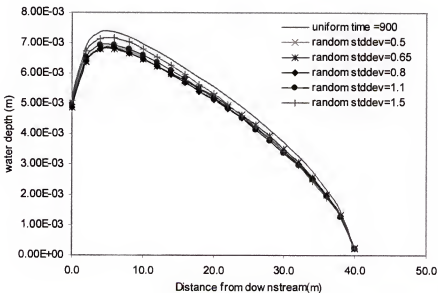


Figure 5-7. Water depth along the centerline between upstream and downstream for uniform field and Monte Carlo simulations with different saturated hydraulic conductivity standard deviation at time 900 sec.

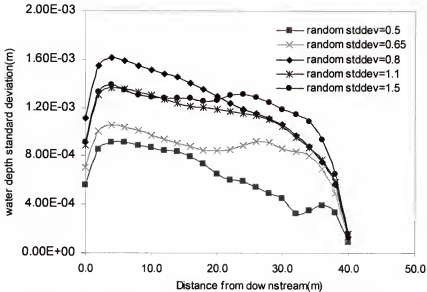


Figure 5-8. Water depth standard deviation along the centerline between upstream and downstream for Monte Carlo simulations with different saturated hydraulic conductivity standard deviation at 900 sec.

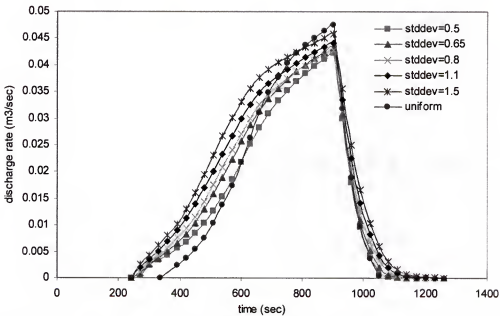


Figure 5-9. Comparison of surface runoff hydrographs for the uniform field and Monte Carlo simulations with different variability of saturated hydraulic conductivity.

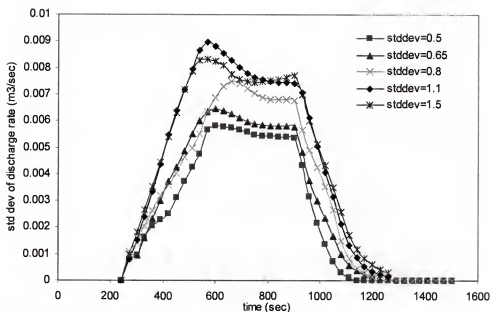


Figure 5-10. Comparison of standard deviations of discharge for Monte Carlo simulations with different variability of saturated hydraulic conductivity.

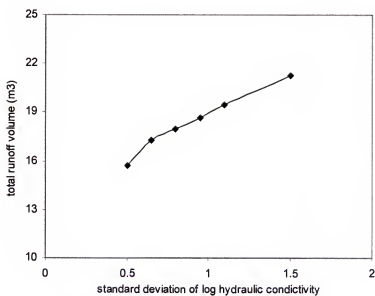


Figure 5-11. Mean discharge volume versus log standard deviation of hydraulic conductivity.

Table 5-2. Surface runoff starting time, ending time, peak and total volume for random hydraulic conductivity fields with different log standard deviation

| Log std dev Hydrograph Attributes | Uniform | 0.5 | 0.65 | 0.8 | 1.1 | 1.5 |
|-----------------------------------------|---------|--------|--------|--------|--------|--------|
| Peak (m^3/sec) | 0.0475 | 0.0422 | 0.0434 | 0.0429 | 0.0442 | 0.0458 |
| Starting time (sec) | 337.45 | 270 | 260 | 240 | 240 | 240 |
| Ending time (sec) | 1051 | 1110 | 1140 | 1200 | 1200 | 1260 |
| Total volume (m^3) | 16.30 | 15.73 | 17.27 | 17.97 | 19.47 | 21.27 |

5.3.3 The Effects of Spatially Varied Manning's Coefficients on Surface Runoff

Similar procedures to those discussed in the last section were followed to examine the effects of variability in Manning's coefficient on surface runoff. Random fields of Manning's coefficients with lognormal standard deviations of 0.5, 0.65, 0.8, 0.95 and 1.1 were evaluated in this case.

The uniform and ensemble water depth curves along the centerline between upstream and downstream at 450 sec and 900 sec are shown in Figure 5-12 and Figure 5-14 respectively. At 450 sec Figure 5-12 shows water depths generated from the Monte Carlo simulations fluctuated around the mean water depths generated from the uniform field. The fluctuation is due to lack of sufficient Monte Carlo replicates to smooth the estimate of the ensemble mean. At 900 sec, the water depths generated from the Monte Carlo simulations are higher than that generated from the uniform field. Increasing variability leads to the increasing of mean water depths at 900 sec. From Figure 5-13 and Figure 5-15, we can see that the variability of water depth increases when the variability of Manning's coefficient increases.

Figure 5-16 shows the surface runoff hydrographs obtained using the uniform field and the ensemble mean field with various standard deviation values. Compared to the uniform field, the ensemble mean surface runoff begins a little later for all levels of variability of Manning's coefficient. However, there is no significant difference among the surface runoff starting time for the random fields. Compared to the uniform Manning's coefficient, surface runoff ends later for the mean of the Monte Carlo simulations. The trend is that the higher the Manning's coefficient variability, the later runoff ends. On the rising limb, the higher the variability, the lower the discharge rate is, and the mean discharge rate on the rising limb for all the Monte Carlo simulations is lower than that from the uniform field. At 900 sec, the peak discharge rate from the uniform field is higher than the mean from any Monte Carlo simulation. On the recession limb, the mean discharge rate for each Monte Carlo simulation is very close to that for uniform field except for during the later recession period when the Monte Carlo simulations have higher mean discharge rates. This is likely due to longer travel times, i.e. increased mean surface resistance for spatially variable Manning's coefficient.

Figure 5-17 shows the change of mean discharge volume with the variability in Manning's coefficient. The total discharge volume decreases as the Manning's coefficient variability increases, and all random fields have less surface runoff than uniform field. This implies that spatial variability in the Manning's coefficient leads to more infiltration of rainfall into the subsurface. For comparison, Table 5-3 summarizes the surface runoff starting time, ending time, peak and total volume for different fields.

Figure 5-18 shows standard deviations of discharge for the Monte Carlo simulations. The standard deviation of surface runoff increases with time until midway

through the storm (i.e. at the reflection point of the rising limb of the mean hydrograph) when the runoff variability begins to decrease. After the rainfall ceases, the variability of runoff starts to increase again. Variability is maximum at the inflection point of the recession limb of the mean hydrograph and then decreases as the runoff leaves the model domain. Again with the increase in variability of Manning's coefficient, the variability of surface runoff increases.

Table 5-3. Surface runoff starting time, ending time, peak and total volume for random Manning's coefficient fields with different log standard deviation

| Log std dev Hydrograph attributes | Uniform | 0.5 | 0.65 | 0.8 | 0.95 | 1.1 |
|--------------------------------------|---------|--------|--------|--------|--------|--------|
| Peak (m^3/sec) | 0.0475 | 0.0473 | 0.0471 | 0.0468 | 0.0461 | 0.0443 |
| Starting time (sec) | 337.45 | 360 | 360 | 360 | 360 | 360 |
| Ending time (sec) | 1051 | 1110 | 1110 | 1140 | 1140 | 1200 |
| Total volume (m^3) | 16.30 | 16.04 | 15.90 | 15.55 | 15.11 | 14.09 |

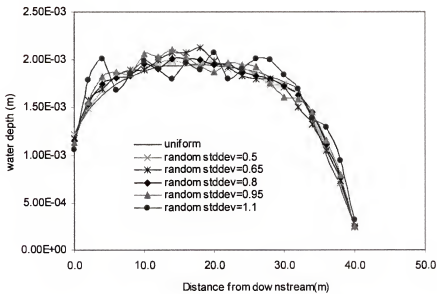


Figure 5-12. Water depth along the centerline between upstream and downstream for uniform field and Monte Carlo simulations with different standard deviation of Manning's coefficient at time 450 sec.

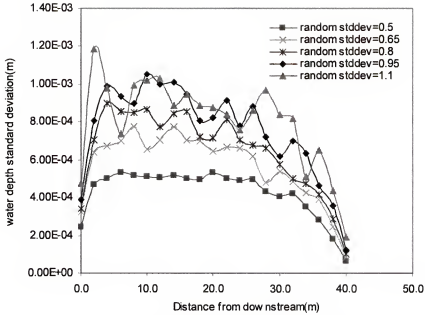


Figure 5-13. Water depth standard deviation along the centerline between upstream and downstream for Monte Carlo simulations with different standard deviation of Manning's coefficient at 450 sec.

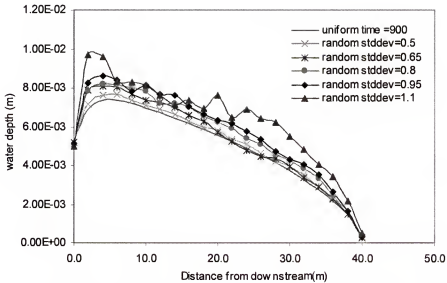


Figure 5-14. Water depth along the centerline between upstream and downstream for uniform field and Monte Carlo simulations with different standard deviation of Manning's coefficient at time 900 sec.

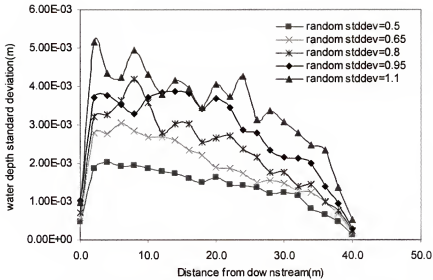


Figure 5-15. Water depth standard deviation along the centerline between upstream and downstream for Monte Carlo simulations with different standard deviation of Manning's coefficient at 900 sec.

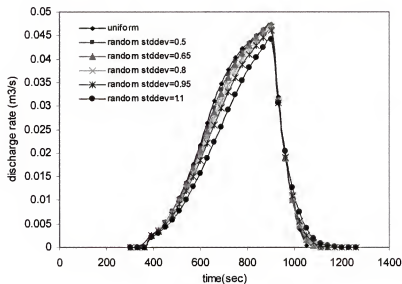


Figure 5-16. Comparison of surface runoff hydrographs for the uniform field and Monte Carlo simulations with different variability of Manning's coefficient.

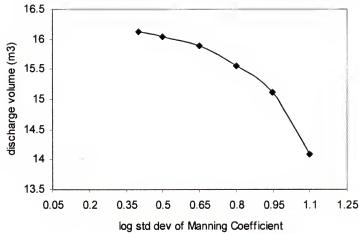


Figure 5-17. Total mean runoff discharge volume versus log standard deviation of Manning's Coefficient.

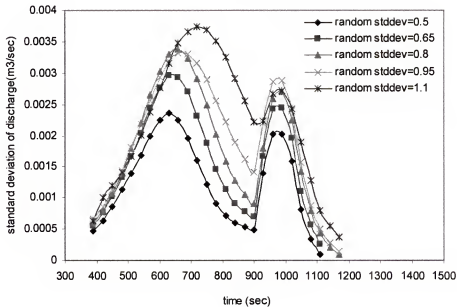


Figure 5-18. Comparison of standard deviations of discharge for Monte Carlo simulations with different variability of Manning's coefficient.

5.3.4 The Effects of Spatially Varied Microtopography on Surface Runoff

Similar procedures as discussed in the last two sections were followed to examine the effects of variability in microtopography on the surface runoff. Random fields of microtopography with standard deviations of 0.2, 0.3, 0.4 and 0.5 cm were evaluated in this case.

The uniform and mean Monte Carlo water depth curves along the centerline between upstream and downstream at 450 and 900 sec are shown in Figure 5-19 and Figure 5-21 respectively. At 450 sec Figure 5-19 shows the mean water depths generated from the Monte Carlo simulations for low variability (0.2, 0.3) are slightly lower than water depths generated from uniform field. The mean water depths generated from the Monte Carlo simulations for relatively high variability (0.4, 0.5) are slightly higher than mean water depths generated from uniform field. At 900 sec, the water depths generated from random fields are always lower than those generated from the uniform field. Increasing variability of microtopography leads to the decreasing mean water depths. From Figure 5-20 and Figure 5-22 we can see that the variability of water depth increases when the variability of microtopography increases.

Figure 5-23 shows the hydrographs obtained using the uniform field and the mean of the Monte Carlo simulations with different standard deviation values. From Figure 5-23 we can see no significant difference exists among the surface runoff starting and ending times for the different ensemble mean fields. On the rising limb, the higher the variability, the lower the ensemble mean runoff discharge rate. The mean discharge rate on the rising limb for all Monte Carlo simulations is lower than the uniform field value. On the recession limb, the ensemble mean discharge rate for each Monte Carlo simulation is very close to that for the uniform field. At 900 sec, the peak discharge rate

from the uniform field is higher than that from any random field. Table 5-4 summarizes the mean surface runoff starting time, ending time, discharge peak and total mean runoff volume for the different cases. Table 5-4 and Figure 5-24 show that the total discharge volume decreases as the variability in microtopography increases. All random fields have less surface runoff volume than the uniform field, except the random field with a standard deviation of 0.2, for which the total runoff volume is a slightly higher than that of the uniform one.

Table 5-4. Surface runoff starting time, ending time, peak and total volume for random surface elevation fields with different log standard deviation

| Hydrograph attributes | Log std dev | Uniform slope 0.02 | 0.2 | 0.3 | 0.4 | 0.5 |
|--------------------------------|-------------|--------------------|--------|--------|--------|--------|
| | | | | | | |
| Peak (m ³ /sec) | | 0.0475 | 0.0462 | 0.0457 | 0.0448 | 0.0444 |
| Starting time (sec) | | 337.45 | 360 | 360 | 360 | 360 |
| Ending time (sec) | | 1051 | 1050 | 1050 | 1050 | 1080 |
| Total volume (m ³) | | 16.30 | 16.66 | 15.98 | 15.65 | 15.37 |

Figure 5-25 shows standard deviations of discharge for the various Monte Carlo simulations. As the variability of microtopography increases, the variability of surface runoff increases. The standard deviation of surface runoff continues to increase with time for a short period after rainfall ceases at 900 sec, reaching its peak at about 930 sec, then decreases dramatically. Before 930 sec, the runoff standard deviation increases with time because the surface water depth at the downstream increases with time and is always less than the standard deviation of microtopography. After 930 sec, the water depth at downstream falls below the standard deviation of microtopography and decreases dramatically with time, thus runoff standard deviation decreases dramatically.

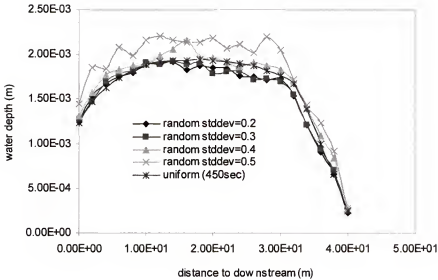


Figure 5-19. Water depth along the centerline between upstream and downstream for uniform field and Monte Carlo simulations with different standard deviation of microtopography at time 450 sec.

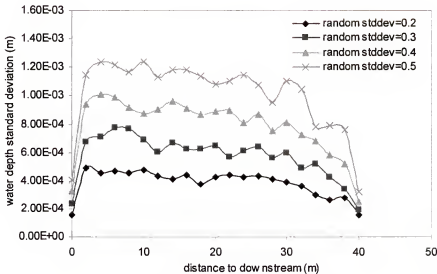


Figure 5-20. Water depth standard deviation along the centerline between upstream and downstream for uniform field and Monte Carlo simulations with different standard deviation of microtopography at time 450 sec.

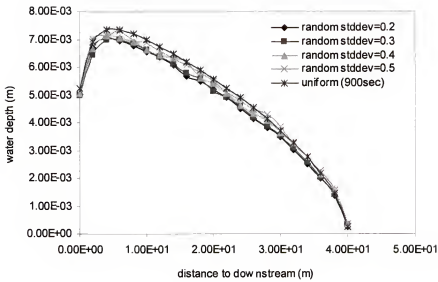


Figure 5-21. Water depth along the centerline between upstream and downstream for uniform field and Monte Carlo simulations with different standard deviation of microtopography at time 900 sec.

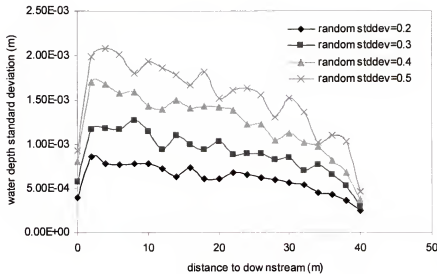


Figure 5-22. Water depth standard deviation along the centerline between upstream and downstream for uniform field and Monte Carlo simulations with different standard deviation of microtopography at time 450 sec.

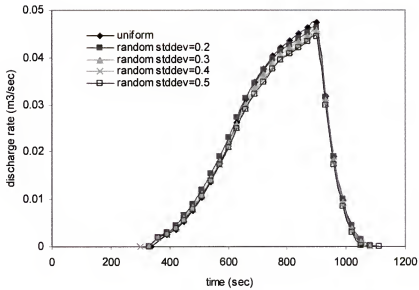


Figure 5-23. Comparison of surface runoff hydrographs for the uniform field and Monte Carlo simulations with different variability of microtopography.

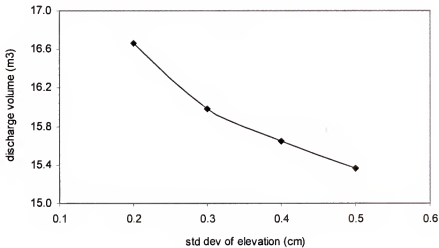


Figure 5-24. Total mean discharge volume versus standard deviation of microtopography.

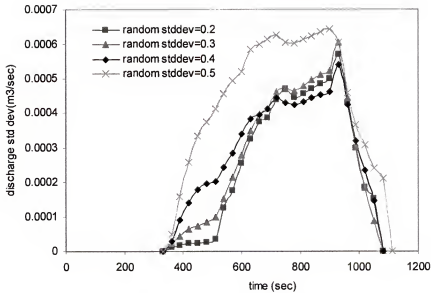


Figure 5-25. Comparison of standard deviations of discharge for Monte Carlo simulations with different variability of microtopography.

5.4 Conclusions

In this chapter, Monte Carlo simulations were conducted to analyze the impact of spatial variability in Manning's coefficient, saturated hydraulic conductivity and microtopography on surface runoff processes. The coefficients of variation of water depth at 450 and 900 sec, and the coefficient of variation of runoff rate at 900 sec were calculated using outputs from the Monte Carlo simulations for each of the three input random fields with a coefficient of variation (CV) of 0.95. The results are summarized in Table 5-5. The coefficients of variation of Manning's coefficient and saturated hydraulic conductivity were calculated using their arithmetic mean and arithmetic standard deviation. The coefficient of variation of microtopography was calculated using its standard deviation and the mean surface water depth at 900 sec for the uniform field since the mean variation of microtopography is zero for all cases. The coefficients of variation of the output variables were calculated using the mean and standard deviation of

that variable along the centerline between the upstream and downstream boundary. The runoff volume change in percent was calculated using the runoff volume for the uniform field as a reference.

Table 5-5. Comparison of outputs from Monte Carlo simulations for different spatially variable parameters with the same coefficient of variation (0.95)

| Outputs Parameter | CV of water depth at 450 sec | CV of water depth at 900 sec | Runoff peak change in percent (%) | Runoff volume change in percent (%) | CV of runoff rate at 900 sec |
|---------------------------|------------------------------------|------------------------------------|-----------------------------------------|-------------------------------------------|------------------------------------|
| Manning's coefficient | 0.39 | 0.42 | -1.47 | -4.60 | 0.02 |
| Hydraulic conductivity | 0.51 | 0.26 | -9.68 | 10.24 | 0.16 |
| Micro-topography | 0.53 | 0.31 | -6.53 | -5.70 | 0.01 |

The coefficient of variation of water depth changed from 0.39 at 450 sec to 0.42 at 900 sec for spatially variable Manning's coefficient; from 0.51 at 450 sec to 0.26 at 900 sec for spatially variable hydraulic conductivity; and from 0.53 at 450 sec to 0.31 at 900 sec for spatially variable microtopography. Thus as time increases, Manning's coefficient shows a slight increasing effect on the coefficient of variation of surface water depth. For microtopography and random hydraulic conductivity, the coefficient of variation of water depth decreases, falling significantly as time increases. Thus spatially variable microtopography and hydraulic conductivity have a greater effect on water depth prediction uncertainty at early times and Manning's coefficient has a slightly greater effect at later times.

Compared with the peak discharge for the uniform field, the mean peak discharge from all the Monte Carlo simulations is smaller. Random hydraulic conductivity shows the largest decrease (9.68%), while random Manning's coefficient shows the smallest decrease (1.47%). Compared with the uniform field, the mean total runoff volume

increases by 10.24% for the random hydraulic conductivity field, and decreases by 5.7% and 4.6% for random microtopography and Manning's coefficient fields, respectively. For spatially variable hydraulic conductivity, the coefficient of variation of surface runoff at 900 sec is 0.16, which is much higher than the values of 0.01 for spatially variable microtopography and 0.02 for spatially variable Manning's coefficient. To conclude, among the three spatially varied parameters, hydraulic conductivity demonstrates the greatest effect on mean and coefficient of variation of the peak runoff discharge rate and total mean runoff volume, while Manning's coefficient has greatest effect on coefficient of variation of the surface runoff water depth at later times.

Simulation results revealed that the spatial variability of saturated hydraulic conductivity, Manning's coefficient and microtopography also influences the mean surface runoff hydrograph in runoff starting time, and ending time. For spatially variable hydraulic conductivity, runoff begins earlier for the ensemble mean field than for the uniform field. For spatially variable microtopography and Manning's coefficient, mean surface runoff begins a little later compared to the uniform field. For all three parameters, the higher the variability, the longer the surface runoff lasts after rainfall ceases.

The uniform field represented by the geometric mean of hydraulic conductivity yields higher peak discharges, but lower total runoff volume than the the mean Monte Carlo runoff hydrograph. This was an expected trend, which is consistent with a previous study reported by Woolhiser and Goodrich (1988). The spatial variability of hydraulic conductivity exerts a greater influence on the runoff volume than on the peak discharge. This conclusion is consistent with studies conducted by Saghaian et al. (1995). The ensemble mean fields for Manning's coefficient and microtopography yield lower peak

discharges and runoff volume compared with the uniform field. The higher the variability of Manning's coefficient and microtopography, the lower the runoff peak and runoff volume are.

For spatially variable hydraulic conductivity, the standard deviation of surface runoff increases with time for the first half of the storm, then begins to decrease after the inflection point of the mean surface discharge hydrograph is reached. After the rainfall ceases at 900 sec, the variability of runoff decreases rapidly. For spatially variable Manning's coefficient, the standard deviation of surface runoff increases with time until midway through the storm (i.e. at the inflection point of the rising limb of the mean hydrograph) when the runoff variability begins to decrease. After the rainfall ceases, the variability of runoff starts to increase again. Variability is maximum at the inflection point of the recession limb of the mean hydrograph then decreases as all surface runoff leaves the domain. For spatially variable microtopography, the standard deviation of surface runoff increases with time until a short time after the rainfall stops, then the standard deviation of surface runoff begins to decrease.

With increasing variation in hydraulic conductivity, the mean water depth increases and is higher than the water depth for the uniform field, especially for earlier times. As time increases, the difference in water depth between the ensemble mean fields and uniform field decreases. For random Manning's coefficient, as time increases the difference in water depth between the mean field and uniform field increases. For spatially random microtopography, as time increases the difference in water depth between the ensemble mean fields and uniform field decreases.

CHAPTER 6

APPROXIMATE ANALYTICAL STOCHASTIC ANALYSIS OF COUPLED OVERLAND AND VADOSE ZONE FLOW

6.1. Introduction

Natural watersheds display spatial variability in topography, surface roughness, and soil infiltration capacity. The variability of those soil characteristics has significant impact on surface runoff in both peak flow rate and total volume, as well as the accuracy with which models are able to predict these quantities. The investigation of such spatial variability has been conducted using numerical Monte Carlo techniques to study the mean and variance of hydrologic outputs resulting from variability of input parameters, and by deriving approximate analytic expressions to predict the effects of variability of input parameters on the output variables. The Monte Carlo approach is in some ways a problem-specific blackbox approach and is often plagued by intensive computational demands, especially for highly non-linear systems. On the other hand the analytical approach has the advantage of facilitating the explicit analysis of output responses to input changes, and is computationally efficient, although it does require introducing some limiting assumptions.

Numerical techniques have been used to calculate prediction uncertainty of surface runoff. Smith and Hebbert (1979) examined the effects of random distribution of infiltration characteristics on the hydrologic performance of catchment areas. Freeze (1980) investigated the influence of spatial stochastic properties of hillslope parameters on the statistical properties of runoff events. Woolhiser and Goodrich (1988) studied the

influence of spatial variations of saturated hydraulic conductivity on the surface runoff for different storm intensities. Zhang and Cundy (1989) studied the effects of spatially varied roughness, infiltration and microtopography on the variability of surface runoff. Julien and Moglen (1990) examined the spatially uncorrelated variability in slope, roughness, width and excess rainfall on a one-dimensional runoff plane. Saghafian et al. (1995) examined the variability in Hortonian surface runoff discharge rate and volume produced by stationary rainstorms on watersheds with spatially distributed soil saturated hydraulic conductivity. Woolhiser et al. (1996) studied the effects of spatial variability of saturated hydraulic conductivity on Hortonian overland flow. Merz and Plate (1997) investigated the effects of spatial variability of infiltration parameters and initial soil moisture on the rainfall runoff process using a quasi-three-dimensional, process-oriented model SAKE / FGM. Seguis et al. (2002) investigated the impact on Hortonian runoff of stochastic and elevation-related spatial distributions of soil parameters.

While approximate analytical stochastic analysis has found many applications in saturated flow (e.g., Mizell et al., 1982; Graham and McLaughlin, 1989; Rubin, 1990; Gelhar, 1993; Zhang, 1998; Osnes, 1998), unsaturated flow (e.g., Dagan and Bresler, 1983; Bresler and Dagan, 1983; Hopmans et al., 1988; Mantoglou, 1992; Tartakovsky et al. 1999; Foussereau et al., 2000) and solute transport (e.g., Dagan, 1984, 1989; Li and Graham, 1998; Hassan, 2001), its applications on surface flow are scarce. Horritt (2002) used an approximate perturbation approach to investigate the effects of topographic uncertainty on shallow water flow. They found that the second order perturbation terms are significant in predicting nonlinear effects such as the shift in the mean water depth and an increase in the variance of water depth.

Heterogeneity in soil properties has posed a problem for distributed numerical models since their early applications. Distributed numerical models require a lot of input data, most of which can not be measured because of factors such as time, labor, money etc., so it is necessary to find a way to estimate those data. Usually data are measured at a scale that is much smaller than the numerical model scale so it is important to find effective parameter values for the larger-scale numerical models that acknowledge the variability of data measured at a smaller scale. Especially for lumped models, it is a challenge to find accurate physically based effective parameter values.

Approximate analytical stochastic analysis has been successfully applied to derive effective values of soil properties for upscaling saturated flow through heterogeneous fields. For the case of a stationary lognormal hydraulic conductivity distribution with isotropic autocovariance, a geometric mean of K_g , and a variance of σ_f , Gutjahr et al. (1978) found that the effective hydraulic conductivity was the harmonic mean for one dimensional saturated flow, the geometric mean (K_g) for two dimensional saturated flow and $K_g(1+\sigma_f^2/6)$ for three-dimensional saturated flow.

Dagan and Bresler (1983) and Bresler and Dagan (1983) demonstrated that the effective hydraulic conductivity may be meaningful for unsaturated flow only under very restricted and special conditions such as steady gravitational flow. They concluded that effective hydraulic conductivity does not exist in the general case of infiltration redistribution.

Dagan (1982) found that the effective conductivity for unsteady groundwater flow is time dependent. Studies by El-Kadi and Brutsaert (1985) complement this conclusion. Also, El-Kadi and Brutsaert (1985) found that the effective parameters depend on both

the distribution of the hydraulic conductivity and its spatial correlation. Thus in evaluating the effective conductivity for a subsurface heterogeneous media, both the nature of the spatial heterogeneities in hydraulic conductivity and the flow system operating within the flow domain must be considered.

Dykaar and Kitanidis (1992a, 1992b) introduced a numerical spectral method to compute the effective conductivity of a three-dimensional, isotropic, stationary, lognormally distributed hydraulic conductivity field. They found that for three-dimensional flow the effective hydraulic conductivity was $K_g \exp(\sigma_r^2 / 6)$ and for a Gaussian covariance function, heterogeneities smaller than about 1.3 integral scales did not significantly contribute to the effective conductivity. In two dimensions, effective conductivity was found to be close to the geometric mean, and the effective conductivity was insensitive to heterogeneities less than 2 integral scales in size.

Using the results of a fully three-dimensional model of variably saturated flow on a heterogeneous hillslope, Binley et al. (1989) found that effective parameters for saturated hydraulic conductivity reasonably reproduced the hillslope hydrograph for high-permeability soils, while single effective parameters failed to reproduce both subsurface and surface flow responses for low permeability soils.

In this chapter, we will present an analytical model based on stochastic perturbation techniques for the examination of the effects of spatial variability of land surface elevation, surface roughness, and hydraulic conductivity on surface runoff. Based on this model, we will derive the effective parameter values for hydraulic conductivity, Manning's coefficient and surface elevation, as well as expressions for the prediction uncertainty for water depth and runoff volumes.

6.2 A Stochastic Analytical Model for Predicting Surface Runoff Uncertainty

For convenience, we rewrite the continuity equation and the momentum equation for a two-dimensional diffusion wave overland flow model,

$$\frac{\partial h}{\partial t} + \frac{\partial(u_i h)}{\partial x_i} = i - f \quad (6-1)$$

$$gh\left(\frac{\partial(h+z)}{\partial x_i} + S_{f_{xi}}\right) = 0 \quad (6-2)$$

where i is the rainfall rate [L/T]; f is the infiltration rate[L/T]; h is the water depth[L]; $S_{f_{xi}}$ is the friction slope[--]; z is the surface elevation [L]; u_i is the flow velocity in i (x or y) direction [L/T]; g is the gravitational acceleration [9.81m/s²].

The velocity u_i can be expressed as a function of Manning's coefficient, water depth and surface slope,

$$u_i = \frac{h^{2/3} S_{f_{xi}}^{1/2}}{n} \quad (6-3)$$

For simplification, the infiltration rate is calculated by the Green-Ampt equation. Thus overland flow and unsaturated flow are uncoupled, and no iterations are necessary to determine the infiltration rate.

$$f = K_s \left(1 + \frac{H_f + h}{F} M_d \right) \quad (6-4)$$

where F is the accumulated infiltration [L]; K_s is the saturated hydraulic conductivity of soil [L/T]; H_f is the capillary pressure at the wetting front [L]; M_d is the soil moisture deficit, with $M_d = \theta_e - \theta_i$; θ_i is the initial moisture content; θ_e is the effective porosity with $\theta_e = \theta_s - \theta_r$; θ_s is the saturated soil moisture content; θ_r is the residual moisture content. It should be noted that the Green-Ampt equation requires several restricting

assumptions such as an abrupt wetting front, saturated soil behind the wetting front, constant saturated hydraulic conductivity with depth, no significant entrapped air and no significant surface sealing.

Combining Equations 6-1 through 6-4 we obtain

$$\frac{\partial h}{\partial t} + \frac{\partial}{\partial x_i} \left(\frac{h^{5/3} S_{fai}^{1/2}}{n} \right) = i - K_s \left(1 + \frac{H_f + h}{F} M_d \right) \quad (6-5)$$

From Equation 6-2 we have

$$S_{fai} = - \frac{\partial(h+z)}{\partial x_i} \quad (6-6)$$

When any of the three parameters, saturated hydraulic conductivity, surface elevation and Manning's coefficient, is regarded as a spatial stochastic process, Equation 6-5 becomes a stochastic differential equation in which friction slope S_{fai} and the solution h will also become stochastic processes. If we assume that the random processes can be written in terms of their mean and a zero-mean perturbation, our goal is to find the perturbation of water depth resulting from the small perturbation of Manning's coefficient, microtopography or saturated hydraulic conductivity. Specifically we are interested in finding the variations of water depth expressed in terms of the variations of hydraulic conductivity, Manning's coefficient or microtopography.

We assume that the Manning's coefficient and saturated hydraulic conductivity have stationary log normal distribution, while microtopography has stationary normal distribution, The random processes of n , K_s and z are written in terms of their expected value, or mean, plus a zero-mean perturbation, as

$$\ln K_s = \bar{K}_s + K'_s \quad E[\ln K_s] = \bar{K}_s \quad E[K'_s] = 0,$$

$$\ln n = \bar{n}_l + n'_l \quad E[\ln n] = \bar{n}_l \quad E[n'_l] = 0, \quad (6-7)$$

$$z = \bar{z} + z' \quad E[z] = \bar{z} \quad E[z'] = 0$$

where \bar{K}_l , K'_l are the mean and perturbation of log saturated hydraulic conductivity respectively; \bar{n}_l , n'_l are the mean and perturbation of log Manning's coefficient respectively; \bar{z} , z' are the mean and perturbation of surface elevation respectively.

Water depth can also be expressed as a mean and zero-mean perturbation

$$h = \bar{h} + h' \quad (6-8)$$

where \bar{h} and h' are the mean and zero-mean perturbation of water depth, respectively.

For linearization $1/n$, and K_s are expanded in Taylor-series.

$$\begin{aligned} \frac{1}{n} &= \exp[-(\bar{n}_l + n'_l)] = \exp(-\bar{n}_l) * \exp(-n'_l) = n_g^{-1} \exp(-n'_l) \approx n_g^{-1} (1 - n'_l) \\ K_s &= \exp(\bar{k}_l + k'_l) = \exp(\bar{k}_l) * \exp(k'_l) = K_g \exp(k'_l) \approx K_g (1 + k'_l) \end{aligned} \quad (6-9)$$

where n_g is the geometric mean of Manning's coefficient, and K_g is the geometric mean of saturated hydraulic conductivity.

$S_{fs}^{1/2}$ can be expressed in the following form

$$S_{fs}^{1/2} = \left(-\frac{\partial(h+z)}{\partial x} \right)^{1/2} = \left(-\frac{\partial(\bar{h} + h' + \bar{z} + z')}{\partial x} \right)^{1/2} = \sqrt{S_0} \left(1 - \frac{\partial(h' + z')/\partial x}{S_0} \right)^{1/2} \quad (6-10)$$

where $S_0 = -\frac{\partial \bar{z}}{\partial x}$ is the mean land surface slope.

In Equation 6-10, $\frac{\partial \bar{h}}{\partial x}$ is assumed to be zero, i.e. \bar{h} is spatially independent, which

is implied in Equation 6-8. This assumption is important because it greatly simplifies the analytic derivations. This assumption should be reasonable in large domains away from non-stationary boundary conditions, such as free outflow boundaries.

Expanding $S_{fx}^{1/2}$ in Equation 6-10 in Taylor-series expansion gives,

$$S_{fx}^{1/2} \approx \sqrt{S_0} \left(1 - \frac{\partial(h' + z')/\partial x}{2S_0} \right) = \sqrt{S_0} - \frac{1}{2\sqrt{S_0}} \left(\frac{\partial h'}{\partial x} + \frac{\partial z'}{\partial x} \right) \quad (6-11)$$

Expanding $h^{5/3}$ in Taylor-series gives,

$$h^{5/3} \approx \bar{h}^{5/3} + \frac{5}{3} \bar{h}^{2/3} (h - \bar{h}) = \bar{h}^{5/3} + \frac{5}{3} \bar{h}^{2/3} h' \quad (6-12)$$

Substituting Equations 6-9, 6-11 and 6-12 into Equation 6-5 we have,

$$\begin{aligned} & \frac{\partial(\bar{h} + h')}{\partial t} + \frac{\partial}{\partial x_i} \left(n_g^{-1} (1 - n'_i) \left(\bar{h}^{5/3} + \frac{5}{3} \bar{h}^{2/3} h' \right) \left(\sqrt{S_0} - \frac{1}{2\sqrt{S_0}} \left(\frac{\partial h'}{\partial x_i} + \frac{\partial z'}{\partial x_i} \right) \right) \right) \\ & = i - K_g (1 + K'_i) \left(1 + \frac{H_f + \bar{h} + h'}{F} M_d \right) \end{aligned} \quad (6-13)$$

Collecting mean and perturbation terms and neglecting second order products of perturbations gives the first-order mean and perturbation equations for \bar{h} and h' , respectively,

$$\frac{\partial \bar{h}}{\partial t} + \frac{\partial}{\partial x_i} \left(\frac{\bar{h}^{5/3} \sqrt{S_0}}{n_g} \right) = i - K_g \left(1 + \frac{H_f + \bar{h}}{F} M_d \right) \quad (6-14)$$

$$\begin{aligned} & \frac{\partial h'}{\partial t} + \frac{\partial}{\partial x_i} \left(- \frac{\bar{h}^{5/3}}{2n_g \sqrt{S_0}} \left(\frac{\partial h'}{\partial x_i} + \frac{\partial z'}{\partial x_i} \right) + \frac{5\sqrt{S_0} \bar{h}^{2/3}}{3n_g} h' - \frac{\sqrt{S_0} \bar{h}^{5/3}}{n_g} n'_i \right) \\ & = -K_g K'_i \left(1 + \frac{H_f + \bar{h}}{F} M_d \right) - \frac{K_g M_d}{F} h' \end{aligned} \quad (6-15)$$

Equation 6-14 has a form very similar to Equation 6-5. This equation indicates that the first-order mean water depth can be found by solving Equation 6-5 using the mean slope and geometric means of Manning's coefficient and hydraulic conductivity. After linearization, Equation 6-15 includes only four unknowns, n'_i , z' , K'_i and h' , and some constant coefficients.

From Equation 6-15, covariance equations can be derived for the water depth, and the cross-covariance between head, land surface elevation, hydraulic conductivity and Manning's coefficient. Pre-multiplying Equation 6-15 by surface elevation perturbation $z'(x')$, bringing this perturbation inside derivatives with respect to x and t , and taking the expected value gives the governing equation for $P_{zh}(x', x, t)$, which is the cross-covariance function between elevation and water depth,

$$\begin{aligned} \frac{\partial P_{zh}(x', x, t)}{\partial t} + \frac{\partial}{\partial x_i} \left(-\frac{\bar{h}^{5/3}}{2n_g \sqrt{S_0}} \left(\frac{\partial P_{zh}(x', x, t)}{\partial x_i} + \frac{\partial P_{zx}(x', x, t)}{\partial x_i} \right) + \frac{5\sqrt{S_0} \bar{h}^{2/3}}{3n_g} P_{zh}(x', x, t) - \frac{\sqrt{S_0} \bar{h}^{5/3}}{n_g} P_{zx}(x', x, t) \right) \\ = -K_g P_{zk}(x', x, t) \left(1 + \frac{H_f + \bar{h}}{F} M_d \right) - \frac{K_g M_d}{F} P_{zh}(x', x, t) \end{aligned} \quad (6-16)$$

where $P_{zz}(x', x, t)$ is the auto-covariance of surface elevation; $P_{zh}(x', x, t)$ is the cross-covariance function between surface elevation and water depth; $P_{zx}(x', x, t)$ is the cross-covariance function between surface elevation and the log Manning's coefficient and $P_{zk}(x', x, t)$ is the cross-covariance function between surface elevation and the log hydraulic conductivity.

Pre-multiplying Equation 6-15 by Manning's coefficient perturbation $n'_i(x')$, bringing this perturbation inside derivatives with respect to x and t , and taking the expected value gives the governing equation for $P_{nh}(x', x, t)$, which is the cross-covariance function between Manning's coefficient and water depth,

$$\begin{aligned} \frac{\partial P_{nh}(x', x, t)}{\partial t} + \frac{\partial}{\partial x_i} \left(-\frac{\bar{h}^{5/3}}{2n_g \sqrt{S_0}} \left(\frac{\partial P_{nh}(x', x, t)}{\partial x_i} + \frac{\partial P_{nm}(x', x, t)}{\partial x_i} \right) + \frac{5\sqrt{S_0} \bar{h}^{2/3}}{3n_g} P_{nh}(x', x, t) - \frac{\sqrt{S_0} \bar{h}^{5/3}}{n_g} P_{nm}(x', x, t) \right) \\ = -K_g P_{nk}(x', x, t) \left(1 + \frac{H_f + \bar{h}}{F} M_d \right) - \frac{K_g M_d}{F} P_{nh}(x', x, t) \end{aligned} \quad (6-17)$$

where $P_{nn}(x', x, t)$ is the auto-covariance of log Manning's coefficient; $P_{nh}(x', x, t)$ is the cross-covariance function between log Manning's coefficient and water depth; $P_{nz}(x', x, t)$ is the cross-covariance function between log Manning's coefficient and surface elevation and $P_{nk}(x', x, t)$ is the cross-covariance function between log Manning's coefficient and log hydraulic conductivity.

Pre-multiplying Equation 6-15 by log hydraulic conductivity perturbation $K'_i(x')$, bringing this perturbation inside derivatives with respect to x and t , and taking the expected value gives the governing equation for $P_{kh}(x', x, t)$, which is the cross-covariance function between log hydraulic conductivity and water depth,

$$\begin{aligned} \frac{\partial P_{kh}(x', x, t)}{\partial t} + \frac{\partial}{\partial x_i} \left(-\frac{\bar{h}^{5/3}}{2n_g \sqrt{S_0}} \left(\frac{\partial P_{kh}(x', x, t)}{\partial x_i} + \frac{\partial P_{ki}(x', x, t)}{\partial x_i} \right) + \frac{5\sqrt{S_0} \bar{h}^{2/3}}{3n_g} P_{kh}(x', x, t) - \frac{\sqrt{S_0} \bar{h}^{5/3}}{n_g} P_{ko}(x', x, t) \right) \\ = -K_g P_{KK}(x', x, t) \left(1 + \frac{H_f + \bar{h}}{F} M_d \right) - \frac{K_K M_d}{F} P_{kh}(x', x, t) \end{aligned} \quad (6-18)$$

where $P_{KK}(x', x, t)$ is the auto-covariance of log hydraulic conductivity; $P_{kh}(x', x, t)$ is the cross-covariance function between log hydraulic conductivity and water depth; $P_{ko}(x', x, t)$ is the cross-covariance function between log hydraulic conductivity and surface elevation and $P_{ki}(x', x, t)$ is the cross-covariance function between log hydraulic conductivity and log Manning's coefficient.

Post-multiplying Equation 6-15 expressed in x' by water depth perturbation $h'(x)$, bringing this perturbation inside derivatives with respect to x' and t , and taking the expected value give the governing equation for $P_{hh}(x', x, t)$,

$$\begin{aligned}
& \frac{\partial P_{hh}(x', x, t)}{\partial t} + \frac{\partial}{\partial x'_i} \left(-\frac{\bar{h}^{5/3}}{2n_g \sqrt{S_0}} \left(\frac{\partial P_{hh}(x', x, t)}{\partial x'_i} + \frac{\partial P_{zh}(x', x, t)}{\partial x'_i} \right) + \frac{5\sqrt{S_0} \bar{h}^{2/3}}{3n_g} P_{hh}(x', x, t) - \frac{\sqrt{S_0} \bar{h}^{5/3}}{n_g} P_{nh}(x', x, t) \right) \\
& = -K_K P_{Kh}(x', x, t) \left(1 + \frac{H_f + \bar{h}}{F} M_d \right) - \frac{K_g M_d}{F} P_{hh}(x', x, t) \quad (6-19)
\end{aligned}$$

where $P_{hh}(x', x, t)$ is the auto-covariance of water depth; $P_{zh}(x', x, t)$ is the cross-covariance function between surface elevation and water depth; and $P_{nh}(x', x, t)$ is the cross-covariance function between log Manning's coefficient and water depth, $P_{Kh}(x', x, t)$ is the cross-covariance function between log hydraulic conductivity and water depth.

Equations 6-15 through 6-19 are four coupled partial differential equations that resemble the original two-dimensional wave Equation 6-1. Generally, these equations must be solved numerically. Once these covariance equations have been solved, then higher-order corrections to the mean water depth can be determined. In Equation 6-16, the cross-covariance $P_{zh}(x', x, t)$ between the topography and the surface water depth is the unknown. This cross-covariance depends on $P_{zz}(x', x, t)$, $P_{zn}(x', x, t)$ and $P_{zK}(x', x, t)$, which must be specified before solution can be obtained. In Equation 6-17, the cross-covariance $P_{nh}(x', x, t)$ between the Manning's coefficient and the surface water depth is the unknown, and is dependent on $P_{nn}(x', x, t)$, $P_{nz}(x', x, t)$ and $P_{nK}(x', x, t)$, which must be specified a priori. In Equation 6-18, the cross-covariance $P_{Kh}(x', x, t)$ between the hydraulic conductivity and the surface water depth is the unknown, while $P_{KK}(x', x, t)$, $P_{Kz}(x', x, t)$ and $P_{Kn}(x', x, t)$ are the required inputs. In Equation 6-19, the auto-covariance $P_{hh}(x', x, t)$ is the unknown while $P_{zh}(x', x, t)$, $P_{nh}(x', x, t)$ and $P_{Kh}(x', x, t)$, which are the solutions to Equations 6-16, 6-17 and 6-18, are the required inputs.

6.3 Solution of Covariance Equations for the Steady-State 1-D Stationary Case

6.3.1 Water Depth Variance

In general, covariance Equations 6-16 through 6-19 must be solved numerically. However, in special cases, approximate analytical solutions can be found. In this section, we will derive approximate analytical solutions by introducing several assumptions. If we assume the runoff process has reached steady state and cumulative infiltration is large, then we can neglect transient terms in Equations 6-16 through 6-19. If we assume that the perturbations of hydraulic conductivity, Manning's coefficient and microtopography are not correlated with each other, then the cross-covariance terms, $P_{zn}(x', x, t)$, $P_{zk}(x', x, t)$, $P_{nz}(x', x, t)$, $P_{nk}(x', x, t)$, $P_{kz}(x', x, t)$ and $P_{kn}(x', x, t)$, in Equations 6-16 through 6-19 are all equal to zero. If we assume that the input and output fields are spatially stationary, i.e. S_0 , \bar{h} , \bar{n}_g and \bar{K}_g are constant in space, then all the coefficients in Equations 6-16 through 6-19 are constant. As a result of these assumptions no nonlinear terms exist in Equation 6-15 and all coefficients are spatially constant. Thus it is suitable for solution using Fourier transform techniques.

Taking into account all the assumptions we have discussed, Equations 6-16 through 6-19 can be rewritten in ζ , where $\zeta = x - x'$, and therefore $\partial x = \partial \zeta$ and $\partial x' = -\partial \zeta$.

$$-\frac{\bar{h}^{5/3}}{2n_g\sqrt{S_0}}\frac{\partial^2 P_{zz}(\zeta)}{\partial \zeta^2} - \frac{\bar{h}^{5/3}}{2n_g\sqrt{S_0}}\frac{\partial^2 P_{zh}(\zeta)}{\partial \zeta^2} + \frac{5\sqrt{S_0}\bar{h}^{2/3}}{3n_g}\frac{\partial P_{zh}(\zeta)}{\partial \zeta} = 0 \quad (6-20)$$

$$-\frac{\bar{h}^{5/3}}{2n_g\sqrt{S_0}}\frac{\partial^2 P_{nh}(\zeta)}{\partial \zeta^2} + \frac{5\sqrt{S_0}\bar{h}^{2/3}}{3n_g}\frac{\partial P_{nh}(\zeta)}{\partial \zeta} - \frac{\sqrt{S_0}\bar{h}^{5/3}}{n_g}\frac{\partial P_{nn}(\zeta)}{\partial \zeta} = 0 \quad (6-21)$$

$$-\frac{\bar{h}^{5/3}}{2n_g\sqrt{S_0}}\frac{\partial^2 P_{Kh}(\zeta)}{\partial \zeta^2} + \frac{5\sqrt{S_0}\bar{h}^{2/3}}{3n_g}\frac{\partial P_{Kh}(\zeta)}{\partial \zeta} = -K_g P_{KK}(\zeta) \quad (6-22)$$

$$-\frac{\bar{h}^{5/3}}{2n_g\sqrt{S_0}}\frac{\partial^2 P_{zh}(\zeta)}{\partial \zeta^2} - \frac{\bar{h}^{5/3}}{2n_g\sqrt{S_0}}\frac{\partial^2 P_{hh}(\zeta)}{\partial \zeta^2} - \frac{5\sqrt{S_0}\bar{h}^{2/3}}{3n_g}\frac{\partial P_{hh}(\zeta)}{\partial \zeta} + \frac{\sqrt{S_0}\bar{h}^{5/3}}{n_g}\frac{\partial P_{nh}(\zeta)}{\partial \zeta} = -K_g P_{Kh}(\zeta) \quad (6-23)$$

Using Fourier transform techniques, differential Equations 6-20 through 6-23 for the auto- and cross- covariance functions can be transformed to algebraic relationships for the auto- and cross- spectra functions.

$$-\frac{\bar{h}^{5/3}}{2n_g\sqrt{S_0}}(-iK)^2 S_{zz}(K) - \frac{\bar{h}^{5/3}}{2n_g\sqrt{S_0}}(-iK)^2 S_{zh}(K) + \frac{5\sqrt{S_0}\bar{h}^{2/3}}{3n_g}(-iK)S_{zh}(K) = 0 \quad (6-24)$$

$$-\frac{\bar{h}^{5/3}}{2n_g\sqrt{S_0}}(-iK)^2 S_{nh}(K) + \frac{5\sqrt{S_0}\bar{h}^{2/3}}{3n_g}(-iK)S_{nh}(K) - \frac{\sqrt{S_0}\bar{h}^{5/3}}{n_g}(-iK)S_{nn}(K) = 0 \quad (6-25)$$

$$-\frac{\bar{h}^{5/3}}{2n_g\sqrt{S_0}}(-iK)^2 S_{Kh}(K) + \frac{5\sqrt{S_0}\bar{h}^{2/3}}{3n_g}(-iK)S_{Kh}(K) = -K_g S_{KK}(K) \quad (6-26)$$

$$-\frac{\bar{h}^{5/3}}{2n_g\sqrt{S_0}}(-iK)^2 S_{zh}(K) - \frac{\bar{h}^{5/3}}{2n_g\sqrt{S_0}}(-iK)^2 S_{hh}(K) - \frac{5\sqrt{S_0}\bar{h}^{2/3}}{3n_g}(-iK)S_{hh}(K) \quad (6-27)$$

$$+ \frac{\sqrt{S_0}\bar{h}^{5/3}}{n_g}(-iK)S_{nh}(K) = -K_g S_{Kh}(K)$$

where K is the wave number and $S_{hh}(K)$, $S_{zz}(K)$, $S_{nn}(K)$, $S_{KK}(K)$, $S_{zh}(K)$, $S_{nh}(K)$,

$S_{Kh}(K)$ are the spectra of $P_{hh}(\zeta)$, $P_{zz}(\zeta)$, $P_{nn}(\zeta)$, $P_{KK}(\zeta)$, $P_{zh}(\zeta)$, $P_{nh}(\zeta)$ and

$P_{Kh}(\zeta)$ respectively.

From Equations 6-24 through 6-27 we get

$$S_{zh}(k) = \frac{-iK}{iK + \frac{10S_0}{3\bar{h}}} S_{zz}(k) \quad (6-28)$$

$$S_{nh}(k) = \frac{2S_0}{iK + \frac{10S_0}{3h}} S_{nn}(k) \quad (6-29)$$

$$S_{kh}(k) = \frac{2\sqrt{S_0} n_g / \bar{h}^{5/3}}{iK + \frac{10S_0}{3h}} \frac{K_g S_{Kk}(k)}{iK} \quad (6-30)$$

$$S_{hh}(k) = \frac{\frac{\bar{h}^{5/3}}{2\sqrt{S_0} n_g} (-iK) S_{zh}(k) - \bar{h}^{5/3} \frac{\sqrt{S_0}}{n_g} S_{nh}(k) + \frac{K_g S_{Kh}(k)}{iK}}{\frac{\bar{h}^{5/3}}{2\sqrt{S_0} n_g} (iK) - \frac{5}{3} \bar{h}^{2/3} \frac{\sqrt{S_0}}{n_g}} \quad (6-31)$$

Substituting Equations 6-28 to 6-30 into Equation 6-31,

$$S_{hh}(k) = \frac{K^2}{K^2 + \left(\frac{10 S_0}{3 \bar{h}}\right)^2} S_{zz}(k) + \frac{(2S_0)^2}{K^2 + \left(\frac{10 S_0}{3 \bar{h}}\right)^2} S_{nn}(k) + \frac{\left(2\sqrt{S_0} n_g K_g / \bar{h}^{5/3}\right)^2}{K^2 \left(K^2 + \left(\frac{10 S_0}{3 \bar{h}}\right)^2\right)} S_{KK}(k) \quad (6-32)$$

To solve Equations 6-28 to 6-31, we assume an exponential auto-covariance function for both log n and z. To produce a finite stationary water depth process, we are required to introduce a hole-type function for log K. The hole-type function for log K has been used by Gelhar et al. (1993) to obtain reasonable solutions in other hydrologic analyses. Thus the auto-covariance functions of log n, z and log K can be written as:

$$P_{zz}(\zeta) = \sigma_z^2 e^{-|\zeta|/\lambda_z} \quad (6-33)$$

$$P_{nn}(\zeta) = \sigma_{\ln n}^2 e^{-|\zeta|/\lambda_n} \quad (6-34)$$

$$P_{KK}(\zeta) = \sigma_{\ln K}^2 \left(1 - \frac{|\zeta|}{l_K}\right) e^{-|\zeta|/l_K} \quad (6-35)$$

where λ_z , λ_n and l_K are correlation scales and σ_z^2 , $\sigma_{\ln n}^2$ and $\sigma_{\ln K}^2$ are the variances of z, n and K_s respectively.

The auto-spectrum for surface elevation z , Manning's coefficient n and hydraulic conductivity K corresponding to these auto-covariance functions are,

$$S_{zz}(k) = \frac{\sigma_z^2 \lambda_z}{\pi (1 + \lambda_z^2 k^2)} \quad (6-36)$$

$$S_{nn}(k) = \frac{\sigma_{\ln n}^2 \lambda_n}{\pi (1 + \lambda_n^2 k^2)} \quad (6-37)$$

$$S_{KK}(k) = \frac{2\sigma_{\ln K}^2 l_K^3 k^2}{\pi (1 + l_K^2 k^2)^2} \quad (6-38)$$

Substituting Equations 6-36 to 6-38 into Equation 6-32, the auto-spectrum of h is

$$\begin{aligned} S_{hh}(k) = & \frac{K^2}{K^2 + \left(\frac{10}{3} \frac{S_0}{h}\right)^2} \frac{\sigma_z^2 \lambda_z}{\pi (1 + \lambda_z^2 k^2)} + \frac{(2S_0)^2}{K^2 + \left(\frac{10}{3} \frac{S_0}{h}\right)^2} \frac{\sigma_{\ln n}^2 \lambda_n}{\pi (1 + \lambda_n^2 k^2)} \\ & + \frac{\left(2\sqrt{S_0} n_g K_g / \bar{h}^{5/3}\right)^2}{K^2 + \left(\frac{10}{3} \frac{S_0}{h}\right)^2} \frac{2\sigma_{\ln K}^2 l_K^3}{\pi (1 + l_K^2 k^2)^2} \end{aligned} \quad (6-39)$$

The variance of h can be derived by integrating Equation 6-39,

$$\begin{aligned} \sigma_h^2 = \int_{-\infty}^{\infty} S_{hh}(k) dk = & \int_{-\infty}^{\infty} \frac{K^2}{K^2 + \left(\frac{10}{3} \frac{S_0}{h}\right)^2} \frac{\sigma_z^2 \lambda_z}{\pi (1 + \lambda_z^2 k^2)} dk \\ & + \int_{-\infty}^{\infty} \frac{(2S_0)^2}{K^2 + \left(\frac{10}{3} \frac{S_0}{h}\right)^2} \frac{\sigma_{\ln n}^2 \lambda_n}{\pi (1 + \lambda_n^2 k^2)} dk + \int_{-\infty}^{\infty} \frac{\left(2\sqrt{S_0} n_g K_g / \bar{h}^{5/3}\right)^2}{K^2 + \left(\frac{10}{3} \frac{S_0}{h}\right)^2} \frac{2\sigma_{\ln K}^2 l_K^3}{\pi (1 + l_K^2 k^2)^2} dk \end{aligned} \quad (6-40)$$

Equation 6-40 indicates that the total variance of h is the linear addition of variance terms resulting from random processes of elevation, Manning's coefficient and hydraulic conductivity. This result is based on the linearization of the original governing equation and the assumption that elevation, Manning's coefficient and hydraulic conductivity are uncorrelated.

If we let $A = \frac{10 S_0}{3 \bar{h}}$, then the first term on the right side of Equation 6-40, which calculates uncertainty in predicting water depth resulting from spatial variability of surface topography, can be expressed

$$\sigma_z^2 = \int_{-\infty}^{\infty} \frac{K^2}{K^2 + A^2} \frac{\sigma_z^2 \lambda_z}{\pi (1 + \lambda_z^2 k^2)} dK = \frac{\sigma_z^2}{1 + A \lambda_z} \quad (6-41)$$

This result is identical to Expression 9 in Horritt (2002), who derived this expression for a steady-state diffusion wave shallow water flow using a power series expansion technique. According to Equation 6-41 the variation in water depth decreases as mean surface slope and correlation scale of surface elevation λ_z increase, and as the variation of surface topography σ_z^2 and mean water depth \bar{h} decrease.

If $A \lambda_z \ll 1$, which occurs when water depth (expressed in the same unit as correlation scale) is much greater than mean surface slope, then $\sigma_h^2 = \sigma_z^2$. If $A \lambda_z \gg 1$, (which occurs when water depth is very shallow), then $\sigma_h^2 = \frac{\sigma_z^2}{A \lambda_z}$.

For the second term on the right side of Equation 6-40, which calculates uncertainty in predicting water depth resulting from spatial variability of Manning's coefficient,

$$\sigma_h^2 = \int_{-\infty}^{\infty} \frac{(2S_0)^2}{K^2 + A^2} \frac{\sigma_{\ln n}^2 \lambda_n}{\pi (1 + \lambda_n^2 k^2)} dK = \frac{\lambda_n}{A(1 + A \lambda_n)} (2S_0)^2 \sigma_{\ln n}^2 \quad (6-42)$$

Equation 6-42 tells us that the variation of water depth increases as mean surface slope, correlation scale of Manning's coefficient, mean water depth and the variation of Manning's coefficient increase.

If $A\lambda_n \gg 1$, then $\sigma_h^2 = \left(\frac{2S_0}{A}\right)^2 \sigma_{\ln n}^2 = \left(\frac{3\bar{h}}{5}\right)^2 \sigma_{\ln n}^2$, which is independent of λ_n .

For the third term on the right side of Equation 6-40, which calculates uncertainty in predicting water depth resulting from spatial variability of hydraulic conductivity,

$$\sigma_h^2 = \int_{-\infty}^{\infty} \frac{\left(2\sqrt{S_0} n_g K_g / \bar{h}^{5/3}\right)^2}{K^2 + A^2} \frac{2\sigma_{\ln K}^2 l_K^2}{\pi(1 + l_K^2 k^2)} dK = \frac{Al_K + 2}{A(Al_K + 1)^2} \left(\frac{2\sqrt{S_0} n_g K_g}{\bar{h}^{5/3}}\right)^2 \sigma_{\ln K}^2 l_K^2 \quad (6-43)$$

Equation 6-43 tells us the variation of water depth increases as the geometric mean of Manning's coefficient, geometric mean of hydraulic conductivity and the correlation scale of hydraulic conductivity increase, and as the mean water depth and mean surface

slope decrease. If $A\lambda_K \gg 2$, then $\sigma_h^2 = \left(\frac{3}{5} \frac{n_g K_g}{\bar{h}^{2/3} \sqrt{S_0}}\right)^2 l_K^2 \sigma_{\ln K}^2$, which is a function the

geometric mean of Manning's coefficient, surface slope, hydraulic conductivity, mean water depth, and the standard deviation and correlation scale of hydraulic conductivity.

6.3.2 Surface Water Discharge Variance

The covariance function of surface water discharge from the downstream boundary can be derived from the downstream boundary condition,

$$q = \sqrt{g} h^{3/2} \quad (6-44)$$

Expressing q and h as the sum of a mean and a perturbation, and expanding $h^{3/2}$ in a first order Taylor-series lead to,

$$\bar{q} + q' = \sqrt{g} (\bar{h}^{3/2} + \frac{3}{2} \bar{h}^{1/2} h') \quad (6-45)$$

where \bar{q} and q' are the mean and perturbation of water flux respectively, and \bar{h} and h' are the mean and perturbation of water depth respectively,

Collecting mean and perturbation terms gives the first-order mean and perturbation equations for \bar{q} and q' respectively.

$$\bar{q} = \sqrt{g\bar{h}}^{3/2} \quad (6-46)$$

$$q' = \frac{3}{2}\sqrt{g\bar{h}}h' \quad (6-47)$$

The covariance function of water flux can be obtained by pre-multiplying Equation 6-47 by a perturbation in $q'(x')$. Expressing $\zeta = x - x'$, and taking the expected value give

$$P_{qq}(\zeta) = \frac{3}{2}\sqrt{g\bar{h}}P_{qh}(\zeta) \quad (6-48)$$

The cross-covariance function between surface water discharge and water depth can be obtained by post-multiplying Equation 6-47 expressed in x' by water depth a perturbation $h'(x)$, and taking the expected value.

$$P_{qh}(\zeta) = \frac{3}{2}\sqrt{g\bar{h}}P_{hh}(\zeta) \quad (6-49)$$

Substituting Equation 6-49 into Equation 6-48 gives,

$$P_{qq}(\zeta) = \frac{9}{4}g\bar{h}P_{hh}(\zeta) \quad (6-50)$$

So the variance of water flux can be expressed as a function of the variance of water depth by setting ζ equal to 0 in Equation 6-50,

$$\sigma_q^2 = \frac{9}{4}g\bar{h}\sigma_h^2 \quad (6-51)$$

6.4 Deriving the Effective Parameters for the Steady State 1-D Stationary Case

Based on the stochastic model developed in the last section, the effective parameter values for Manning's coefficient, hydraulic conductivity and surface slope can

be derived using the cross-covariance between Manning's coefficient and water depth, hydraulic conductivity and water depth, and surface slope and water depth to evaluate the second order correction terms to the mean equations.

6.4.1. Effective Manning's coefficient

From Manning's equation, flow rate can be expressed as

$$q = \frac{h^{5/3} S_{fx}^{1/2}}{n} \quad (6-52)$$

Expanding h and $1/n$ in a Taylor-series, neglecting higher order terms, assuming S_{fx} is deterministic, and taking the expected value gives

$$\begin{aligned} E[q] &= E \left[\left(\bar{h}^{5/3} + \frac{5}{3} \bar{h}^{2/3} h' + \frac{5}{9} \bar{h}^{-1/3} h'^2 \right) S_{fx}^{1/2} n_k^{-1} \left(1 - n'_i + \frac{n_i'^2}{2} \right) \right] \\ &= S_{fx}^{1/2} n_k^{-1} E \left[\bar{h}^{5/3} - \bar{h}^{5/3} n'_i + \frac{\bar{h}^{5/3}}{2} n_i'^2 + \frac{5}{3} \bar{h}^{2/3} h' - \frac{5}{3} \bar{h}^{2/3} h' n'_i + \frac{5}{9} \bar{h}^{-1/3} h'^2 \right] \end{aligned} \quad (6-53)$$

Recalling that $E[h'] = E[n'_i] = 0$, $P_{nh}(0) = E[n'_i(x)h'(x)]$,

$\sigma_n^2 = P_{nn}(0) = E[n'_i(x)n'_i(x)]$, and $\sigma_h^2 = P_{hh}(0) = E[h'(x)h'(x)]$, then Equation 6-53 can be simplified to,

$$E[q] = \left(1 - \frac{5}{3\bar{h}} P_{nh}(0) + \frac{1}{2} \sigma_n^2 + \frac{5}{9\bar{h}^2} \sigma_h^2 \right) n_k^{-1} \bar{h}^{5/3} S_{fx}^{1/2} \quad (6-54)$$

The cross-covariance between the Manning's coefficient and water depth can be obtained by substituting Equation 6-37 into Equation 6-29 and performing the inverse Fourier transform,

$$P_{nh}(0) = \int_{-\infty}^{\infty} \frac{2S_0}{iK + A} \frac{\sigma_{\ln n}^2 \lambda_n}{\pi(1 + \lambda_n^2 k^2)} dK = \frac{2S_0 \lambda_n}{1 + A \lambda_n} \sigma_{\ln n}^2 \quad (6-55)$$

If $A \lambda_n \gg 1$, then

$$P_{nh}(0) = \frac{2S_0}{A} \sigma_{\ln n}^2 \quad (6-56)$$

Substituting Equation 6-56 and the expression for A into Equation 6-54 gives

$$E[q] = \left(1 - \sigma_{\ln n}^2 + \frac{1}{2} \sigma_{\ln n}^2 + \frac{1}{5} \sigma_{\ln n}^2\right) n_g^{-1} \bar{h}^{5/3} S_{fx}^{1/2} = \left(1 - \frac{3}{10} \sigma_{\ln n}^2\right) n_g^{-1} \bar{h}^{5/3} S_{fx}^{1/2} \quad (6-57)$$

Assuming the effective flux $q_e = E[q] = \frac{\bar{h}^{5/3} S_{fx}^{1/2}}{n_e}$ and $n_e = n_g + n_c$, where n_e is the

effective Manning's coefficient, and n_c is the correction term to Manning's coefficient,

$$n_c = \frac{3\sigma_{\ln n}^2}{10 - 3\sigma_{\ln n}^2} n_g \quad (6-58)$$

Equation 6-58 is only valid when $\sigma_{\ln n}^2$ is less than 10/3. This condition should be satisfied for physically reasonable situations. Equation 6-58 indicates that as the variability in Manning's coefficient increases, the effective value of Manning's coefficient increases.

6.4.2 Effective Surface Slope

According to the kinematic assumption for overland flow, the friction slope S_f can be approximated as S_0 . It has been shown that only for very flat ($S_0 < 0.002$) or very steep ($S_0 > 0.10$) slopes is the kinematic assumption violated (Munoz-Carpena et al., 1993).

Therefore, invoking this assumption, expressing $S_0 = \bar{S}_0 + S'$ and expanding $S_{fx}^{1/2}$ in

Taylor-series,

$$S_{fx}^{1/2} \approx (S_0)^{1/2} = (\bar{S}_0 + S')^{1/2} \approx \sqrt{\bar{S}_0} \left(1 + \frac{S'}{2\bar{S}_0} - \frac{S'^2}{8\bar{S}_0^2}\right) = \sqrt{\bar{S}_0} + \frac{S'}{2\sqrt{\bar{S}_0}} - \frac{S'^2}{8\bar{S}_0^{3/2}} \quad (6-59)$$

Assuming n is deterministic, substituting Equation 6-59 and the Taylor-series expansion for h into Equation 6-52 and taking expectations gives,

$$E[q] = E \left[(\bar{h}^{5/3} + \frac{5}{3} \bar{h}^{2/3} h' + \frac{5}{9} \bar{h}^{-1/3} h'^2) \left(\sqrt{\bar{S}_0} + \frac{S'}{2\sqrt{\bar{S}_0}} - \frac{S'^2}{8\bar{S}_0^{3/2}} \right) / n \right] \quad (6-60)$$

Following the similar procedures used to derive n_c , we have

$$E[q] = \frac{\bar{h}^{5/3} \sqrt{\bar{S}_0}}{n} \left(1 - \frac{\sigma_s^2}{8\bar{S}_0^2} + \frac{5P_{sh}(0)}{6\bar{S}_0 \bar{h}} + \frac{5\sigma_h^2}{9\bar{h}^2} \right) \quad (6-61)$$

$P_{sh}(0)$, σ_s^2 and $P_{hh}(0)$ can be obtained from $P_{sh}(\zeta)$ and $P_{hh}(\zeta)$ (see Appendix D for details)

$$P_{sh}(0) = -\frac{3\bar{h}}{10\bar{S}_0} \sigma_s^2 \quad (6-62)$$

$$P_{hh}(0) = \left(\frac{3\bar{h}}{10\bar{S}_0} \right)^2 \sigma_s^2 \quad (6-63)$$

$$P_{ss}(0) = \sigma_s^2 = \frac{\sigma_z^2}{\lambda_z^2} \quad (6-64)$$

Substituting Equations 6-62 and 6-63 into Equation 6-61 gives

$$E[q] = \frac{\bar{h}^{5/3} \sqrt{\bar{S}_0}}{n} \left(1 - \frac{13\sigma_s^2}{40\bar{S}_0^2} \right) \quad (6-65)$$

If we write S_0 as \bar{S}_0 and a correction term S_c , then,

$$S_0^{1/2} = (\bar{S}_0 + S_c)^{1/2} \approx \sqrt{\bar{S}_0} \left(1 + \frac{S_c}{2\bar{S}_0} \right) = \sqrt{\bar{S}_0} + \frac{S_c}{2\sqrt{\bar{S}_0}} \quad (6-66)$$

From Equations 6-64 through 6-66, we can get S_c ,

$$S_c = -\frac{13\sigma_s^2}{20\bar{S}_0} = -\frac{13\sigma_z^2}{20\bar{S}_0 \lambda_z^2} \quad (6-67)$$

With the same microtopography variability, the higher the mean slope (\bar{S}_0), the less impact the microtopography variation has on surface runoff, thus less slope

correction is needed and S_c decreases. Equation 6-48 tells us that when the variability of microtopography increases, the effective value of surface slope decreases.

6.4.3 Effective Hydraulic Conductivity

For convenience, we rewrite the Green-Ampt Equation 6-4 here

$$f = K_s \left(1 + \frac{H_f + h}{F} M_d \right) \quad (6-68)$$

Expanding K_s and h into the sum of mean and perturbation terms as before, and taking expectations give

$$E[f] = E \left[\left(K_g (1 + K'_f) \left(1 + \frac{H_f + \bar{h} + h'}{F} M_d \right) \right) \right] = K_g \left(1 + \frac{H_f + \bar{h}}{F} M_d \right) + K_g \frac{P_{kh}}{F} M_d \quad (6-69)$$

The correction term, K_c , for K can be expressed as

$$K_c \left(1 + \frac{H_f + \bar{h}}{F} M_d \right) = K_g \frac{P_{kh}}{F} M_d \quad (6-70)$$

The cross-covariance between water depth and saturated hydraulic conductivity can be obtained by substituting Equation 6-38 into Equation 6-30 and performing the inverse Fourier transformation,

$$P_{kh}(0) = \int_{-\infty}^{\infty} \frac{2\sqrt{S_0} n_g K_g / \bar{h}^{5/3}}{iK(iK + A)} \frac{2\sigma_{\ln K}^2 \lambda_K^3}{\pi(1 + \lambda_K^2 k^2)} dK = -\frac{2\sqrt{S_0} n_g K_g}{\bar{h}^{5/3}} \frac{\lambda_K^2}{(A\lambda_K + 1)^2} \sigma_{\ln K}^2 \quad (6-71)$$

Substituting Equation 6-71 into 6-70, the expression for K_c can be written as

$$K_c = \frac{K_g M_d}{F + (H_f + \bar{h}) M_d} P_{kh} = -\frac{M_d}{F + (H_f + \bar{h}) M_d} \frac{2\sqrt{S_0} n_g K_g^2}{\bar{h}^{5/3}} \frac{\lambda_K^2}{(A\lambda_K + 1)^2} \sigma_{\ln K}^2 \quad (6-72)$$

From Equation 6-72, it is evident that when F , \bar{h} and H_f increase, K_c decreases.

When F , i.e. the cumulative infiltration, and h increase, from Equation 6-43 we know that the standard deviation of water depth decreases, so less K correction is needed. The

infiltration rate is determined by both geometric mean hydraulic conductivity, K_s , and capillary pressure at the wetting front H_f , so when H_f increases, for an equal infiltration rate, the contribution to infiltration by K_s decreases, so K_c decreases. If M_d increases, then for the same time of infiltration, F decreases, so K_c increases.

From Equations 6-58, 6-67 and 6-72, it is apparent that the corrections for Manning's coefficient and surface slope remain constant over time, while the correction to the hydraulic conductivity is a function of water depth which varies over time. When cumulative infiltration increases, the correction decreases until it is close to zero when F approaches infinity.

6.5 Verification of Analytical Models for Predicting Surface Runoff Uncertainties

The results from examples in Chapter 5 are used to verify the analytical solutions. The variability of surface runoff was obtained separately for random hydraulic conductivity, Manning's coefficient and surface elevation Monte Carlo simulations with different levels of input variability. For verification, the standard deviation of water depth along the centerline between downstream and upstream is evaluated.

6.5.1 Comparison of Monte Carlo with Analytical Results for Spatially Variable Hydraulic Conductivity

As stated in chapter 5, random fields of hydraulic conductivity with lognormal standard deviations of 0.5, 0.65, 0.8, 1.1 and 1.5 were chosen for the Monte Carlo simulations. The water depth standard deviations from the Monte Carlo simulations are compared with analytical results obtained using Equation 6-43. In the Monte Carlo simulations, random fields were generated by using the turning bands algorithm. For the spatially variable hydraulic conductivity, the turning bands algorithm generated random fields based on the exponential covariance function with a correlation scale λ , while in

our analytical model the hole-type covariance function of hydraulic conductivity was used. So the correlation parameter of hole-type covariance function, l_c , must be adjusted to fit the exponential function used to generate the data. Gelhar (1993) recommended selecting l_c based on the fit of the functions at the separation for which the correlation for both functions decreases to the e^{-1} level. This requires that $l_c = 2.31 * \lambda$. Figure 6-1 compares the correlation curve from the hole-type function with $l_c = 2.31 * \lambda$ with correlation curves from data generated by the turning bands algorithm and the exponential function. After adjusting the correlation scale, the hole-type function shows good agreement with both exponential function and the data, especially for lag distances less than 4 m. So in our analytical model we use $l_c = 2.31 * 4 \text{ m} = 9.24 \text{ m}$ as an effective correlation scale for the hole type function for spatially variable hydraulic conductivity.

Although the stochastic analytical model assumes steady-state flow in an infinite domain, it is worthwhile to compare the results from the Monte Carlo simulations and the analytical model to evaluate the importance of these assumptions. Figures 6-2 through 6-6 show the standard deviations along the centerline from downstream to upstream obtained from Monte Carlo simulations and the analytical model developed in this study.

For all five cases, the analytical model predicts the Monte Carlo standard deviation well within about 15 m of the downstream boundary but not as accurately for the upstream. This is likely due to the shallow water depth near the upstream boundary which causes the standard deviation prediction from the analytical model using Equation 6-43 to be very high, contrasting to the relatively low standard deviation from the Monte Carlo simulations. Furthermore, the low standard deviations calculated by the Monte Carlo simulations near the upstream boundary may be caused in part by the no flux

boundary conditions imposed there. Nevertheless, the results from the numerical model show the same trend as the results from the Monte Carlo simulations, i.e., as the standard deviation of heterogeneous hydraulic conductivity field increases the prediction uncertainty of surface water depth increases.

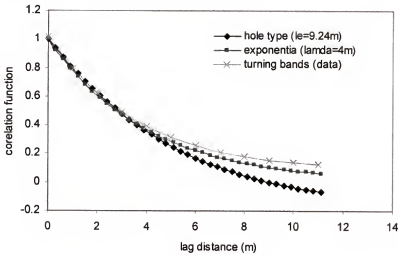


Figure 6-1. Autocorrelation functions of hydraulic conductivity for the exponential function, hole-type function and turning bands algorithm.

Figure 6-7 shows a comparison of standard deviation of water depth versus standard deviation of log hydraulic conductivity for all cases. For the Monte Carlo simulation, the standard deviation of water depth given in this figure is an average value of the standard deviation of water depth for the middle domain, i.e. 10 to 30m. For the analytical solution, the mean water depth required in Equation 6-43 was obtained using geometric mean of hydraulic conductivity. For comparison, the average water depth from the Monte Carlo simulation is also used for the calculation of runoff water depth standard deviation. From Figure 6-7, we can see that results from both approaches are very close and follow the same general trend as the Monte Carlo simulation results. The analytical model, however, overestimates the standard deviation of water depth. It should be noted

that several factors may cause the discrepancy of results between the Monte Carlo simulations and the analytical model. Because of the high non-linearity of the governing equations both for surface and unsaturated flow, it may not be enough to run just 200 Monte Carlo simulations to get the satisfactory statistics of the outputs, especially for random fields with high variability. Furthermore, the analytical model was developed based on a small perturbation assumption, as well as several additional assumptions such as infinite domain, steady state flow, constant mean water depth and decoupled overland and vadose zone flow. All these assumptions have the potential to introduce discrepancies with results from the Monte Carlo simulation.

Figure 6-8 shows a comparison of standard deviations of discharge rate at 900 seconds obtained from Monte Carlo simulations and the analytical model given in Equation 6-51. The analytical model underestimated discharge uncertainty especially for low saturated hydraulic conductivity standard deviation.

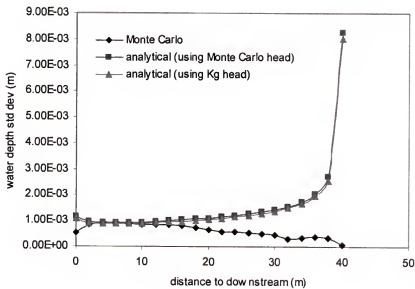


Figure 6-2. Standard deviation of water depth along the centerline between downstream and upstream at 900 sec for a lognormal distributed stationary heterogeneous hydraulic conductivity field with a log standard deviation of 0.5.

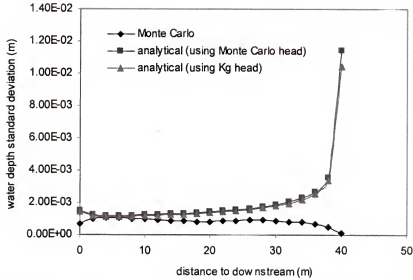


Figure 6-3. Standard deviation of water depth along the centerline between downstream to upstream at 900 sec for a lognormal distributed stationary heterogeneous hydraulic conductivity field with a log standard deviation of 0.65.

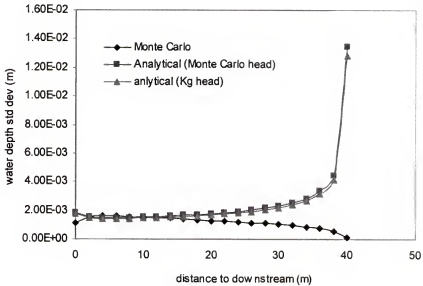


Figure 6-4. Standard deviation of water depth along the centerline between downstream to upstream at 900 sec for a lognormal distributed stationary heterogeneous hydraulic conductivity field with a log standard deviation of 0.8.

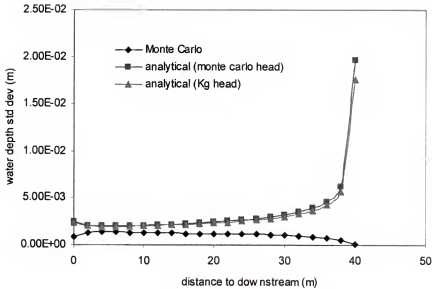


Figure 6-5. Standard deviation of water depth along the centerline between downstream to upstream at 900 sec for a lognormal distributed stationary heterogeneous hydraulic conductivity field with a log standard deviation of 1.1.

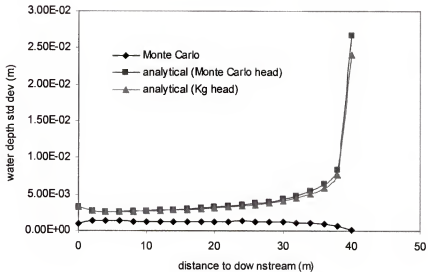


Figure 6-6. Standard deviation of water depth along the centerline between downstream to upstream at 900 sec for a lognormal distributed stationary heterogeneous hydraulic conductivity field with a log standard deviation of 1.5.

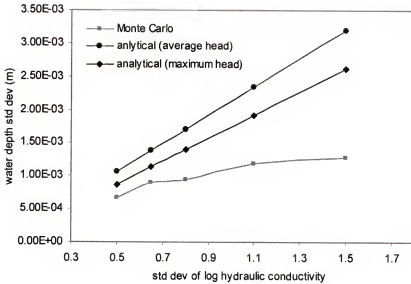


Figure 6-7. Comparison of average standard deviation of water depth versus standard deviation of log hydraulic conductivity at 900 sec between Monte Carlo simulations and analytical model.

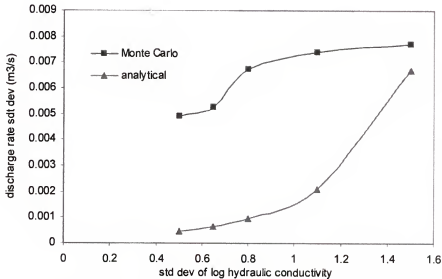


Figure 6-8. Comparison of average standard deviation of discharge rate versus standard deviation of log hydraulic conductivity at 900 sec between Monte Carlo simulations and analytical model.

6.5.2 Comparison of Monte Carlo Results with Analytical Results for Spatially Variable Manning's coefficient

Heterogeneous Manning's coefficient field with lognormal standard deviations of 0.5, 0.65, 0.8, 0.95 and 1.1 were chosen for Monte Carlo simulation. Figures 6-9 to 6-13 compare the standard deviations obtained from Monte Carlo simulations and the analytical model along the centerline from downstream to upstream. For the analytical solution, the average water depths from the Monte Carlo (MC) simulations, using arithmetic mean, and the using effective parameter derived from the analytical model (Equation 6-58) were each used for the calculation of standard deviation of water depth using Equation 6-42.

From Figures 6-9 through 6-13 it is apparent that for all three cases, the analytical model predicts the Monte Carlo results well for the entire domain, especially in the upstream regions. Using the effective Manning's coefficient to determine the mean head gives results very close to the Monte Carlo simulations. Figure 6-14 gives a comparison of the average standard deviation of water depth from the Monte Carlo simulation and the average solution using both the effective parameter derived in Equation 6-58 and the arithmetic mean Manning's coefficient. The average standard deviations of water depth were obtained by averaging the standard deviations of water depth for the center domain from 10 m to 30 m. Again, using the effective parameter in the analytical model gives better results compared with using the arithmetic mean of the Manning's coefficient.

From Figure 6-14, we can see the analytical model slightly overestimates water depth variability for all cases. The reason may be that the Monte Carlo results are based on two-dimensional fields, while our analysis is based on a simplified one-dimensional model. As Gelhar (1993) states "*the higher variance predicted by the one-dimensional*

analysis demonstrates the importance of flow dimensionality when analyzing the effects of heterogeneity.” For one dimensional flow, the flow is forced to pass through high Manning’s coefficient zones, while for two dimensionally heterogeneous medium water is able to move laterally around zones of high Manning’s coefficient. So, in two-dimensional flow, the variability of surface runoff is less than that in one-dimensional flow. The analytical model performs better when using the effective parameter derived from the analytical model as the mean Manning’s coefficient value. When the variability of Manning’s coefficient is low, the analytical model gives satisfactory predictions. When the variability increases, the difference of water depth standard deviation between the Monte Carlo simulations and analytical model increases, as expected, due to the small perturbation assumption.

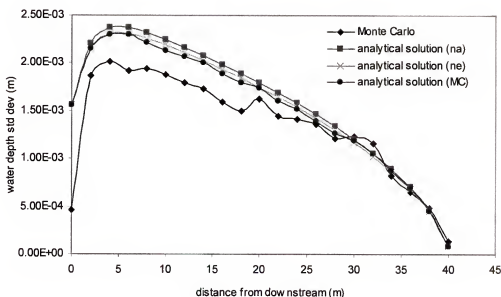


Figure 6-9. Standard deviation of water depth along the centerline between downstream to upstream at 900 sec for a lognormal distributed stationary heterogeneous Manning’s coefficient field with a log standard deviation of 0.5.

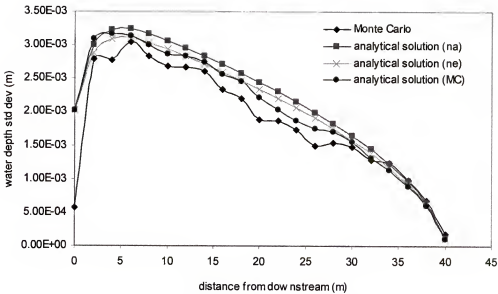


Figure 6-10. Standard deviation of water depth along the centerline between downstream to upstream at 900 sec for a lognormal distributed stationary heterogeneous Manning's coefficient field with a log standard deviation of 0.65.

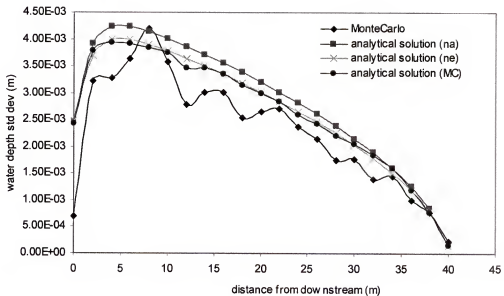


Figure 6-11. Standard deviation of water depth along the centerline between downstream to upstream at 900 sec for a lognormal distributed stationary heterogeneous Manning's coefficient field with a log standard deviation of 0.8.

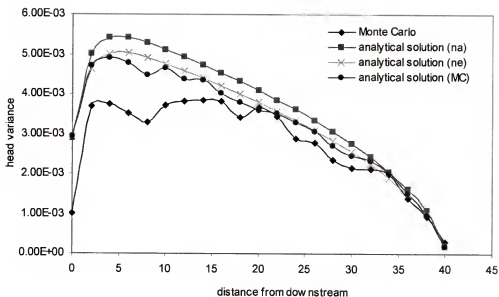


Figure 6-12. Standard deviation of water depth along the centerline between downstream to upstream at 900 sec for a lognormal distributed stationary heterogeneous Manning's coefficient field with a log standard deviation of 0.95.

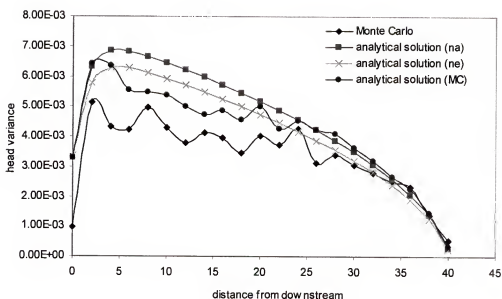


Figure 6-13. Standard deviation of water depth along the centerline between downstream to upstream at 900 sec for a lognormal distributed stationary heterogeneous Manning's coefficient field with a log standard deviation of 1.1.

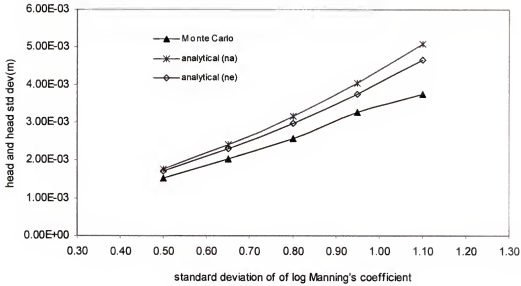


Figure 6-14. Comparison of average standard deviation of water depth versus standard deviation of log Manning's coefficient at 900 sec between Monte Carlo simulations and analytical model using average water depth obtained using the effective and the arithmetic mean Manning's coefficient.

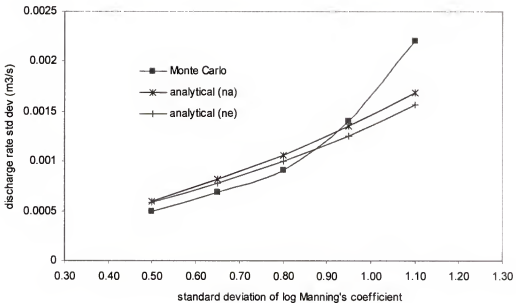


Figure 6-15. Comparison of average standard deviation of discharge rate versus standard deviation of log Manning's coefficient at 900 sec for Monte Carlo simulations and analytical model.

Figure 6-15 shows a comparison of the standard deviation of discharge rate versus standard deviations of log Manning's coefficient at 900 seconds for the Monte Carlo simulations and the analytical model using both the arithmetic mean and effective parameter value of Manning's coefficient to obtain the mean head. Generally speaking, the analytical model gave very good results. For standard deviation of log Manning's coefficient less than 0.9, the analytical model gave results very close to those of the Monte Carlo simulations, although it slightly overestimated the uncertainty of the runoff discharge rate. For standard deviation of log Manning's coefficient greater than 0.9, the analytical model underestimated the uncertainty of runoff discharge rate.

6.5.3 Comparison of Monte Carlo with Analytical Results for Spatially Variable Microtopography

Heterogeneous land surface elevation field with standard deviation of 0.2, 0.3, 0.4 and 0.5 were chosen for the Monte Carlo simulations. Figure 6-16 to Figure 6-19 show the standard deviations obtained from the Monte Carlo simulations and the analytical model for the centerline of the domain from downstream to upstream. For the analytical solution, the mean water depths from the Monte Carlo (MC) simulations and the deterministic result using a uniform slope were used in the calculation of head standard deviation using Equation 6-41. From Figures 6-16 through 6-19 we can see that for all four cases, the analytical model significantly underestimated water depth uncertainty. Figure 6-20 shows the water depth standard deviation versus the surface elevation standard deviation for the Monte Carlo and analytic results. In this figure, the average standard deviations of water depth were obtained by averaging the standard deviation of water depth for the center domain from 10 to 30 m. Again, we can see the analytical model significantly underestimates water depth uncertainty for all cases. As the

variability of the land surface elevation increases, the difference between water depth standard deviations from the Monte Carlo simulations and analytical model increases. The reason may be that our analytical model only considers the first-order effects of land surface variability. According to Horritt (2002), second order effects become important when water depths are small. In our study, the average water depth is about 0.5 cm, comparing to the water depth of more than 1 m in Horritt's study (2002). So second order effects are even more important in our study.

Figure 6-21 shows a comparison of standard deviations of discharge rate at 900 seconds obtained from the Monte Carlo simulations and the analytical model (Equation 6-51) using the Monte Carlo mean head and the mean head obtained from the uniform microtopography. The analytical model significantly overestimates the uncertainty of runoff discharge rate.

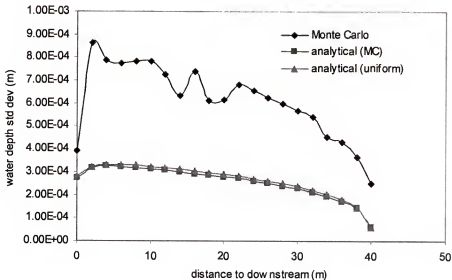


Figure 6-16. Standard deviation of water depth along the centerline between downstream to upstream at 900 sec for a normal distributed stationary microtopography field with a standard deviation of 0.2 cm.

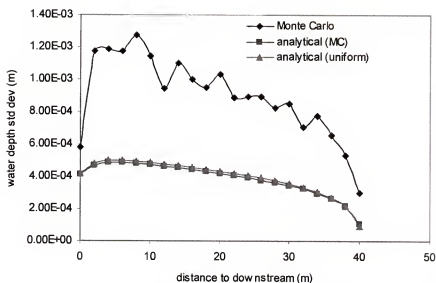


Figure 6-17. Standard deviation of water depth along the centerline between downstream to upstream at 900 sec for a normal distributed stationary microtopography field with a standard deviation of 0.3 cm.

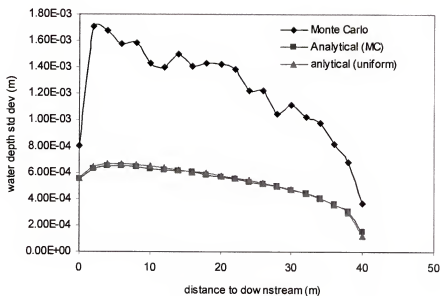


Figure 6-18. Standard deviation of water depth along the centerline between downstream to upstream at 900 sec for a normal distributed stationary microtopography field with a standard deviation of 0.4 cm.

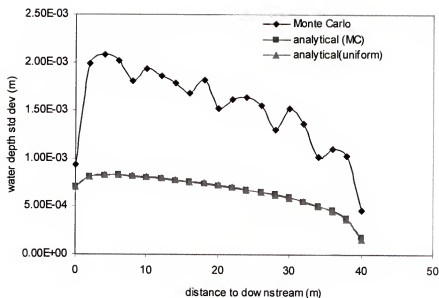


Figure 6-19. Standard deviation of water depth along the centerline between downstream to upstream at 900 sec for a normal distributed stationary microtopography field with a standard deviation of 0.5 cm.

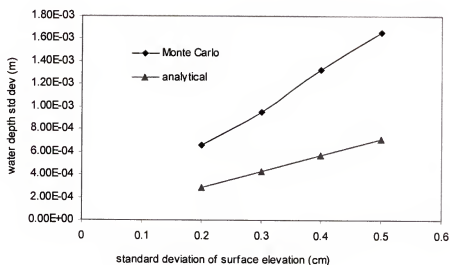


Figure 6-20. Comparison of average standard deviation of water depth at 900 sec between Monte Carlo simulations and analytical model using average water depth for different standard deviation of microtopography.

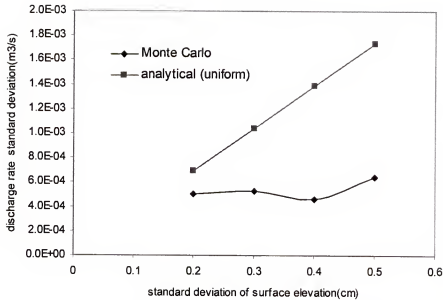


Figure 6-21. Comparison of average standard deviation of discharge rate at 900 sec between Monte Carlo simulations and analytical model versus standard deviation of microtopography.

6.6 Verification of Analytical Model for Effective Parameter Value for Manning's Coefficient

In this section, the ability of the derived effective parameter values of Manning's coefficient to predict the mean runoff hydrograph obtained from the Monte Carlo simulation is evaluated. In addition, the ability of the arithmetic mean, geometric mean, or harmonic mean of the random field to reproduce the mean Monte Carlo runoff hydrograph is examined.

6.6.1 Effective Parameter Value of Manning's coefficient

The mean hydrograph from the Monte Carlo simulations and the hydrographs from uniform fields using the effective parameter (n_e) as well as the arithmetic (n_a), geometric (n_g) and harmonic (n_h) mean respectively as input of Manning's coefficient are plotted in one graph for comparison.

For a lognormal distributed random field with a geometric mean X_g and a variance σ_x^2 , its arithmetic mean X_a and harmonic mean X_h can be expressed as (Gelhar, 1993)

$$X_a = X_g \exp(\sigma_x^2 / 2) \quad (6-57)$$

$$X_h = X_g \exp(-\sigma_x^2 / 2) \quad (6-58)$$

Figures 6-22 through 6-26 show the mean hydrograph from the Monte Carlo simulations and hydrographs obtained from running the deterministic numerical model developed in this study using the arithmetic mean, geometric mean, harmonic mean of Manning's coefficient, and effective Manning's coefficient as input. Each figure shows hydrographs corresponding to one of the five different degrees of variability employed in the Monte Carlo simulations.

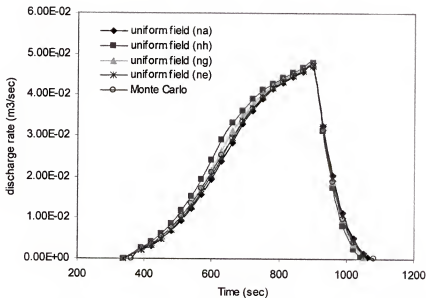


Figure 6-22. Runoff hydrographs from Monte Carlo simulation for a standard deviation of $\log n$ of 0.5 and the deterministic numerical model using the arithmetic mean, harmonic mean, geometric mean and effective parameter value as the Manning's coefficient.

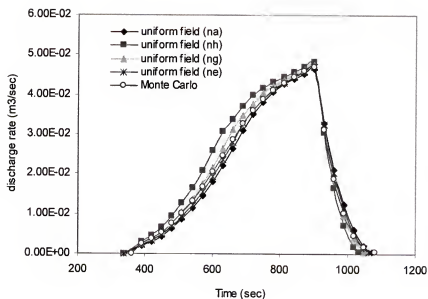


Figure 6-23. Runoff hydrographs from Monte Carlo simulation for a standard deviation of $\log n$ of 0.65 and the deterministic numerical model using the arithmetic mean, harmonic mean, geometric mean and effective parameter value as the Manning's coefficient.

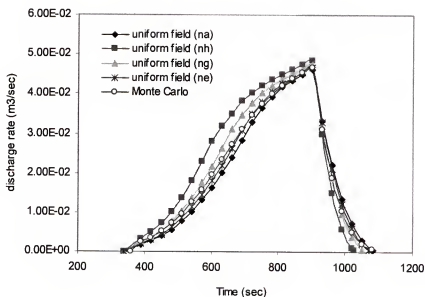


Figure 6-24. Runoff hydrographs from Monte Carlo simulation for a standard deviation of $\log n$ of 0.8 and the deterministic numerical model using the arithmetic mean, harmonic mean, geometric mean and effective parameter value as the Manning's coefficient.

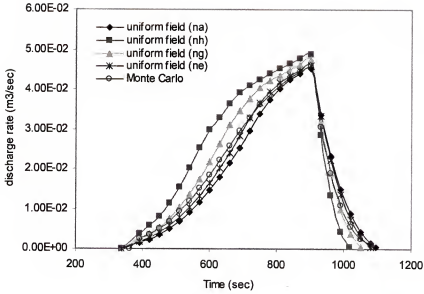


Figure 6-25. Runoff hydrographs from Monte Carlo simulation for a standard deviation of $\log n$ of 0.95 and the deterministic numerical model using the arithmetic mean, harmonic mean, geometric mean and effective parameter value as the Manning's coefficient.

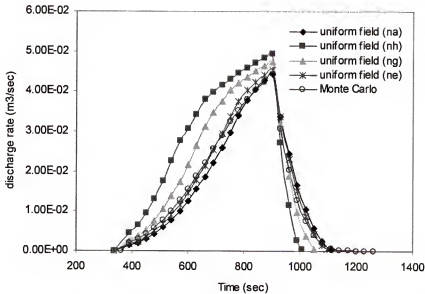


Figure 6-26. Runoff hydrographs from Monte Carlo simulation for a standard deviation of $\log n$ of 1.1 and the deterministic numerical model using the arithmetic mean, harmonic mean, geometric mean and effective parameter value as the Manning's coefficient.

Figures 6-22 through 6-26 show that the effective parameter derived from the analytical model gives very good results. Using the effective parameter derived from the analytical model overestimates surface runoff only when the log standard deviation of Manning's coefficient is close to 1.1. Among arithmetic, geometric and harmonic means, using arithmetic mean gave the best results. Using the geometric or harmonic mean as input for uniform field overestimated surface runoff especially for high variability of Manning's coefficient. While using arithmetic mean as input for the uniform field slightly underestimated surface runoff.

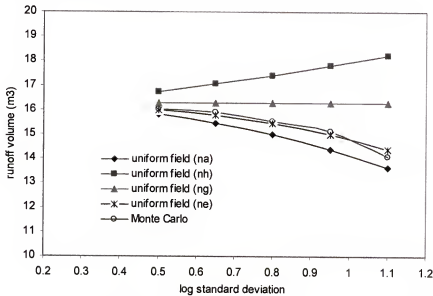


Figure 6-27. Runoff volumes obtained from Monte Carlo simulations and the deterministic numerical model using the arithmetic mean, harmonic mean, geometric mean and effective parameter value as the Manning's coefficient for spatially variable Manning's coefficient.

Figure 6-27 gives the mean total runoff volume (which is the area under the mean hydrograph) versus log standard deviation of Manning's coefficient for the Monte Carlo simulation and the deterministic model using the arithmetic, harmonic, geometric means

and the effective Manning's coefficient. Similar conclusions can be drawn by comparing the total runoff volume from different approaches. The effective parameter predicts the decrease in runoff volume with increasing variability of the Manning's coefficient very accurately.

6.6.2 Effective Parameter Value of Hydraulic Conductivity

For hydraulic conductivity, the correction factor determined from Equation 6-72 is very small because of small surface water depth, so no attempt was made to evaluate effective parameter value based on Equation 6-72. However the runoff hydrographs obtained from the arithmetic mean, geometric mean and harmonic mean were compared to the mean runoff hydrograph obtained from the Monte Carlo simulations (see Figures 6-28 through 6-32). It is obvious that taking arithmetic or harmonic mean as the effective hydraulic conductivity of the heterogeneous field leads to underestimation or overestimation of surface runoff peak and volume, respectively. The geometric mean gives more acceptable results, although it is not particularly accurate. Generally speaking, using the geometric mean hydraulic conductivity as the effective parameter underestimates surface runoff volume and overestimates runoff peak.

Figure 6-33 gives a comparison of the total runoff volume for all cases. When the standard deviation of heterogeneous field is as high as 1.5, using the arithmetic mean as the average hydraulic conductivity generates no runoff because the arithmetic mean is so high that all rainfall infiltrates into subsurface. Our numerical experiments show that no single effective parameter exists that will reproduce or well approximate the average hydrograph obtained from the Monte Carlo simulations, however, use of the geometric mean gave more accurate results than use of the arithmetic or harmonic mean of hydraulic conductivity.

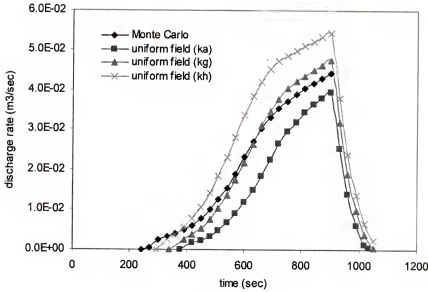


Figure 6-28. Runoff hydrographs from Monte Carlo simulations for a standard deviation of $\log k$ of 0.5 and the deterministic numerical model using the arithmetic mean, harmonic mean, and geometric mean as the hydraulic conductivity.

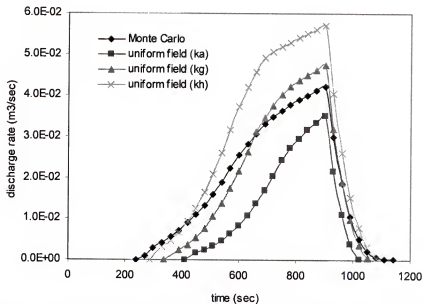


Figure 6-29. Runoff hydrographs from Monte Carlo simulations for a standard deviation of $\log k$ of 0.65 and the deterministic numerical model using the arithmetic mean, harmonic mean, and geometric mean as the hydraulic conductivity.

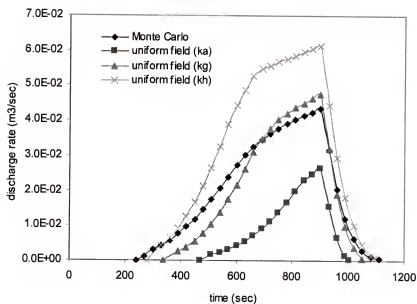


Figure 6-30. Runoff hydrographs from Monte Carlo simulations for a standard deviation of $\log k$ of 0.8 and the deterministic numerical model using the arithmetic mean, harmonic mean, and geometric mean as the hydraulic conductivity.

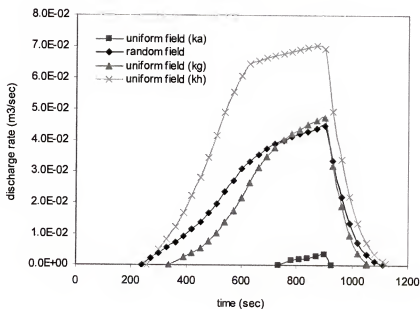


Figure 6-31. Runoff hydrographs from Monte Carlo simulations for a standard deviation of $\log k$ of 1.1 and the deterministic numerical model using the arithmetic mean, harmonic mean, and geometric mean as the hydraulic conductivity.

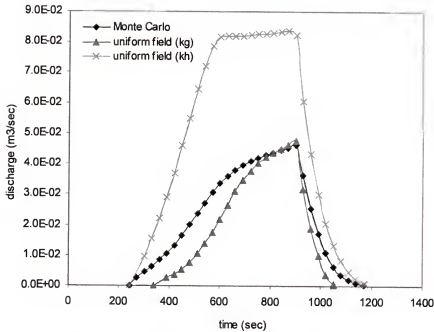


Figure 6-32. Runoff hydrographs from Monte Carlo simulations for a standard deviation of $\log k$ of 1.5 and the deterministic numerical model using the arithmetic mean, harmonic mean, and geometric mean as the hydraulic conductivity.

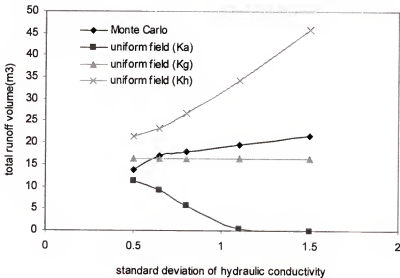


Figure 6-33. Runoff volumes obtained from Monte Carlo simulations and the deterministic numerical model using the arithmetic mean, harmonic mean, and geometric mean as the hydraulic conductivity.

6.7 Conclusions

In this chapter, a 1-D stochastic analytical model based on first-order perturbation techniques was developed. The model can be used to predict the runoff water depth and discharge rate standard deviation resulting from uncertainties in saturated hydraulic conductivity, Manning's coefficient and microtopography. The analytical model was developed after introducing steady-state, infinite domain, and constant water depth assumptions so caution should be exercised when applying the model to areas of the domain close to boundaries and during extremely transient situations. From this analytical model, the effective parameter values of hydraulic conductivity, Manning's coefficient and surface elevation were derived. Several examples were used to test the analytical model.

The analytical model accurately predicted the runoff water depth uncertainty resulting from the uncertainty of Manning's coefficient, although it slightly overestimated the water depth uncertainty compared with Monte Carlo simulations. From the analytical model, the water depth standard deviation due to the spatially heterogeneous Manning's coefficient field is proportional to water depth and the standard deviation of the Manning's coefficient field. As runoff water depth increases, the prediction uncertainty for water depth increases, thus the discrepancy between the analytical model and the Monte Carlo simulation is significant for areas close to the downstream boundary and small for areas close to the upstream boundary.

The effective parameter value for Manning's coefficient developed from the analytical model is only a function of the variance of log Manning's coefficient and the geometric mean of Manning's coefficient so it is very convenient to use. The effective parameter of Manning's coefficient gave satisfactory results when it was used to predict

the runoff water depth standard deviation, mean runoff hydrograph and mean runoff volume.

The analytical model reasonably predicted the water depth standard deviation for a heterogeneous hydraulic conductivity field. However, it overestimated the surface water depth uncertainty. From the analytical model, the water depth standard deviation due to the spatially variable hydraulic conductivity is proportional to the correlation scale, geometric mean and the standard deviation of the hydraulic conductivity, and inversely proportional to the mean runoff water depth and the square root of the mean surface slope. The dependence on mean water depth explains why the difference in the water depth standard deviation between the analytical model and the Monte Carlo simulation is large for areas close to the upstream boundary and small for areas close to the downstream boundary.

The effective parameter value for hydraulic conductivity is a function of water depth, so it is also a function of time. This means that no single value is available for effective hydraulic conductivity for the transient problem. Based on the expression of effective parameter of hydraulic conductivity derived in this study, the correction to the geometric mean hydraulic conductivity is small when the water depth is very shallow. Thus, the geometric mean may be the best effective parameter value for this case. After comparing the hydrographs from approaches using the geometric mean, arithmetic mean and harmonic mean as the uniform equivalent hydraulic conductivity, we conclude that geometric mean is the best one among them. Although we may find a better single effective parameter value that produces a surface runoff volume closer to that produced by Monte Carlo simulation, the shape of the hydrograph obtained using this effective

parameter value, however, will be quite different from the mean hydrograph from Monte Carlo simulations.

The analytical model significantly underestimates the runoff standard deviation resulting from a heterogeneous surface elevation field. From the analytical model, the water depth standard deviation due to the spatially variable microtopography is approximately inversely proportional to the correlation scale and mean of the surface slope, and is approximately proportional to mean water depth and the standard deviation of microtopography. Thus, the difference in the standard deviation of water depth predicted by the analytical model and the Monte Carlo simulation is large in the center of the domain and small for the areas close to the upstream and downstream boundaries.

The effective parameter value for surface slope is inversely proportional to surface slope. The correction to the mean surface slope increases with the variance of microtopography, and decreases with the mean surface slope and correlation scale of random microtopography field. Unfortunately, the correction to surface slope is very small for the Monte Carlo simulations conducted in this research so Equation 6-67 could not be validated.

CHAPTER 7

SUMMARY AND CONCLUSIONS

In this study, a model was developed to couple evapotranspiration, overland flow and unsaturated subsurface flow. The 1-D Richards' equation was selected for solving unsaturated flow using a finite element method. Evaporation and transpiration were modeled as a specified flux boundary and internal sink respectively within the unsaturated soil moisture flow model. The unsaturated flow model was tested against several examples taken from the literature. The model can use potential evapotranspiration saved in an input file or calculate it using the Penman-Monteith equation. The actual evaporation and transpiration are calculated by introducing a reduction coefficient, which can be determined using several methods. The model can use average daily evapotranspiration or evapotranspiration with a diurnal cycle.

A 2-D diffusion wave model of overland flow derived from the Saint Venant equations was selected to simulate surface flow, and was solved by a finite element method. Several examples taken from the literature were used to test the overland flow model. The overland flow model was coupled with the unsaturated subsurface model by a common boundary---the ground surface, and the coupling parameter was water flux at the interface. The coupled model was tested against the field study by Jacobs et al. (2002) for comparison of actual evapotranspiration, water table depth and soil moisture content. It was also tested against the experimental data by Smith and Woolhiser (1971) and numerical results by Akan and Yen (1981) and Singh and Bhallamudi (1998) for the comparison of the surface runoff hydrograph resulting from the interactive process of

overland flow and vadose zone flow. The various examples given in Chapters 1, 3 and 4 for the verification of both the coupled model and its several components established the reliability of the coupled model predictions. Thus, it was used for the stochastic analysis of surface runoff.

Using the coupled numerical model, Monte Carlo simulations were conducted to study the prediction uncertainties in surface discharge rate and surface water depth produced by undetermined spatial variability in Manning's coefficient, surface elevation and soil saturated hydraulic conductivity. Results show that as time increases, the coefficient of variation of surface water depth increases when Manning's coefficient is spatially variable. For spatially variable microtopography and random hydraulic conductivity, the coefficient of variation of water depth decreases significantly as time increases. Thus spatially variable microtopography and hydraulic conductivity have a greater effect on water depth prediction uncertainty at early times and Manning's coefficient has a slightly greater effect at later times. Regarding mean peak discharge and mean total runoff volume, the random hydraulic conductivity field produced the largest deviation from deterministic results obtained using a uniform field.

A 1-D stochastic analytical model based on first-order perturbation techniques was developed and tested against the results obtained from the Monte Carlo simulations. The analytical model was used to predict the runoff water depth and discharge rate uncertainties resulting from uncertainties in saturated hydraulic conductivity, Manning's coefficient and microtopography. The analytical model gave results very similar to the Monte Carlo simulation results when applied to predict the uncertainties of runoff water depth and runoff discharge rate resulting from the uncertainty of Manning's coefficient.

The analytical model gave reasonable predictions of water depth and runoff rate standard deviations from a heterogeneous hydraulic conductivity field, especially for low degree of variability of hydraulic conductivity. As expected, when the degree of variability of hydraulic conductivity increases, the discrepancy between results from the analytical model and Monte Carlo simulations increases. The analytical model significantly underestimates the runoff variability resulting from the heterogeneous surface elevation field probably because the effects of higher-order perturbations were not considered in developing the analytical model. In Horritt's study (2002), the higher-order perturbations resulted in an increase in both the mean water depth and its standard deviation.

The effective parameter values of Manning's coefficient, surface slope and hydraulic conductivity for random fields were derived from the analytical stochastic model. The effective parameter value of Manning's coefficient gave satisfactory results when it was used to predict the runoff water depth uncertainty, the mean hydrograph and the mean runoff volume. Based on the expression derived for the effective hydraulic conductivity and surface elevation, the corrections to hydraulic conductivity and surface slope are small when the surface water depth is very shallow, as was the case for the Monte Carlo simulation example. Thus no attempt was made to test the effective parameter values of hydraulic conductivity and surface elevation.

Based on the findings of current study, the following recommendations for future research are suggested.

Monte Carlo simulations which use conventional Monte Carlo sampling methods (MCS) are very computationally intensive. Computational demands may be reduced if a more efficient sampling technique such as a Latin Hypercube Sample (LHS) algorithm is

used. LHS is a stratified sampling technique where the random variable distributions are divided into equal probability intervals. A probability is randomly selected from within each interval for each basic event. LHS is generally more precise for producing a representative ensemble of random samples than conventional Monte Carlo sampling, because the full range of the distribution is sampled more evenly and consistently. Thus, with LHS, a smaller number of realizations can achieve the same accuracy as a larger number of Monte Carlo trials.

In this research, a 1-D stochastic analytical model was developed and tested against a 2-D Monte Carlo model. The performance of the analytical model should improve if it is extended to two dimensions. Also, the analytical model was developed for a steady state overland flow condition. It may be worthwhile to develop a transient analytical model so that the impact of spatial heterogeneity on the runoff hydrograph can be predicted analytically.

APPENDIX A
DERIVATION OF MATRICES A , B AND F

For two-node linear elements, the shape functions are expressed as

$$\begin{aligned} N_1^{(e)}(x) &= \frac{x_2 - x}{x_2 - x_1} \\ N_2^{(e)}(x) &= \frac{x - x_1}{x_2 - x_1} \end{aligned} \quad (\text{A-1})$$

A.1 For Moisture-Content Based Governing Equation

Plugging Equation A-1 into A_U of Equation 1-21 renders

$$\begin{aligned} A_{11}^{(e)} &= \int_{x_1}^{x_2} N_1 N_1 dx = \frac{L_e}{3} \\ A_{12}^{(e)} &= \int_{x_1}^{x_2} N_1 N_2 dx = \frac{L_e}{6} \\ A_{21}^{(e)} &= A_{12}^{(e)} = \frac{L_e}{6} \\ A_{22}^{(e)} &= \int_{x_1}^{x_2} N_2 N_2 dx = \frac{L_e}{3} \end{aligned} \quad (\text{A.2})$$

where $L_e = x_2 - x_1$, is the length of the element.

So matrix A can be written as

$$A^{(e)} = \begin{bmatrix} \frac{L_e}{3} & \frac{L_e}{6} \\ \frac{L_e}{6} & \frac{L_e}{3} \end{bmatrix} = \frac{L_e}{6} \begin{bmatrix} 2 & 1 \\ 1 & 2 \end{bmatrix} \quad (\text{A-3})$$

Considering the B_U term in Equation 1-22. We approximate \hat{D} as

$$\hat{D}(x, t) = N_j(x) D_j(t) = D_1 \frac{x_2 - x}{x_2 - x_1} + D_2 \frac{x - x_1}{x_2 - x_1} \quad (\text{A-4})$$

$$B^{(e)}_{11} = \int_{x_1}^{\hat{x}} \bar{D} \frac{\partial N_1}{\partial x} \frac{\partial N_1}{\partial x} dx = \frac{D_1 + D_2}{2L_e} = \frac{\bar{D}}{2L_e} \quad (\text{A.5})$$

$$\text{Here } \bar{D} = \frac{D_1 + D_2}{2}$$

Similarly we get:

$$\begin{aligned} B^{(e)}_{12} &= -\frac{\bar{D}}{2L_e} \\ B^{(e)}_{21} &= B^{(e)}_{12} = -\frac{\bar{D}}{2L_e} \\ B^{(e)}_{22} &= \frac{\bar{D}}{2L_e} \end{aligned} \quad (\text{A.6})$$

So matrix B can be written as

$$B^{(e)} = \begin{bmatrix} \frac{\bar{D}}{2L_e} & \frac{\bar{D}}{2L_e} \\ \frac{\bar{D}}{2L_e} & \frac{\bar{D}}{2L_e} \end{bmatrix} = \frac{\bar{D}}{2L_e} \begin{bmatrix} 1 & -1 \\ -1 & 1 \end{bmatrix} \quad (\text{A-7})$$

The load vector F_I is determined in a similar procedure:

$$F^{(e)}_I = \int_{x_1}^{x_2} K \hat{k}_r \frac{\partial N_I}{\partial x} \frac{\partial z}{\partial x} dx + \left[N_I \left(\hat{D} \frac{\partial \theta}{\partial x} + K \hat{k}_r \frac{\partial z}{\partial x} \right) \right]_{x_1}^{x_2} + \int_{x_1}^{x_2} N_I Q dx \quad (\text{A-8})$$

$$k_r(x, t) = N_J(x) k_J(t) = k_1 \frac{x_2 - x}{x_2 - x_1} + k_2 \frac{x - x_1}{x_2 - x_1} \quad (\text{A-9})$$

$$\begin{aligned} F^{(e)}_1 &= \int_{x_1}^{x_2} K \hat{k}_r \frac{\partial N_1}{\partial x} \frac{\partial z}{\partial x} dx + \left[N_1 \left(K_{\theta} \hat{k}_r \frac{\partial \psi}{\partial x_j} + K \hat{k}_r \frac{\partial z}{\partial x} \right) \right]_{x_1}^{x_2} + \int_{x_1}^{x_2} N_1 Q dx \\ &= -K \frac{k_{r1} + k_{r2}}{2} + \frac{QL_e}{2} + q_{in}(x_1) \end{aligned} \quad (\text{A-10})$$

Here $q_{in}(x_1)$ is the flux at node 1.

F_2 can be calculated in the same way,

$$\begin{aligned} F^{(e)}_2 &= \int_{x_1}^{x_2} K \hat{k}_r \frac{\partial N_2}{\partial x} \frac{\partial z}{\partial x} dx + \left[N_2 (K_{yy} k_r \frac{\partial \psi}{\partial x_j} + K \hat{k}_r \frac{\partial z}{\partial x}) \right]_{x_1}^{x_2} + \int_{x_1}^{x_2} N_2 Q dx \\ &= K \frac{k_{r1} + k_{r2}}{2} + \frac{QL_e}{2} + q_{in}(x_2) \end{aligned} \quad (A-11)$$

A.2 For Pressure Based Governing Equation

Approximating $\hat{\eta}(x, t)$ by following equation:

$$\hat{\eta}(x, t) = N_J(x) \eta_J(t) = \eta_1 \frac{x_2 - x}{x_2 - x_1} + \eta_2 \frac{x - x_1}{x_2 - x_1} \quad (A-12)$$

Substituting Equations A-1 and A-12 into A_{IJ} of Equation 1-31 we get

$$A^{(e)}_{11} = \int_{x_1}^{x_2} \hat{\eta} N_1 N_1 dx = \frac{L_e}{12} (3\eta_1 + \eta_2) \quad (A-13)$$

where $L_e = x_2 - x_1$

$$\begin{aligned} A^{(e)}_{12} &= \int_{x_1}^{x_2} \hat{\eta} N_1 N_2 dx = \frac{L_e}{12} (\eta_1 + \eta_2) \\ A^{(e)}_{22} &= \int_{x_1}^{x_2} \hat{\eta} N_2 N_2 dx = \frac{L_e}{12} (\eta_1 + 3\eta_2) \\ A^{(e)}_{21} &= A^{(e)}_{12} = \frac{L_e}{12} (\eta_1 + \eta_2) \end{aligned} \quad (A-14)$$

So we have

$$A^{(e)} = \frac{L_e}{12} \begin{bmatrix} 3\eta_1 + \eta_2 & \eta_1 + \eta_2 \\ \eta_1 + \eta_2 & \eta_1 + 3\eta_2 \end{bmatrix} \quad (A-15)$$

Now consider the B_{IJ} term in Equation 1-32,

$$B^{(e)}_{11} = \int_{x_1}^{x_2} K k_r \frac{\partial N_1}{\partial x} \frac{\partial N_1}{\partial x} dx = \frac{K_1 + K_2}{2L_e} = \frac{\bar{K}}{2L_e} \quad (A-16)$$

Here $\bar{K} = \frac{K_1 + K_2}{2}$, and $K_1 = K k_r|_{x=x_1}$, $K_2 = K k_r|_{x=x_2}$

Similarly we get:

$$\begin{aligned}
 B^{(e)}_{12} &= -\frac{\bar{K}}{2L_e} \\
 B^{(e)}_{21} &= B^{(e)}_{12} = -\frac{\bar{K}}{2L_e} \\
 B^{(e)}_{22} &= \frac{\bar{K}}{2L_e}
 \end{aligned} \tag{A-17}$$

So matrix B can be written as,

$$B^{(e)} = \begin{bmatrix} \frac{\bar{K}}{2L_e} & \frac{\bar{K}}{2L_e} \\ \frac{\bar{K}}{2L_e} & \frac{\bar{K}}{2L_e} \end{bmatrix} = \frac{\bar{K}}{2L_e} \begin{bmatrix} 1 & -1 \\ -1 & 1 \end{bmatrix} \tag{A-18}$$

APPENDIX B ROOT DENSITY DISTRIBUTION FUNCTIONS AND SOIL MOISTURE RESTRICTION FACTOR

B.1 Root Density Distribution Functions

If $L_d(z)$ is the root length density ($L L^{-3}$), then the root density distribution function can be expressed as:

$$g(z) = \frac{L_d(z)}{\int_0^{L_r} L_d(z) dz} \quad (B-1)$$

where $g(z)$ is the root density distribution function (L^{-1}); L_r is the total root depth (L); L_d is the root length density ($L L^{-3}$).

If $L_d(z) = (1-c)L_r + 2cz$, then the root density distribution function is

$$g(z) = \frac{c(2z - L_r) + L_r}{L_r^2}, \quad -1 \leq c \leq 1, \quad |z| \leq L_r \quad (B-2)$$

where c is the constant depending on the plant and its vegetative stage (-); z is the current root depth (L); L_r is the total root depth (L).

The root density distribution function was used by Hoogland et al. (1981) and Perrochet (1987).

A logarithmic root density distribution model used by Jackson et al. (1996) and Dogan (1999) can be obtained by setting $L_d(z) = c^z$.

$$g(z) = \frac{c^z \ln(c)}{c^{L_r} - 1} \quad 0.1 \leq c < 1, \quad |z| \leq L_r \quad (B-3)$$

The root density distribution model used in this study can be obtained by setting

$L_d(z) = e^{-cz} - e^{-cL_r}$, after substituting it to Equation B-1, we get

$$g(z) = \frac{c(e^{-cz} - e^{-cL_r})}{1 - (1 + cL_r)e^{-cL_r}} \quad 0 < c \leq 1, \quad |z| \leq L_r \quad (\text{B-4})$$

This new expression is easy to fit because only one parameter(c) needs to be determined.

B.2 Soil Moisture Restriction Factor

Feddes et al. (1978) proposed the following method to calculate soil moisture restriction factor:

$$\alpha(\psi) = \begin{cases} 1 & \psi_1 \leq \psi \leq 0 \\ 1 - \frac{\psi - \psi_1}{\psi_2 - \psi_1} & \psi_2 \leq \psi \leq \psi_1 \\ 0 & -\infty \leq \psi \leq \psi_2 \end{cases} \quad (\text{B-5})$$

where ψ is the soil suction around the roots at a given depth (L); ψ_1 is the minimum soil suction at which roots have potential transpiration rate (L); ψ_2 is the soil suction around the roots from which the transpiration diminishes to zero (L).

Kristensen and Jensen (1975) proposed a soil moisture restriction reduction function as:

$$\alpha(\psi) = 1 - \left(\frac{\psi_{fc} - \psi}{\psi_{fc} - \psi_{wp}} \right)^{\frac{c_3}{T_p}} \quad (\text{B-6})$$

where ψ_{fc} is the pressure head at field capacity of soil (L); ψ_{wp} is the pressure head at wilting point of soil (L); c_3 is the shape parameter ($\geq T_p$) (L), which defines the shape of the water stress function; and T_p is the potential transpiration rate (L).

APPENDIX C CALCULATIONS OF MATRICES FOR GALERKIN FEM APPROACH

Given a triangular element and linear interpolation functions, the procedures for calculating matrix A_{IJ} , B_{IJ} , and F_I are listed in following.

$$A_{IJ}^e = \int_{\Omega^e} N_I N_J d\Omega \quad (C-1)$$

The integrals of this form are readily evaluated using the following convenient relation.

$$\int_{\Omega^e} L_1^a L_2^b L_3^c d\Omega = 2\Delta^e a!b!c!/(a+b+c+2)! \quad (C-2)$$

where L_1, L_2, L_3 is the local coordinates of a triangle expressed in area proportion(-); a, b and c are integration constants; Δ^e is the area of triangular element(L^2).

L_1, L_2, L_3 are calculated by

$$L_1 = A_1 / \Delta^e, \quad L_2 = A_2 / \Delta^e, \quad L_3 = A_3 / \Delta^e \quad (C-3)$$

where Δ^e is the total area of the triangle and A_i ($i=1,2,3$) denotes the areas of the subtriangle i . Because the sum of A_1, A_2 , and A_3 must equal Δ^e , it follows that

$$L_1 + L_2 + L_3 = 1 \quad (C-4)$$

It is easy to know that $N_1 = L_1, N_2 = L_2, N_3 = L_3$.

$$A_{11}^e = \int_{\Omega^e} N_1 N_1 d\Omega = \int_{\Omega^e} L_1^2 d\Omega = \frac{2\Delta^e \times 2!}{(2+0+0+2)!} = \frac{\Delta^e}{6}$$

$$A_{12}^e = \int_{\Omega^e} N_1 N_2 d\Omega = \int_{\Omega^e} L_1 L_2 d\Omega = \frac{2\Delta^e}{(1+1+0+2)!} = \frac{\Delta^e}{12}$$

$$A_{13}^e = \int_{\Omega^e} N_1 N_3 d\Omega = \int_{\Omega^e} L_1 L_3 d\Omega = \frac{2\Delta^e}{(1+0+1+2)!} = \frac{\Delta^e}{12}$$

Following the same procedures, other elements in Matrix A can be calculated. In Matrix for A is written as

$$A^e = \frac{\Delta^e}{12} \begin{vmatrix} 2 & 1 & 1 \\ 1 & 2 & 1 \\ 1 & 1 & 2 \end{vmatrix} \quad (C-5)$$

B_{IJ}^e is calculated by Equation C-6

$$B_{IJ}^e = \int_{\Omega^e} K_I K_J \frac{\partial N_I}{\partial x_i} \frac{\partial N_J}{\partial x_j} d\Omega, \quad (C-6)$$

In calculating B_{IJ}^e , we assume

$$K_{11} = k_x, \quad K_{22} = k_y \quad \text{and} \quad K_{12} = K_{21} = 0$$

We also assume k_x and k_y within any point of the triangle can be approximated as

$$\begin{aligned} K_x &= K_{x,1}N_1 + K_{x,2}N_2 + K_{x,3}N_3 \\ K_y &= K_{y,1}N_1 + K_{y,2}N_2 + K_{y,3}N_3 \end{aligned} \quad (C-7)$$

The shape functions in Equation C-7 can be expressed as

$$N_I = \frac{1}{2\Delta^e} (\alpha_I + \beta_I x + \gamma_I y) \quad I=1,2,3 \quad (C-8)$$

$$\text{So} \quad \partial N_I / \partial x = \beta_I / 2\Delta^e, \quad \partial N_I / \partial y = \gamma_I / 2\Delta^e,$$

$$B_{IJ}^e = \int_{\Omega^e} \left(K_x \frac{\partial N_I}{\partial x} \frac{\partial N_J}{\partial x} + K_y \frac{\partial N_I}{\partial y} \frac{\partial N_J}{\partial y} \right) d\Omega = \frac{1}{4\Delta^{e^2}} \int_{\Omega^e} (K_x \beta_I \beta_J + K_y \gamma_I \gamma_J) d\Omega$$

The first part of B_{IJ}^e is calculated:

$$\begin{aligned} \int_{\Omega^e} (K_x \beta_I \beta_J) d\Omega &= \beta_I \beta_J \int_{\Omega^e} (K_{x,1}N_1 + K_{x,2}N_2 + K_{x,3}N_3) d\Omega \\ &= \beta_I \beta_J \left(K_{x,1} \frac{2\Delta^e}{3!} + K_{x,2} \frac{2\Delta^e}{3!} + K_{x,3} \frac{2\Delta^e}{3!} \right) = \Delta^e \bar{k}_x \beta_I \beta_J \end{aligned}$$

Where $\bar{k}_x = (K_{x,1} + K_{x,2} + K_{x,3})/3$

The second part of B_{ij}^e can be calculated using a similar procedure,

$$\int_{\Omega^e} (K_y \gamma_i \gamma_j) d\Omega = \Delta^e \bar{k}_y \gamma_i \gamma_j$$

where $\bar{k}_y = (K_{y,1} + K_{y,2} + K_{y,3})/3$

Therefore B_{ij}^e can be written as

$$B_{ij}^e = \frac{1}{4\Delta^e} (\Delta^e \bar{k}_x \beta_i \beta_j + \Delta^e \bar{k}_y \gamma_i \gamma_j) = \frac{1}{4\Delta^e} (\bar{k}_x \beta_i \beta_j + \bar{k}_y \gamma_i \gamma_j)$$

Matrix F is calculated part by part

$$F_i = \sum_e \left(- \int_{\Gamma_N} N_i K_y \frac{\partial H}{\partial x_j} n_i d\Gamma - \int_{\Omega^e} N_i Q d\Omega \right) \quad (C-9)$$

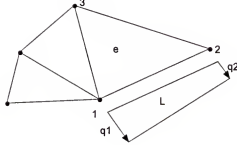


Figure C-1 Evaluation of the flux term across the exterior element boundary.

To calculate the first part of F, it is assumed that in Figure C-1 that nodes 1 and 2 lie on Γ_N^e , Then the integration along this edge can be evaluated as

$$\int_{\Gamma_N} N_i q d\Gamma = \int_0^L N_i q dS \quad (C-10)$$

Where L is the length of edge 12, S is local coordinate.

Now along the coordinate S, the linear functions q and N1 are given by

$$q = q_1 + \frac{S}{L}(q_2 - q_1) \quad N_1 = 1 - \frac{S}{L} \quad N_2 = \frac{S}{L} \quad (\text{C-11})$$

Substitution Equation C-11 to Equation C-12 yields,

$$\int_{\Gamma_N} N_1 q d\Gamma = \int_0^L \left[q_1 + \frac{S}{L}(q_2 - q_1) \right] \left[1 - \frac{S}{L} \right] dS = \frac{L}{2} \left(q_1 + \frac{q_2 - q_1}{3} \right) = \frac{(2q_1 + q_2)L}{6} \quad (\text{C-12})$$

Similarly, it can be shown that

$$\int_{\Gamma_N} N_2 q d\Gamma = \frac{L}{2} \left(q_2 + \frac{q_1 - q_2}{3} \right) = \frac{(q_1 + 2q_2)L}{6}, \quad \text{and}$$

$$\int_{\Gamma_N} N_3 q d\Gamma = 0$$

The second part is obtained as follows,

$$F_{i,2} = \int_{\Omega^e} N_i Q d\Omega = \frac{\Delta^e Q}{3} \quad (\text{C-13})$$

APPENDIX D
DERIVING THE AUTOCOVARIANCE OF WATER DEPTH, AND THE
CROSSCOVARIANCE FUNCTION BETWEEN SURFACE SLOPE AND WATER
DEPTH RESULTING FROM RANDOM VARIABLE SURFACE SLOPE

Instead of expressing $S_{fx}^{1/2}$ in the derivative of z in space, it is expanded in Taylor series directly and used in developing $P_{sh}(\zeta)$ and $P_{hh}(\zeta)$.

For Expanding $S_{fx}^{1/2}$ in Taylor series,

$$S_{fx}^{1/2} = S_0^{1/2} + \frac{1}{2} S_0^{-1/2} = \sqrt{S_0} \left(1 + \frac{1}{2S_0} \right) \quad (D-1)$$

Substituting Equations 6-9, 6-12 and D-1 into Equation 6-5 and assuming steady state condition, then we have,

$$\frac{\partial}{\partial x_i} \left(n_g^{-1} (1 - n'_i) \left(\bar{h}^{5/3} + \frac{5}{3} \bar{h}^{2/3} h' \right) \left(\sqrt{S_0} + \frac{1}{2\sqrt{S_0}} S' \right) \right) = -K_g (1 + K'_i) \quad (D-2)$$

Collecting perturbation terms respectively and neglecting second order terms,

$$\frac{\partial}{\partial x_i} \left(\frac{\bar{h}^{5/3}}{2n_g \sqrt{S_0}} S' + \frac{5\sqrt{S_0} \bar{h}^{2/3}}{3n_g} h' - \frac{\sqrt{S_0} \bar{h}^{5/3}}{n_g} n'_i \right) = -K_g K'_i \quad (D-3)$$

Pre-multiplying Equation D-3 by surface slope perturbation $S'(x')$, bring this perturbation inside derivatives with respect to x , assuming that surface slope, Manning's coefficient and saturated hydraulic conductivity are not related with each other and taking the expected value gives the governing equation for $P_{sh}(x', x)$, which is the cross-covariance of surface slope and water depth,

$$\frac{\partial}{\partial x_i} \left(-\frac{\bar{h}^{5/3}}{2n_g \sqrt{S_0}} P_{ss}(x', x) + \frac{5\sqrt{S_0} \bar{h}^{2/3}}{3n_g} P_{sh}(x', x) \right) = 0 \quad (D-4)$$

where $P_{ss}(x', x)$ is the auto-covariance of surface slope; $P_{sh}(x', x)$ is the cross-covariance of surface slope and water depth.

From Equation D-4 we have

$$P_{sh}(x', x) = -\frac{3\bar{h}}{10S_0} P_{ss}(x', x) \quad (D-5)$$

Post-multiplying Equation D-3 expressed in x' by water depth perturbation $h'(x)$, bringing this perturbation inside derivatives with respect to x' , and taking the expected value give the governing equation for $P_{hh}(x', x)$,

$$\frac{\partial}{\partial x_i} \left(-\frac{\bar{h}^{5/3}}{2n_g \sqrt{S_0}} P_{ss}(x', x) + \frac{5\sqrt{S_0} \bar{h}^{2/3}}{3n_g} P_{hh}(x', x) - \frac{\sqrt{S_0} \bar{h}^{5/3}}{n_g} P_{nh}(x', x) \right) = -K_K P_{Kh}(x', x) \quad (D-6)$$

where $P_{hh}(x', x)$ is the auto-covariance of water depth; $P_{sh}(x', x)$ is the cross-covariance of surface slope and water depth; $P_{nh}(x', x)$ is the cross-covariance of Manning's coefficient and water depth $P_{Kh}(x', x)$ is the cross-covariance of hydraulic conductivity and water depth.

For this part we are only interested in deriving a relation between $P_{hh}(x', x)$ and $P_{sh}(x', x)$. From Equation D-6, we have,

$$P_{hh}(x', x) = -\frac{3\bar{h}}{10S_0} P_{sh}(x', x) \quad (D-7)$$

Combining Equations D-6 and D-7, then we have

$$P_{hh}(x', x) = \left(\frac{3\bar{h}}{10S_0} \right)^2 P_{ss}(x', x) \quad (D-8)$$

If we define $\zeta = x - x'$, then Equations D-5 and D-8 can be rewritten as,

$$P_{sh}(\zeta) = -\frac{3\bar{h}}{10S_0} P_{ss}(\zeta) \quad (\text{D-9})$$

$$P_{hh}(\zeta) = \left(\frac{3\bar{h}}{10S_0} \right)^2 P_{ss}(\zeta) \quad (\text{D-10})$$

The covariance of slope can be calculated from the covariance of microtopography. The relation between topography and surface slope exists,

$$S = -\frac{\partial h}{\partial z} \quad (\text{D-11})$$

According to Gelhar (1993), the covariance functions of surface slope and topography are related by the second-order differential equation.

$$P_{ss}(\zeta) = \frac{d^2 P_{zz}(\zeta)}{d\zeta^2} \quad (\text{D-12})$$

So if the $P_{zz}(\zeta)$ is give by Equation 6-33, then $P_{ss}(\zeta)$ is given by

$$P_{ss}(\zeta) = \frac{\sigma_z^2}{\lambda_z^2} e^{-|\zeta|/\lambda_z} \quad (\text{D-13})$$

From Equation D-13 it is straightforward to write the relation between σ_s^2 and σ_z^2 in the following form,

$$\sigma_s^2 = \sigma_z^2 / \lambda_z^2 \quad (\text{D-14})$$

LIST OF REFERENCES

- Abbott, M.B. 1979. Computational hydraulics---elements of the theory of free surface flows. Pitman, Boston, MA. 326p.
- Abriola, L.M., and K. Rathfelder. 1993. Mass balance errors in modeling two-phase immiscible flows: causes and remedies. *Advances in Water Resources* 16:223-39.
- Ahn, S., G. Kim, and G. Choi. 1993. On the applicable ranges of kinematic and diffusion models in open channels. H. W. Shen, S.T. Su, F. Wen, Editors. *Hydraulic Engineering '93*. ASCE Proc. Speciality Conf. San Francisco, CA.
- Akan, A.O., and B. C. Yen. 1981. Mathematical modeling of shallow water flow over porous media. *J. Hydraul. Div. Am. Soc. Civ. Eng.* 107:479-94.
- Allen, M.B., and C. L. Murphy. 1986. A finite-element collocation method for variably saturated flow in two space dimensions. *Water Resour. Res.* 22(11):1537-1542.
- Allen, R.G. 2000. Using FAO-56 dual crop coefficient method over an irrigated region as part of an evapotranspiration intercomparison study. *J. Hydrol.* 229:27-41.
- Allen, R.G., L. S. Pereira, D. Raes, and M. Smith. 1998. Crop evapotranspiration: Guidelines for computing crop water requirements. FAO, Rome, Italy, 300pp: FAO Irrigation and Drainage Paper 56.
- Belmans, C., J.G. Wesseling, and R.A. Feddes. 1983. Simulation model of the water balance of a cropped soil-SWATRE. *J. Hydrol.* 63:271-286.
- Berg P. 1999. Long-term simulation of water movement in soils using mass-conserving procedures. *Advances in Water Resources* 22(5):419-430.
- Beven, K., A. Calver, E.M. Morris. 1987. The Institute of Hydrology Distributed Model, Rep. No. 98, Institute of Hydrology, Wallingford.
- Binley, A., J. Elgy and K. Beven. 1989a. A physically base model of heterogeneous hillslopes, 1. Runoff production. *Water Resour. Res.* 25(6):1219-1226.
- Binley, A., K. Beven and J. Elgy. 1989b. A physically based model of heterogeneous hillslopes. 2. Effective hydraulic conductivities. *Water Resour. Res.* 25(6):1227-1233.
- Bond, J.J., and W.O. Willis. 1970. Soil water evaporation: First stage drying as influenced by surface residue and evaporation potential. *Proc. Soil Soc. Amer.* 34:924-928.

- Borah, D.K. 1989. Runoff simulation model for small watersheds. *Trans. Am. Soc. Agric. Eng.* 32:881-886.
- Borah, D.K., S.N. Prasad and C.V. Alonso. 1980. Kinematic wave routing incorporating shock fitting. *Water Resour. Res.* 16(3):529-541.
- Bouwer, H. 1964. Unsaturated flow in groundwater hydraulics. *J. Hydraul. Div. Amer. Soc. Civil Eng.* 90(HY5):121.
- Bouwer, H. 1969. Infiltration of water into nonuniform soil. *J. Irrig. Drain. Div. Amer. Soc. Civil Eng.* 95(IR4):384.
- Brakensiek, D.L. 1967. Kinematic flood routing. *Trans. ASAE.* 10(3):340-343.
- Bresler, E. and D. Dagan. 1983. Unsaturated flow in spatially variable fields, 2, Application of water flow models to various fields. *Water Resour. Res.* 19(2):421-428.
- Brooks, R.H., and A.T. Coorey. 1964. Hydraulic properties of porous media: Fort Collins. Colorado State University Hydrology Paper no. 3, 72p.
- Buckingham, E. 1907. Studies on the movement of soil moisture. U.S. Dept. of Agr. Bur. Soils Bull. 38.
- Burman, R., L. O. Pochop. 1994. Evaporation, evapotranspiration and climatic data Volume Developments in Atmospheric Science, 22 Elsevier.
- Cadwell, W.L. and R.L. Parsons. 1945. Average permeabilities of heterogeneous oil sands. *Trans. Am. Inst. Min. Metall. Pet. Eng.* 160:34-43.
- Celia, M.A., E.T. Bouloutas, and R.L. Zarba. 1990. A general mass-conservative numerical solution for the unsaturated flow equation. *Water Resour. Res.* 26(7):1483-1496.
- Chen, Z.-Q., R.S. Govindaraju and M.L. Kavvas. 1994a. Spatial averaging of unsaturated flow equation under infiltration conditions over areally heterogeneous fields, 1. Development of models. *Water Resour. Res.* 30(2):523-533.
- Chen, Z.-Q., R.S. Govindaraju and M.L. Kavvas. 1994b. Spatial averaging of unsaturated flow equation under infiltration conditions over areally heterogeneous fields, 2. Numerical simulations. *Water Resour. Res.* 30(2):535-548.
- Childs, E.C., and M. Bybordi. 1969. The vertical movement of water in a stratified porous material. 1. Infiltration. *Water Resour. Res.* 5(2):446.
- Childs, S.W., J.R. Gilley, and W.E. Splinter. 1977. A simplified model of corn growth under moisture stress. *Trans. ASAE* 20:858-65.

- Chow, V.T., and A. Ben-Zvi. 1973. Hydrodynamic modeling of two-dimensional watershed-flow. *J. Hydr. Div. ASCE* 99(1):2023-2040.
- Chow, V.T., D.R. Maidment, and L.W. Mays. 1988. *Applied Hydrology*. New York: McGraw-Hill Book Co. 572 p.
- Clement, T.P., W.R. Wise, and F.J. Molz. 1994. A physically based, two-dimensional, finite-difference algorithm for modeling variably saturated flow. *J. Hydrol.* 161:71-90.
- Cooley, R.L. 1983. Some new procedures for numerical solution of variably saturated flow problems. *Water Resour. Res.* 19(5):1271-85.
- Cordes, C., and W. Kinzelbach. 1992. Continuous groundwater velocity fields and path lines in linear, bilinear, and trilinear finite elements. *Water Resour. Res.* 28(11):2903-11.
- Corradini, C., F. Melone and R.E. Smith. 1994. Modeling infiltration during complex rainfall sequences. *Water Resour. Res.* 30(10):2777-2784
- Corradini, C., F. Melone and R.E. Smith. 1997. A unified model for infiltration and redistribution during complex rainfall patterns. *J. Hydrol.* 192:104-124.
- Corradini, C., R. Morbidelli and F. Melone. 1998. On the interaction between infiltration and Hortonian runoff. *J. Hydrol.* 204:52-67
- Cundy, T.W., and S.W. Tonto. 1985. Solution to the kinematic wave approach to overland flow routing with rainfall excess given by Philip's equation. *Water Resour. Res.* 21, 1132-1140.
- Dagan, D. 1982. Analysis of flow through heterogeneous random aquifers, 2, Unsteady flow in confined aquifers. *Water Resour. Res.* 18(5):1571-1585.
- Dagan, D., and E. Bresler. 1983. Unsaturated flow in spatially variable fields, 1, Derivation of models of infiltration and redistribution. *Water Resour. Res.* 19(2):413-420.
- Dagan, G. 1984. Solute transport in heterogeneous porous formations. *J. Fluid Mech.* 145:151-177.
- Dagan, G. 1989. *Flow and transport in porous formations*. Springer-Verlag, New York. 465p.
- de Faria, R.T., and C.A. Madramootoo. 1996. Simulation of soil moisture profiles for wheat in Brazil. *Agricultural Water Management* 31:35-49.
- Diersch, H-J.G., and P. Perrochet. 1999. On the primary variable switching technique for simulating unsaturated-saturated flows. *Advances in Water Resources* 23:271-301.

- Droogers, P. 2000. Estimating actual evapotranspiration using a detailed agro-hydrological model. *J. Hydrol.* 229:50-8.
- Droogers, P., F.B.W. van der Meer, and J. Bouma. 1997. Water accessibility to plant roots in different soil structures occurring in the same soil type. *Plan Soil* 188:83-91.
- Droogers, P., W.G.M. Bastiaanssen, M. Beyazaul, Y. Kayam, G. W. Kite, and H. Murray-Rust. 2000. Distributed agro-hydrological modeling of an irrigation system in Western Turkey. *Agricultural Water Management* 43:182-202.
- Dykaar, B.B. and P.K. Kitanidis. 1992a. Determination of the effective hydraulic conductivity for heterogeneous porous media using a numerical spectral approach. 1 Method. *Water Resour. Res.* 28(4):1155-1166.
- Dykaar, B.B. and P.K. Kitanidis. 1992b. Determination of the effective hydraulic conductivity for heterogeneous porous media using a numerical spectral approach. 1 Results. *Water Resour. Res.* 28(4):1167-1178.
- Eagleson, P.S. 1970. *Dynamic Hydrology*. McGraw-Hill, New York. 462 p.
- Feddes, R.A., P.J. Kowalik, K. K. Malinka, and H. Zaradny. 1976. Simulation of field water uptake by plants using a soil water dependent root extraction function. *J. Hydrol.* 31:13-26.
- Feddes, R.A., P. J. Kowalik, and H. Zaradny. 1978. Simulation of field water use and crop yield. Wageningen, the Netherlands. 189p: Center for Agricultural Publishing and Documentation.
- Forsyth, P.A., Y.S. Wu, and K. Pruess. 1995. Robust numerical methods for saturated-unsaturated flow with dry initial conditions in heterogeneous media. *Advances in Water Resources* 18:25-38.
- Foussereu, X., W.D. Graham, and P.S.C. Rao. 2000. Stochastic analysis of transient flow in unsaturated heterogeneous soils. *Water Resour. Res.* 36(4):891-910.
- Freeze, R.A. 1971. Three-dimensional, transient, saturated-unsaturated flow in a groundwater basin. *Water Resour. Res.* 7(2):347-66.
- Freeze, R.A. 1972. Role of subsurface flow in generating surface runoff. 1. Base flow contribution to channel flow. *Water Resour. Res.* 8(3): 609-623.
- Freeze, R.A. 1975. A stochastic-conceptual analysis of one-dimensional groundwater flow in a nonuniform homogeneous media. *Water Resour. Res.* 11(5):725-741.
- Freeze, R.A. 1980. A stochastic-conceptual analysis of rainfall-runoff processes on a hillslope. *Water Resour. Res.* 16(2):391-408.

- Galbiati, G., and F. Savi. 1995. Evaluation of the comparative influence of soil hydraulic properties and roughness on overland flow at the local scale. *Journal of Agricultural Engineering Research* 61:183-190
- Gandolfi, C. and F. Savi. 2000. A mathematical model for the coupled simulation of surface runoff and infiltration, *J. Agric. Engng Res.* 75:49-55.
- Garcia, R., and R.A. Kahawita. 1986. Numerical solution of the St. Venant equations with the MacCormack finite-difference scheme. *Int. J. Numer. Methods in Fluids* 6:507-27.
- Gardner, W.R. 1958. Some steady state solutions of the unsaturated moisture flow equation with application to evaporation from a water table, *Soil Sci.* 85:228-232.
- Gelhar, L.W. 1993. *Stochastic subsurface hydrology*. Prentice-Hall, Old Tappan, N.J. 390p.
- Giammarco, P.D., E. Todini, and P. Lamberti. 1996. A conservative finite elements approach to overland flow: the control volume finite element formulation. *J. Hydrol.* 175:267-91.
- Goodrich, D.C., D.A. Woolhiser, and T.O. Keefer. 1991. Kinematic routing using finite elements on a triangular irregular network. *Water Resour. Res.* 27:995-1003.
- Gottardi, G., and M. Venutelli. 1992. Moving Finite element model for one-dimensional infiltration in unsaturated soil. *Water Resour. Res.* 28(12):3259-67.
- Gottardi, G., and M. Venutelli. 1993. Control volume finite-element model for two-dimensional overland flow. *Adv. Water Resour.* 16(3):277-84.
- Gottardi, G., and M. Venutelli. 1993. Richards: computer program for the numerical simulation of one-dimensional infiltration into unsaturated soil. *Computers & Geosciences* 19(9):1239-66.
- Gottardi, G., and M. Venutelli. 1997. LANDFLOW: Computer program for the numerical simulation of two-dimensional overland flow. *Computers & Geosciences.* 23(1):77-89.
- Govindaraju, R.S., S.E. Jones, and M.L. Karras. 1988. On the diffusion wave model for overland flow 1. Solution for steep slopes. *Water Resour. Res.* 24(5):734-744
- Govindaraju, R.S., M.L. Kavvas, and G. Tayfur. 1992. A simplified model for two-dimensional overland flows. *Advances in Water Resources* 15:133-41.
- Graham, W., and D. McLaughlin. 1989. Stochastic analysis of nonstationary subsurface solute transport, 2. Conditional moments. *Water Resour. Res.* 25(11):2331-2355.

- Graser, E.A., and C.H.M. Van Bavel. 1982. The effect of soil moisture upon soil albedo. *Agricultural Meteorology* 27:17-26.
- Green, W.H., and C. Ampt. 1911. Studies of soil physics, Part I.-the flow of air and water through soils. *J. Agr. Sci.* 4:1-24
- Gutjahr, A.L., L.W. Gelhar, A.A. Bakr and J.L. MacMillan. 1978. Stochastic analysis of spatial variability in subsurface flows, 2, Evaluation and application. *Water Resour. Res.* 14(5):953-959.
- Hassan, A.E. 2001. Water flow and solute mass flux in heterogeneous porous formations with spatially random porosity. *J. Hydrol.* 242(1-2):1-25.
- Haverkamp, R., M. Vauclin, J. Touma, P.J. Wierenga, and G. Vachaud. 1977. A comparison of numerical simulation models for one-dimensional infiltration. *Soil Sci. Soc. Am. J.* 41:285-94.
- Hayhoe, H.N. and R. De Jong. 1988. Comparison of two soil water models for soybeans. *Can. Agric. Eng.* 30:5-11.
- Henderson, F.M. and R.A. Wooding. 1964. Overland flow and groundwater flow from a steady rainfall of finite duration. *J. Geophys. Res.* 69(8):1531-1540.
- Hills, R.G., D.B. Hudson, I. Porro, and P.J. Wierenga. 1989a. Modeling one-dimensional infiltration into very dry soils. 1. Model development and evaluation. *Water Resour. Res.* 25(6):1259-69.
- Hills, R.G., D.B. Hudson, I. Porro, and P.J. Wierenga. 1989b. Modeling one-dimensional infiltration into very dry soils. 2. Estimation of the soil water parameters and model predictions. *Water Resour. Res.* 25(6):1271-81.
- Holden, A.P., and D. Stephenson. 1995. Finite difference formulations of kinematic equations. *Journal of Hydraulic Engineering* 121(5):423-6.
- Hoogland, J.C., R.A. Feddes, and C. Belmans. 1981. Root water uptake model depending on soil water pressure head and maximum extraction rate. *Acta. Hort.* 119:123-36.
- Hopmans, J.W., H. Schukking and P.J.J.F. Torfs. 1988. Two dimensional steady state unsaturated water flow in heterogeneous soils with autocorrelated soil hydraulic properties. *Water Resour. Res.* 24(12):2005-2017.
- Horritt, M.S. 2002. Stochastic Modelling of 1-D Shallow water flows over uncertain topography. *Journal of Computational Physics.* 180(1):327-338.

- Hromadka, T.V. II, and C. Lai. 1985. Solving the two-dimensional diffusion flow equations. Proc. of the Spec. Conf. Sponsored by the Hydr. Div. of the ASCE. New York, N.Y.
- Huang, K., B.P. Mohanty, and M.T. van Genuchten. 1996. A New convergence criterion for the modified Picard iteration method to solve the variably saturated flow equation. *J. Hydrol.* 178:69-91.
- Hunt, B. 1987. A perturbation solution of the flood routing problem. *J. Hydraul. Res.* 25(3):215-234.
- Huyakorn, P.S., and G. F. Pinder. 1983. Computational Methods in subsurface flow. Academic Press, New York.
- Huyakorn, P.S., E.P. Springer, V. Guvansen, and T.D. Wordsworth. 1986. A three-dimensional finite-element model for simulating water flow in variable saturated porous media. *Water Resour. Res.* 22(13):1790-808.
- Huyakorn, P.S., S.D. Thomas, and B.M. Thompson. 1984. Techniques for making finite elements competitive in modeling flow in variably saturated porous media. *Water Resour. Res.* 20(8):1099-115.
- Idso, S.B., R.D. Jackson, R.J. Reginato, B.A. Kimball, and F.S. Nakayama. 1975. The dependence of bare soil albedo on soil water content. *J. Appl. Meteor.* 14:109-13.
- Iwagaki, Y. 1955. Fundamental studies on runoff analysis by characteristics, *Bull.* 10:1-25, Disaster Prev. Res. Inst., Kyoto Univ. Kyoto, Japan, 1955.
- Iwasa, Y., and K. Inoue. 1982. Mathematical simulations of channel and overland flood flows in view of flood disaster engineering. *Nat. Disaster Sci.* 4(1):1-30.
- Izzard, C.F., and M. T. Augustine. 1943. Preliminary report on analysis of runoff resulting from simulated rainfall on a paved plot. *Trans. Am. Geophysical Union*:500-509.
- Jackson, R.B., J. Canadell, J.R. Ehleringer, H.A. Mooney, O.E. Sala, and E.D. Schulze. 1996. A global analysis of root distributions for terrestrial biomes. *Oecologia.* 108:389-441
- Jacobs, J.M., S.L. Mergelsberg, A.F. Lopera and D. A. Myers. 2002. Evapotranspiration from a wet prairie wetland under drought conditions: Paynes Prairie Preserve, Florida, USA. *Wetlands* 22(2):374-385.
- Jensen, M.E., R.D. Burman, and R.G. Allen. 1990. Evapotranspiration and irrigation water requirements. ASCE, New York: Manual of Practice No. 70.
- Ju, S. and K.-J.S. Kung. 1997. Mass types, element orders and solution schemes for the Richards Equation. *Computers & Geosciences* 23(2):175-87.

- Julien, P.Y. and G.E. Moglen. 1990. Similarity and length scale for spatially varied overland flow. *Water Resour. Res.*, 26(8):1819-1832.
- Kalisz, P.J., R.W. Zimmerman, and R.N. Muller. 1987. Root density, abundance, and distribution in the mixed mesophytic forest of eastern Kentucky. *Soil Sci. Soc. Am. J.* 51:220-5.
- Katopodes, N.D. and T. Strelkoff 1977. Hydrodynamics of border irrigation: complete model. *Journal of the Irrigation and Drainage Division, ASCE* 103(IR3): 309-323.
- Katopodes, N.D. and R. Strelkoff. 1978. Computing two-dimensional dam break flood waves. *J. Hydr. Div. ASCE.* 104(9):1269-1288.
- Kawahara, M., and T. Yokoama. 1980. Finite element method for direct runoff flow. *J. Hydr. Div., ASCE* 106(4):519-34.
- Kirkland, M.R., R.G. Hills, and P.J. Wierenga. 1992. Algorithms for solving Richards' equation for variably saturated soils. *Water Resour. Res.* 28(8):2049-58.
- Kristensen, K.J., and S.E. Jensen. 1975. A model for estimating actual evapotranspiration from potential transpiration. *Nordic Hydrology* 6:70 - 88.
- Lai, C.T., and G. Katul. 2000. The dynamic role of root-water uptake in coupling potential to actual transpiration. *Advances in Water Resources* 23:427-39.
- Lal, A.M.W. 1998a. Performance comparison of overland flow algorithms. *Journal of Hydraulic Engineering* 124(4):342-9.
- Lal, A.M.W. 1998b. Weighted implicit finite-volume model for overland flow. *Journal of Hydraulic Engineering* 124(9):941-50.
- Lappala, E.G., R.W. Healy, and E.P. Weeks. 1987. Documentation of computer program VS2D to solve the equations of fluid flow in variably saturated porous media: U.S. Geological Survey Water-Resources Investigations Report 83-4009, 184 p.
- Li, L., and W.D. Graham. 1998. Stochastic analysis of solute transport in heterogeneous aquifers subject to spatially random recharge, *J. Hydrol.* 206(1-2):16-38.
- Li, R.M., D.B. Simons. And M.A. Stevens. 1975. Nonlinear kinematic wave approximation for water routing. *Water Resour. Res.* 11(2):245-252.
- Liedl, R., G.H. Schmitz, and G.J. Seus. 1996. Comment on "Mass conservative numerical solutions of the head-based Richards equation". *Water Resour. Res.* 32(3):759-60.

- Liggett, J.A., and D.A. Woolhiser. 1967. Difference solutions of the shallow water equation. *J. Engrg. Mech. Div., ASCE*. 93(2):39-71.
- Lighthill, M.J., and C.B. Whitham. 1995. On kinematic waves: Flood movement in long rivers. *Proc. R. Soc. London, Ser. A*. 229:281-316.
- Maller, R.A., and M.L. Sharma. 1981. An analysis of areal infiltration considering spatial variability. *J. Hydrol.* (52), 25-37.
- Mantoglou, A. 1992. A theoretical approach for modeling unsaturated flow in spatially variable soils: Effective flow models in finite domains and nonstationarity. *Water Resour. Res.* 28(1):251-267.
- McNaughton, K.G., and P.G. Jarvis. 1983. Predicting effects of vegetation changes on transpiration and evaporation. *Water Deficits and Plant Growth* 7:1-47.
- Mein, R.G., and C.L. Larson. 1973. Modeling infiltration during a steady rain. *Water Research Resource* 9(2):384.
- Melone, F., C. Corradini, and V.P. Singh. 1998. Simulation of the direct runoff hydrograph at basin outlet. *Hydrological Processes* 12:769-79.
- Merz, B., and E.J. Plate. 1997. An analysis of the effects of spatial variability of soil and soil moisture on runoff. *Water Resour. Res.*, 33(12):2909-2922.
- Milly, P.C.D. 1985. A mass-conservative procedure for time-stepping in models of unsaturated flow. *Advanced Water Resources* 8:32-6.
- Molz, F.J. 1981. Models of water transport in the soil-plant system: A review. *Water Resour. Res.* 17(5):1245-60.
- Molz, F.J., and I. Remson. 1970. Extraction term models of soil moisture use by transpiring plants. *Water Resour. Res.* 6(5):1346-1356.
- Monteith, J.L. 1981. Evaporation and surface temperature. *Quart. J. Roy. Meteorol. Soc.* 107:1-27.
- Morita, M., and B.C. Yen. 2000. Numerical methods for conjunctive two-dimensional surface and three-dimensional sub-surface flows. *Int. J. Numer. Met. Fluids*. 32:921-957.
- Motha, J.A., and J. M. Wigham. 1995. Modeling overland flow with seepage. *J. Hydrol.* 169:265-280.
- Munoz-Carpena, R., C. T. Miller, J. E. Parsons. 1993. A Quadratic Petrov-Galerkin solution for kinematic wave overland flow. *Water Resour. Res.* 29(8):2615-27.

- Munoz-Carpena, R., J.E. Parsons, and J.W. Gilliam. 1993. Numerical approach to the overland flow process in vegetative filter strips. *Trans. Am. Soc. Agric. Eng.* 36:761-770.
- Neuman, S.P. 1973. Saturated-unsaturated seepage by finite elements. *Journal of the Hydraulics Division* 99, HY12:2233-51.
- Nimah, M.N., and R.J. Hanks. 1973. Model for estimating soil water, plant and atmosphere interrelations. I. Description and sensitivity. *Soil Sci. Soc. Am. Proc.* 37: 522-527.
- Osnes, H. 1998. Stochastic analysis of velocity spatial variability in bounded rectangular heterogeneous aquifers. *Advances in Water Resources* 21(3):203-215.
- Paniconi, C., A.A. Aldama, and E.F. Wood. 1991. Numerical evaluation of iterative and noniterative methods for the solution of the nonlinear Richards equation. *Water Resour. Res.* 27(6):1147-63.
- Paniconi, C., and E. F. Wood. 1993. A detailed model for simulation of catchment scale subsurface hydrologic processes. *Water Resour. Res.* 29(6):1601-20.
- Paniconi, C., and M. Putti. 1994. A comparison of Picard and Newton iteration in the numerical solution of multidimensional variably saturated flow problems. *Water Resour. Res.* 30(12):3357-74.
- Parlange, J.Y., R. Haverkamp, and J. Tourna. 1985. Infiltration under ponded conditions: 1. optimal analytical solution and comparison with experimental observations. *Soil Science* 139, 305-311
- Perrochet, P. 1987. Water uptake by plant roots--A simulation model, 1. Conceptual model. *J. Hydrol.* 95:55-61.
- Philip, J.R. 1957. The theory of infiltration. Sorptivity and algebraic infiltration equations. *Soil Sci.* 84:257-264.
- Philip, J.R. 1969 Theory of infiltration. *Adv. Hydrol. Sci.* 5: 215-296.
- Pinder, G.F., and S.P. Sauer. 1971. Numerical simulation of flow wave modification due to back storage effects. *Water Resour. Res.* 7(1): 63-70.
- Playan, E., W.R. Walker, and G.P. Merkley. 1994. Two-dimensional simulation of basin irrigation, 1: theory. *Journal of Irrigation and Drainage Engineering, ASCE* 120(5): 837-856.
- Ponce, V.M., O.I. Cordero-Brana, and S.Y. Hasenin. 1997. Generalized conceptual modeling of dimensionless overland flow hydrographs. *J. Hydrol.* 200:222-7.

- Ponce, V.M., R.-M. Li, and D.B. Simons. 1978. Applicability of kinematic and diffusion models. *J. Hydr. Engrg., ASCE* 104(3):353-60.
- Pozdniakov, S.P. and C.-F. Tsang. 1999. A semianalytical approach to spatial averaging of hydraulic conductivity in heterogeneous aquifers. *J. of Hydro..* 216:78-98.
- Prasad, R. 1988. A linear root water uptake model. *J. Hydrol.* 99, 297-306.
- Radersma, S., and N. de Ridder. 1996. Computed evapotranspiration of annual and perennial crops at different temporal and spatial scales using published parameter values. *Agricultural Water Management* 31:17-34.
- Rathfelder, K., and L. M. Abriola. 1994. Mass conservative numerical solutions of the head-based Richards equation. *Water Resour. Res.* 30(9):2579-86.
- Rice, J.G. and R.J. Schnipke. 1985. A monotone streamline upwind finite element method for convection dominated flows. *Computer Methods in Applied Mechanics and Engineering.* 48:313-317.
- Richards, L.A. 1931. Capillary conduction of liquids through porous media, *Physics.* 1:318-333.
- Romano, N., B. Brunone, and A. Santini. 1998. Numerical analysis of one-dimensional unsaturated flow in layered soils. *Advances in Water Resources* 21:315-24.
- Ross, P.J. 1990. Efficient numerical methods for infiltration using Richards' equation. *Water Resour. Res.* 26(2): 279.
- Ross, R.B., D.N. Contractor, and V.O. Shanholtz. 1979. A finite element model of overland and channel flow for assessing the hydrologic impact of land-use change. *J. Hydrol.* 41:11-30.
- Rowse, H.R., D.A. Stone, and A. Gerwitz. 1978. Simulation of the water distribution in soil, II. The model for cropped soil and its comparison with experiment. *Plant Soil*, 49: 533-550.
- Rubin, Y. 1990. Stochastic modeling of macrodispersion in heterogeneous media. *Water Resour. Res.* 24(3):453-459.
- Russo, D. 1993. Stochastic modeling of macrodispersion for solute transport in a heterogeneous unsaturated porous formation. *Water Resour. Res.* 29:383-397.
- Russo, D., J. Zaidel, and A. Laufer. 1998. Numerical analysis of flow and transport in a three-dimensional partially saturated heterogeneous soil. *Water Resour. Res.* 34:1451-1468.

- Saghafian, B., P.Y. Julien and F.L. Ogden. 1995. Similarity in catchment response 1. Stationary rainstorms. *Water Resour. Res.* 31(6):1533-1541.
- Sainju, U.M., and R.E. Good. 1993. Vertical root distribution in relation to soil properties in New Jersey Pinelands forests. *Plant Soil* 150:87-97.
- Sakkas, J.G., C.V. Bellos, and M.N. Klonaraki. 1994. Numerical computation of surface irrigation. *Irrigation Science* 15:83-99
- Savabi, M.R. 1993. Modeling subsurface drainage and surface runoff with WEPP. *Journal of Irrigation and Drainage Engineering, ASCE* 119(5): 801-813.
- Schmid, B.H. 1989. On overland flow modeling: can rainfall excess be treated as independent of flow depth? *J. Hydrol.* 107:1-8.
- Schmidhalter, U., H.M. Selim, and J.J. Oertli. 1994. Measuring and modeling root water uptake based on chloride discrimination in a silt loam soil affected by groundwater. *Soil Sci.* 158:97-105.
- Seguis, L., B. Cappelaere, C. Peugeot and B. Vieux. 2002. Impact on Sahelian runoff of stochastic and elevation-induced spatial distributions of soil parameters. *Hydrological Processes.* 16:313-332.
- Singh, V., and S.M. Bhallamudi. 1996. Complete hydrodynamic border-strip irrigation model. *Journal of Irrigation and Drainage Engineering, ASCE* 122(4):189-197.
- Singh, V., and S.M. Bhallamudi. 1998. Conjunctive surface-subsurface modeling of overland flow. *Advances in water Resources* 21:567-579.
- Sivapalan, M., and E.F. Wood. 1986. Spatial heterogeneity and scale in the infiltration response of catchments. In: Gupta, V.K., Rodriguez-Iturbe, L., Wood, E.F., (eds.), *Scale Problems in Hydrology*. D. Reidel, Haningham, MA, pp. 81-106.
- Smith, R.E. and R.H.B. Hebbert. 1979. A Monte Carlo analysis of the hydrologic effects of spatial variability of infiltration. *Water Resour. Res.* 15(2):419-429.
- Smith, R.E., R.H.B. Hebbert. 1983. Mathematical simulation of interdependent surface and subsurface hydrologic processes. *Water Resour. Res.* 19(4):987-1001
- Smith, R.E. and J.Y. Parlange. 1978. A parameter-efficient hydrologic infiltration model, *Water Resour. Res.* 14(3):533-538.
- Smith, R.E. and D.A. Woolhiser. 1971. Overland flow on an infiltrating surface. *Water Resour. Res.* 7(4):899-913.

- Srivastava, R., and T.C.J. Yeh. 1991. Analytical solutions for one-dimensional, transient infiltration toward the water table in homogeneous and layered soils. *Water Resour. Res.* 27(5):753-62.
- Stone, J.J., L.J. Lane, and E.D. Shirley. 1992. Infiltration and runoff simulation on a plane. *Trans. Am. Soc. Agric. Eng.* 35(1):161-170.
- Strelkoff, T., and N.D. Katopodes. 1977. Border irrigation hydraulics with zero inertia. *Journal of Irrigation and Drainage Division ASCE*, 103:325-342
- Tan, W. 1992. *Shallow water hydrodynamics*. New York, N. Y.: Elsevier Science Publishing Co., Inc.
- Tartakivsky, D.M., S.P. Neuman and Z. Lu. 1999. Conditional stochastic averaging of steady state unsaturated flow by means of Kirchhoff transformation. *Water Resour. Res.* 35(3):731-745.
- Tayfur, G., M.L. Kavvas, R.S. Govindaraju, and D. E. Storm. 1993. Applicability of St. Venant equations for two-dimensional overland flows over rough infiltrating surfaces. *J. Hydr. Engrg. ASCE* 119(1):51-63.
- Taylor, C., G. Al-Mashidani, and J.M. Davis. 1974. A finite element approach to watershed runoff. *J. Hydro. Div., ASCE* 21:231-46.
- Tisdale, T.S., P.D. Scarlatos, and J.M. Hamrick. 1998. Streamline upwind finite-element method for overland flow. *Journal of Hyaulic Engineering* 124(4):350-357.
- Tompson, A.F.B., R. Ababou, and L.W. Gelhar. 1989. Implementation of the 3-dimensional turning bands random field generator. *Water Resour. Res.* 25(10):2227-2243.
- Van Duin, R.H.A. 1955. Tillage in relation to rainfall intensity and infiltration capacity of soils. *Neth. J. Agr. Sci.* 3:182.
- van Genuchten, M.T. 1980. A closed-form equation for predicting the hydraulic conductivity of unsaturated soils. *Sci. Soc. Am. J.* 44:892-898.
- Vieux, B.E., V.F. Bralts, L.J. Segerlind, and R.B. Wallace. 1990. Finite element watershed modeling:one-dimensional elements. *J. Water Resour. Plan. Manage. Div. Am. Soc. Civ. Eng.* 116(6):803-19.
- Vieux, B.E., and N. Gaur. 1994. Finite element modeling of storm water runoff using GRASS GIS. *Microcomputers in Civil Engineering* 9:263-270.

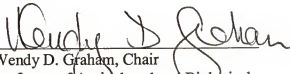
- Wagenet, R.J., and J.L. Huston. 1989. LEACHM: Leaching Estimation and Chemistry Model. Version 2. Center for Environmental Research, Cornell University, Ithaca, New York.
- Wallach, R., G. Grigorin and J. Rivlin. 1997. The errors in surface runoff prediction by neglecting the relationship between infiltration rate and overland flow depth. *J. Hydrol.* 200:243-259.
- Wallach, R., D. Zaslavsky, and M. Israeli. 1989. A small perturbation solution for steady infiltration due to nonuniform water application. *Water Resour. Res.* 25:1989-1998.
- Wooding, R.A. 1965. A hydraulic model for the catchment-stream problem. *J. Hydrol.* 3:254-267.
- Woolhiser, D.A. 1969. Overland flow on a converging surface. *Trans. ASAE.* 12(4):460-462.
- Woolhiser, D.A. and D.C. Goodrich. 1988. Effect of rainfall intensity patterns on surface runoff. *J. Hydrol.* 102:335-354.
- Woolhiser, D.A., R.E. Smith and J.-V Giraldez. 1996. Effects of spatial variability of saturated hydraulic conductivity on Hortonian overland flow. *Water Resour. Res.* 32(3):671-678.
- Woolhiser, D.A., R.E. Smith, D.C. Goodrich. 1990. KINEROS, A Kinematic Runoff and Erosion Model: Documentation and User Manual. USDA-ARS, ARS Publication No. 77.
- Wu, J., R. Zhong, and S. Gui. 1999. Modeling soil water movement with water uptake by roots. *Plant and Soil* 215:7-17.
- Xanthopoulos, T.H., and C.H. Koutitas. 1976. Numerical simulation of two dimensional flood wave propagation due to dam failure. *J. Hydr. Research* 14(4):321-31.
- Yakirevich, A., P. Berliner, and S. Sorek. 1997. A model for numerical simulating of evaporation from bare saline soil. *Water Resour. Res.* 33(5):1021-33.
- Yakirevich, A., V. Borisov, and S. Sorek. 1998. A quasi three-dimensional model for flow and transport in unsaturated and saturated zones: 1: Implementation of the quasi two-dimensional case. *Advances in Water Resources* 21(8):679-89.
- Yeh, G.T. 1981. On the computation of Darcian velocity and mass balance in the finite element modeling of groundwater flow. *Water Resour. Res.* 17(5):1529-34.

- Yen, B.C., and R. Riggins. 1991. Time scales for conjunctive modeling of subsurface and surface water motion. *Irrigation and Drainage, Proceedings of ASCE National Conference, Honolulu*: 351-358.
- Zhang, D. 1998. Numerical solutions to statistical moment equations of groundwater flow in nonstationary, bounded heterogeneous media. *Water Resour. Res.* 34(3):529-538.
- Zhang, W., and T.W. Cundy. 1989. Modelling of two-dimensional overland flows. *Water Resour. Res.* 25(9):2019-2035.
- Zhao, D.H., H.W. Shen, G.Q. Tabios, J.S. Lai, III, and W.Y. Tan. 1994. Finite-volume two-dimensional unsteady flow model for river basins. *J. Hydr. Engrg. ASCE* 120(7):863-83.
- UF-IFAS. 2001. Florida Automated Weather Network.
<http://fawn.ifas.ufl.edu/data/chart.html> University of Florida. Date accessed: December 2002.


BIOGRAPHICAL SKETCH

Siqing Liu was born in Hubei, China, in 1966. He graduated from the Huazhong University of Science and Technology in Wuhan, China, with a Bachelor of Science degree in fluid engineering and fluid machinery in July 1988. In September 1988, he enrolled as a graduate student in the Department of Civil Engineering at the China Agricultural University. He earned his Master of Engineering degree in July 1991. In September 1991, he was employed as a lecturer in the Department of Civil Engineering at the China Agricultural University. He taught several courses and carried out research on optimistic design of pumps, pump performance test and optimistic running of water turbines. He worked at China Agricultural University for six years. In October 1997, he was admitted to the Ph.D. program in mechanical engineering at the University of Leeds, Leeds, England. In August 1998, he attended Utah State University, Logan, USA; and worked on his Ph.D study in the Department of Biological and Irrigation Engineering with a major in hydrological science. In August 1999, he transferred to the University of Florida and began his Ph.D study in the Department of Agricultural and Biological Engineering.


I certify that I have read this study and that in my opinion it conforms to acceptable standards of scholarly presentation and is fully adequate, in scope and quality, as a dissertation for the degree of Doctor of Philosophy.


Wendy D. Graham, Chair
Professor of Agricultural and Biological
Engineering


I certify that I have read this study and that in my opinion it conforms to acceptable standards of scholarly presentation and is fully adequate, in scope and quality, as a dissertation for the degree of Doctor of Philosophy.


Kenneth L. Campbell, Cochair
Professor of Agricultural and Biological
Engineering

I certify that I have read this study and that in my opinion it conforms to acceptable standards of scholarly presentation and is fully adequate, in scope and quality, as a dissertation for the degree of Doctor of Philosophy.


Jonathan D. Jordan
Assistant in of Agricultural and Biological
Engineering

I certify that I have read this study and that in my opinion it conforms to acceptable standards of scholarly presentation and is fully adequate, in scope and quality, as a dissertation for the degree of Doctor of Philosophy.


Jennifer M. Jacobs
Assistant Professor of Civil and Coastal
Engineering

I certify that I have read this study and that in my opinion it conforms to acceptable standards of scholarly presentation and is fully adequate, in scope and quality, as a dissertation for the degree of Doctor of Philosophy.



Kirk Hatfield
Associate Professor of Civil and Coastal
Engineering

This dissertation was submitted to the Graduate Faculty of the College of Engineering and to the Graduate School and was accepted as partial fulfillment of the requirements for the degree of Doctor of Philosophy.

August 2003



Pramod P. Khargonekar
Dean, College of Engineering

Winfred M. Philips
Dean, Graduate School